Transition metals doped TiO₂ nanoparticles obtained by sol-gel templated assisted synthesis. Physico-chemical properties and catalytic applications

By

Roberto Nasi
* * * * * *

Supervisors
Prof. Barbara Bonelli, Supervisor
Prof. Serena Esposito, Co-Supervisor
Prof. Marco Armandi, Co-Supervisor

Doctoral Examination Committee:
Prof. Ilenia Rossetti, Università degli studi di Milano
Prof. Vincenzo Vaiano, Università degli studi di Salerno

Politecnico di Torino
October 14, 2019

I hereby declare that, the contents and organisation of this dissertation constitute my own original work and does not compromise in any way the rights of third parties, including those relating to the security of personal data.

………………………………......

Roberto Nasi

Turin, February 29, 2019

Abstract

The discover made by Fujishima and Honda in 1972 on the photocatalytic water splitting catalysed by TiO_2 photosensitization effect [1] started a new increasing interest in the research of this material that was anyway long studied before (first report on TiO_2 photocatalysis was done by Renz et al. on 1921 [2]), which led to development of many new applications, especially in catalysis and photocatalysis, environmental field (anti-bacteria, deodorization, water treatment, dirtiness prevention by wettability control..), as well as in the energy harvesting and storage (e.g Grätzel cells and Lithium Ion Batteries) [3].

In the last decades many aspects of TiO_2 have been explored and countless efforts have been dedicated to characterize the properties of titanium dioxide, but due to the multitude of variables, much can still be explored and understood in order to have a better knowledge of the material properties and subsequently engineer the final product. For instance, final product properties strongly depends from synthetic conditions, methods and process parameters, used precursor materials, dopants, morphology and surface texture. Moreover, TiO_2 may occur as different polymorphs (mainly as anatase, rutile and brookite) as well as amorphous TiO_2, with up to 12 reported bulk and/or nanocrystalline phases, which compositions depends on these factors too as by adjusting the synthetic conditions and post treatments, the final combination of different amounts of each phase can be tuned.

Alongside the chemical and crystal properties, morphology and surface texture play an important role in the final material properties. Nanoparticles morphology, as an example, can enhance the adsorption coefficients of organic molecules adsorbed on their surfaces, the rate of adsorption of molecules and the rate of electron transfer at the particle surface. All important factors for catalytic processes. Therefore, tailoring particles shape, size and surface morphology is necessary for a variety of applications.

As can be easily understood, these mentioned "*variables*" are just for the starting material (TiO₂), but the problem (the final material properties-parameters relationship) become more and more complex as external variables are added. For example, in photocatalytic applications one of the key parameters of a catalyst is the band gap, which is easily tuneable by the presence of a doping element, which in turn may strongly modify all the other physical-chemical and textural properties, so increasing the complexity of the material characterization.

In this thesis, the TiO₂ system will be briefly introduced, with major stress on the last trends and applications of nanostructured titania systems. Whereas in the following chapters, the synthetic methodology adopted to produce metal oxides will be explored and lastly will be reported the characterization of the TiO₂ system that has been performed during this PhD work, having special consideration for high surface area nanoparticles synthetized by templated assisted sol-gel (TASG) synthesis, which is extremely flexible in terms of composition, precursors and doping materials that can be used, which in this work are Molybdenum and Manganese. Likewise, in terms of real cases usage, the synthetized materials have been tested for modern-day important applications by exploiting the tailored material properties.

High surface area NPs, possibly characterized by hierarchical inter-and/or intra-particle porosity, where obtained by using soft templates in order to improve the material catalytic activity and to facilitate the diffusion of reagents/products, as well as modify the surface physical-chemical characteristics of acidity, charge and phase composition. Moreover, the contribution of doping with heteroatoms, has been explored, by selecting two elements of the most interesting and promising properties from literature research (Mo, Mn) and the modification of physical-chemical properties as well as the changes in optical responses and the textural modifications due respect the bare titania has been studied.

In order to investigate and have an idea of the catalytic real cases performances, photocatalytic tests of Mo-doped TiO₂ samples have been carried out for photodegradation of Rhodamine B dye, a model molecule used as water "*pollutant*". Nonetheless manganese oxides, interesting due to various types of labile oxygen and oxidation states (Mn^{2+}, Mn^{3+} and Mn^{4+}), has been used at low doping concentration supported on the strong acidic surface of TiO₂ and tested as catalytic promoter for the low-temperature NOx removal by using the Selective Catalitic Reduction (SCR) with ammonia, exploiting the surface acidity/basicity

characteristics as well as peculiar composition of the produced catalyst by the TASG method.

Acknowledgment

Contents

List of Tables

1

List of Figures

Chapter 1
Introduction

1.1 Motivation of the study

Titanium dioxide (TiO_2) is the 9th most abundant element on the Earth (0.63% of the Earth's crust) but does not occur in nature as pure form but is derived from ilmenite or leuxocene ores [4]. It was initially mass produced after the First World War in 1918 for uses for both macro and micro-scale application such as pigment in paints [5], sunscreens and ultraviolet protective cosmetics [6–8], food additives [9], toothpastes, construction materials [10], ceramics, photoelectrochromics, photovoltaics (especially dye-sensitized solar cells) [3], water splitting [1], photocatalysis, sensor, mixed applications [11], etc [12–14]. TiO_2 is well known for its high chemical, thermal and under illumination stability, as well as its environmentally friendly applications and low toxicity [15][16][14]. Along with ZnO, TiO_2 is also one of the most investigated wide band gap semiconductor for catalysts-photocatalyst processes, as it is able to decompose several organic [17] and inorganic pollutants in both liquid and gas phases [18–20], so it founds applications in water and air cleaning systems and self-cleaning coatings [21][22][23].

TiO_2 may occur mainly as anatase, rutile and brookite polymorphs as well as amorphous TiO_2, but up to 12 reported bulk and/or nanocrystalline phases of TiO_2 were discovered, with more detailed discussion in the next chapter of this thesis.

By properly tailoring the synthesis conditions and nanoparticle dimensions, pure or mixed phases can be obtained. While in bulk TiO_2, rutile is the stable phase above 600 °C, synthesis methods starting from solutions containing a Ti precursor generally lead to the formation of anatase. When TiO_2 nanoparticles (NPs) are obtained, polymorphs that are usually metastable in the bulk may be, instead, stabilized: among TiO_2 polymorphs, anatase has the lowest surface energy, so NPs of this polymorph under 15 – 30 nm dimension are more easily obtained [24–26]. Instead, if a strong acid is added, brookite NPs are somewhat preferentially formed [26][27]. This polymorph is not commonly observed in minerals due to its metastable character and difficult to synthesize in pure form.

Nanoparticles properties also differ from bulk materials in many ways and can be critical to obtain tailored characteristics. For instance nanoparticles can enhance the adsorption coefficients of organic molecules adsorbed on their surfaces [29], or the rate of adsorption of molecules and the rate of electron transfer at the particle surface, which are important factors for catalytic process. For these reasons, tailoring particles size and surface acidity/basicity is very interesting for a variety of applications, in order to impart the desired characteristics to the final material. To have an idea of the implication of nanoparticle size and phase composition, as

one of the many example that can be cited, Jang et al found that the degree of decomposition of methylene blue, bacteria and ammonia gas by TiO_2 nanoparticles under illumination was directly proportional to the anatase mass fraction, but inversely to the particle size [30].

As far as photocatalytic applications are concerned, the band gap is one of the most important parameters. Anatase has a band-gap (E_g) of around 3.2 eV, whereas that of rutile is 3.0 eV and that of brookite is in the range between 3.1 and 3.4 eV (*vide infra*): consequently, TiO_2 is mainly active under UV light. Moreover, electron-hole pairs are characterized by relatively fast recombination rate (from pico- to micro-seconds) [31] that decreases its photocatalytic efficiency. In addition, the TiO_2 polar surface has a poor adsorption ability towards non-polar organic molecules, further limiting is efficiency towards the removal of organic pollutants [32].

With the aim of improving the understanding of nano-TiO_2 physical-chemical characteristics and the photocatalytic activity of such material, doping with heteroatoms, including transition metals (Cr, Co, Fe, Ni, Mn, V, Cu, Ni and Zn) and non-metals, has been subject of many studies, since it should allow narrowing the band gap and improving its solar light absorption [33–36]. Concerning doping with transition metals, the absorption edge shifts towards longer wavelengths due to charge-transfer transitions between *d* electrons of the transition metals and the CB (conduction band) or the VB (valence band). Rare earths have good electron trapping properties, resulting in a large absorption edge shift towards longer wavelengths, whereas defects chemistry can also play an important role in the reactions kinetics and charge recombination.

Non-metals (C, B, I, F, S, and N) doping at the O sites of TiO_2 NPs has also been largely exploited: N appears to be one of the most efficient (and investigated) dopants, the enhancement of charge separation being ascribed to the formation of paramagnetic species [O-Ti^{4+}-N^{2-}-Ti^{4+}-V_O], where V_O is an oxygen vacancy. With non-metals doping, impurity states are located near the VB edge and their role as recombination centres might be minimized [34,37].

Other studies show, instead, that if TiO_2 is modified by adding noble metals (such as Ag, Pt , Pd , Rh and Au), electron-hole recombination is hindered by the resulting Schottky barrier at the metal-TiO_2 interface, where the former acts as a storing-transporting mediator of photogenerated electrons from the surface of TiO_2 to an acceptor (in the reaction medium). Consequently, the photocatalytic activity increases as the charge carrier recombination rate decreases [38–42].

Concerning transition metals, Mo doping is very promising since it introduces an empty donor level below the CB (n-type doping), which only slightly perturbs the band [43], so avoiding strongly localized *d* states that can reduce the mobility of charge carriers [44]. In this context, titania nano-photocatalysts have, among the most promising advanced oxidation technologies (AOTs), proven useful to treat persistent organic pollutants (POPs) [45] (resistant to environmental degradation), several other organic/inorganic pollutants in both liquid and gas phases [18–20], as well as dyes, biological toxins and pathogenic microorganisms [46] due to peculiar

properties such as, but not limited to, the effectiveness to generate hydroxyl radicals [22], thus playing an important role in the remediation of environmental and pollution challenges, especially underlining the incapability of conventional water-treatment systems to fully decompose these pollutants in aqueous media, due to industrial, agricultural [47], and domestic activities.

Concerning non-photocatalytic application, TiO_2 is, among many other applications, also widely used as support or stand-alone catalytic material for a variety of uses such as removal of nitrogen oxides. The BP's Energy Outlook of 2016 estimate that fossil fuels will remain the dominant source of energy for the whole world's economy, with 60% of the energy increase till 2035, parted as oil (+63%), natural gas (+193%) and coal (+5%) accounting for 53% of the growth. The combustion of fossil fuels of course inevitably leads to the production of different air pollutants as sulphur dioxide, nitrogen oxides, particulate with heavy metals and not last, volatile organic compounds (VOCs). NO_x have been shown to be major air pollutants discharged by combustion engines (as the primary mobile sources), power plants and nitric acid production plants (as stationary ones) and are associated with a series of environmental issues (eg. acid rain, ozone depletion and photochemical smog), especially NO_2 have a high global warming potential (around 300 times higher than CO_2) meanwhile N_2O greatly contributes to ozone depletion due to its long lifetime (~150 years) [48]. To reduce NOx emissions, multiple technologies have emerged, among them the selective catalytic reduction with ammonia (NH_3-SCR), technology initially developed by Hitachi Zosen in Japan in the 1970s [49], is one of the most reliable and common method due to the NOx reduction efficiencies, durable performance and reasonable costs. The current industrial SCR processes, in facts, can efficiently reduce up to 90-100% NOx emissions [50] by producing harmless N_2 and H_2O. The catalysts employed for SCR are usually supported V_2O_5/TiO_2 [51][52], mixed $V_2O_5-WO_3/TiO_2$, $V_2O_5-MoO_3/TiO_2$ and for the more recent applications also consist of zeolite-supported Cu and Fe [53]. The former system is successful thanks to high activity and resistance to SO_2 poisoning but suffer the disadvantage that it does not work at reaction temperatures lower than 250 °C, so the SCR must be located upstream of the desulfurizer control device to avoid reheating the gas flow, however in this case the catalyst deactivation is faster due to higher SO_2 exposure. The need to lower investments and to increase thermal efficiency leads to a pressing need for low-cost and low-temperature catalysts (LTC) alternatives as after desulfurizer and particulate removal device the flue gas is relatively clean but with an outlet temperature ≤150 °C [54]. Developing LTC with both excellent efficiency and stability for SCR of NO_x by ammonia is therefore a challenge. Zeolite-based catalysts with their thermal stability can be used at higher temperatures while titania-based catalysts can cover the medium temperatures uses thanks to their high selectivity (as much as ~95−100%) combined with lower costs. In this sector, Mn and Cu-based oxides have been reported to efficiently catalyse SCR reactions at low temperatures similarly to V-based oxide catalysts [55], but doping metal content reaches high values as much as 20% weight content.

Manganese oxides are also interesting due to various types of labile oxygen and oxidation states (Mn^{2+}, Mn^{3+} and Mn^{4+}), which can have a significant role to complete a catalytic cycle [56]. Kijlstra et al. for instance suggested that, in the case of the SCR reaction, it may starts with the transformation of coordinated NH_3 on Mn^{3+} ions to NH_2 species [57]. Furthermore, manganese is a less toxic metal compared to Co, V and Ni and it is relatively abundant with an average upper crustal abundance of 600 mg kg^{-1} [58].

Taking into account all these factors, and aiming to tailor titania catalytic properties, the study of a reliable synthetic route and characterization of TiO_2 nanoparticles, followed by synthesis and characterization of the transitional metal doped counterparts (with Molybdenum and Manganese) has been carried out. Nonetheless, produced materials with appropriate synthetic route, based on their characteristics, have been tested for two real life applications: 1) the NH_3−SCR reactions for Manganese doped TiO_2 and 2) the degradation of the model molecule Rhodamine B in water under low irradiance visible light, with the aim to estimate the photocatalytic capabilities of the synthetized Molybdenum doped nanoparticles.

Chapter 2

Theory

To allow a better reading experience, especially for not-of-the-field readers, as well as provide a resume on the state-of-the-art literature on the topics, it is necessary a brief overview of the main theoretical aspects, information regarding the used materials and techniques, along with the fundamental parameters needed.

2.1 TiO₂ Nanoparticles – Physical and Chemical Properties

More than a decade of research led to advanced understanding of many aspects of nano-TiO₂, from its synthesis to properties and applications. As this is of course true, it is also important to notice that in the vast literature, inconsistences and contradictory results are not so uncommon due to bulk and surface structure−property relationships that add others degree of freedom to the material properties and catalytic performances, obstructing the correct comparison of results from different synthetized materials and the univocal understanding of TiO₂ nanomaterials characteristics.

Due to its modified properties and reactivity at small sizes, nano-TiO₂ finds applications in many innovative areas like solar energy harvesting, photochemical hydrogen generation from water and biomedical implants coatings [59], all of them in addition to traditional applications already listed in the previous chapter of this thesis.

2.1.1 Crystalline, Nanocrystalline and Amorphous Phases of Titania

There are, up to now, 11 reported bulk and/or nanocrystalline phases of TiO₂ which structural characteristics and structures are reported in Table 2.1-1 and figure 2.1-2 respectively, plus one recently discovered high pressure phase. They are: Rutile discovered in 1791 by the British amateur chemist Willem Gregor from ilmenite sand (FeTiO₃), while the name comes by the German geologist Abraham Gottlob Werner in 1800 from the Latin *rutilus*, meaning "reddish"; Anatase, named in 1801 by Rene Just Haüy from greek "ανάτασις" ("anatasis") that means "extension" in allusion to the length of the pyramidal faces being longer in relation to their bases than in many tetragonal minerals (Figure X) [60]; and Brookite, named in 1825 by Serve-Dieu Abailard "Armand" Lévy in honor of Henry James Brooke, amateur English crystallographer and mineralogist [61].

Figure 2.1-1: Typical natural occurring crystals (from left to right) of: Anatase [60], Brookite [61] and Rutile.

These three phases are naturally occurring polymorphs. To these will be later added: $TiO_2(B)$ discovered in 1980 [62] with structure isotypic to that of Na_xTiO_2 (titanium bronze), x~0.2, where the name "$TiO_2(B)$" comes from; two more metastable modifications obtained in ambient pressure synthesis that are hollandite-like ($TiO_2(H)$) discovered in 1989 [63] and ramsdellite-like ($TiO_2(R)$) discovered in 1994 [64]. To these ambient pressure phases, high-pressure polymorphs have been identified confirming theoretical calculations. These structures depend on the pressure and TiO_2 adopts isotypic structures of orthorhombic PbO_2 (columbite-type) $TiO_2(II)$, baddeleyite-like (ZrO_2) at more than 12GPa, cottunite-like ($PbCl_2$) OII [65] between 4-12GPa, pyrite (FeS_2), or fluorite (CaF_2) cubic phase. The cottunite structured has been denoted as the "*hardest known oxide*" [66], later analysed again by other researchers, reporting a bulk modulus of around 300 GPa [67]. The last reported 12th high-pressure polymorph in 2017 is the Riesite which is the result of a retrograde transformation of baddeleyite-type TiO_2 at temperatures between 1000 and 1500K at pressures below 6 GPa. [68][69]

In addition to these crystalline phases, there are at least 3 reported non-crystalline TiO_2 phases: one low density amorphous TiO_2 and two high density amorphous structures. [70][71][72]

Densities for ambient pressure stable phases ranges from the lowest ~3.5 of $TiO_2(H)$ to ~4.2 for rutile g/cm^3, while for high pressure phases their densities range from ~4.3 for $TiO2(II)$ to ~5.8 g/cm^3 for the cubic one. The shape change of the polyhedron is a consequence of the change in the coordination number of Ti from 6 to 7, 8, and 9 due to the pressure increase. Increased edge sharing decreases the Ti−Ti distances and hence increases the structure energy. Hence for the six low-pressure bulk phases, the relative phase stability is in the order: rutile > brookite > anatase > $TiO_2(B)$ > $TiO_2(R)$ > $TiO_2(H)$, which scales roughly with the number of polyhedra per unit cell.

Table 2.1-1: Structural Characteristics of TiO₂ Crystalline Phases. [73]

Phase	Rutile	Anatase	Brookite	$TiO_2(B)$	$TiO_2(H)$	$TiO_2(R)$	$TiO_2(II)$	baddeleyite	OI	OII	cubic
crystal system	tetragonal	tetragonal	tetragonal	monoclinic	tetragonal	orthorhombic	orthorhombic	monoclinic	orthorhombic	orthorhombic	cubic
space group	$P4_2/mmm$	$I4_1/amd$	Pbca	C2/m	I4/m	Pbnm	Pbcn	$P2_1/c$	Pbca	Pnma	$Fm\bar{3}m$
Group number	136	141	61	12	87	62	60	14	61	62	225
a (Å)	4.5941	3.7842	9.184	12.1787	10.161	4.9022	4.515	4.589	9.052	5.163	4.516
b (Å)	4.5941	3.7842	5.447	3.7412	10.161	9.4590	5.497	4.849	4.836	2.989	4.516
c (Å)	2.9589	9.5146	5.145	6.5249	2.970	2.9585	4.939	4.736	4.617	5.966	4.516
α (°)	90	90	90	90	90	90	90	90	90	90	90
β (°)	90	90	90	107.054	90	90	90	98.6	90	90	90
γ (°)	90	90	90	90	90	90	90	90	90	90	90
densitya (g/cm3)	4.248	3.895	4.123	3.734	3.461	3.868	4.329	5.092	5.251	5.763	5.761
polyhedron type	octahedron	octahedron	octahedron	octahedron	octahedron	octahedron	octahedron	augmented triangular prism	distorted augmented triangular	triaugmented triangular prism	cube
#polyhedra per unit cell	2	4	8	8	8	4	4	4	8	4	4
#polyhedra per unit cell volume (1/Å3)	0.03203	0.02936	0.03108	0.02815	0.02609	0.02916	0.03263	0.03839	0.03958	0.04345	0.04343
#edge sharingb	2	4	3								
coordination (Ti)	6	6	6	6	6	6	6	7	7	9	8
lattice energyc (kJ/mol)	0	24.75	18.53	49.16	73.05	68.49	8.86	155.55	141.07	141.97	147.78
high pressure?							yes	yes	yes	yes	yes
reference	ICDS 9161	COD 9008213	ICDS 15409	ICDS 41056	COD 1008514	ICDS 75179	ICDS 15328	COD 9015355	ICDS 173960	ICDS 27736	ICDS 44937

Anatase

Rutile

Brookite

TiO$_2$ (B)

TiO$_2$ (H)

TiO$_2$ (R)

TiO$_2$ (II)

Baddeleyite

OI

OII

Cubic
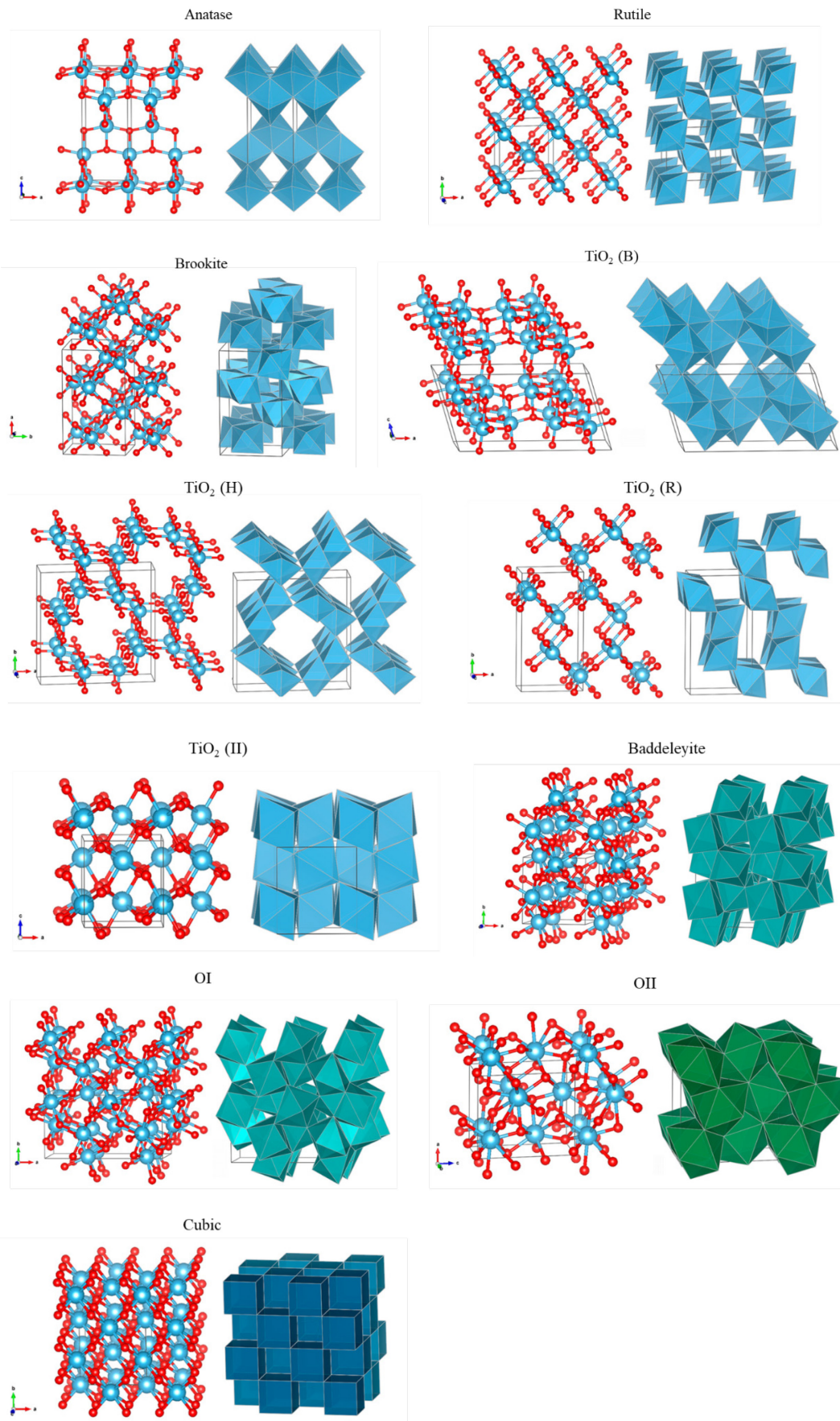
Figure 2.1-2: Structures of TiO$_2$ phases in the ball-and-stick and polyhedron models where red balls are O atoms and blue balls Ti atoms. Thin line cages represent the unit cells. [73]

2.1.2 Effects of nanoparticles size in TiO₂

It is known that particle size affects many physical-chemical properties of matter. One of the effects regards the structural characteristics, such as surface stress and lattice contraction/expansion. Zhang et al [74], Eltzholtz et al [75] and Matěj et al [76], synthetized nearly spherical anatase nanoparticles with sizes in the range 4-35nm, 7-35nm and 3-25nm respectively with different synthetic routes; Their results showed a decreasing in cell volume and negative strains (contraction) in both a and c axis (figure 2.1-3) that increases in magnitude by decreasing particle size as one can expect due to "structure strain". Depending on the environment and synthetic conditions, these results are not always with the same trend, as a preferred growth direction or the presence of ligands and their binding strengths may influence surface stress: stronger binding could result in a negative surface stress (positive strain) and hence a lattice expansion at small sizes. [77][78]
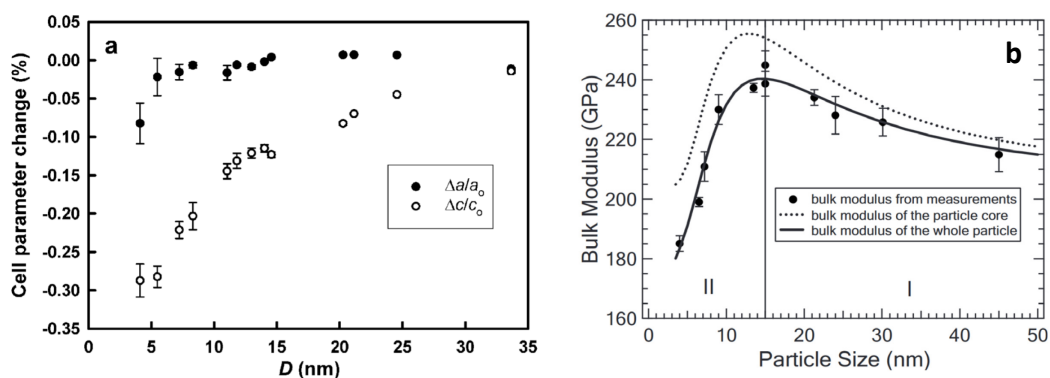
Figure 2.1-3: a) cell parameter change with anatase nanoparticle diameter due to structural strain [74], **b) size dependence of the bulk modulus** [79]. **The solid curve represents the effective bulk modulus (whole particle), the dashed curve represents the bulk modulus of the particle core only. Reprinted with permission. Copyright of respective journals.**

A positive strain/increase in cell volume with decreasing nanoparticle size can also be possible due to the presence of surface defect dipoles caused by the distortion of the Ti-O octahedra [80] and Ti^{4+} vacancies [81].

Mechanical properties of nano-TiO₂ also depend on size. Chen et al [79] found that bulk modulus follow the trend in figure 2.1-3 b, where the highest value of 240GPa is for nanoparticles of around 15nm. This trend was explained with two main contributions: by decreasing nanoparticles size the bulk modulus is firstly increased due to the enhanced overlap of dislocation strain fields, but under 15nm arises the inability to retain dislocations inside the small particles, which are also at high pressure due to surface stress.

2.1.3 Electronic structure

Ti atom in TiO₂ donates its 3d and 4s valence electrons to the oxygen 2p orbitals and so have empty d band. TiO₂ is a wide-band-gap semiconductor, the band gap energy values for phase pure TiO₂ are reported in table 2.1-2. Titania, both natural

and synthetic is usually slightly oxygen-deficient, TiO_{2-x} (x ≈ 0.01). The vacancy defects, the absence of the atoms/ions from the lattice structure, are very common in all types of crystalline materials. These point defects in the lattice are formed to minimize the Helmholtz free energy for the establishment of thermodynamic equilibrium and can effectively alter the charge distribution - electronic energy levels near the defect site. Moreover, oxygen vacancies (V_O) have the lowest formation energy among the various defects. This small oxygen deficiency, which can also be considered as Ti^{3+} impurity, provides n-type doping to the semiconductor material, which act as donors in semiconducting metal oxides, which play crucial roles in defining various physical and chemical properties of the material such as (ferromagnetism, superconductivity, phase transition, photocatalytic effect, photoelectrochemical performance, piezoelectric response, redox activity, etc [82]). For instance, as an n-type semiconductor, it acts as a photoanode in an electro-chemical cell upon photoexcitation across the band gap.

Band structure and density of states (figure 2.1-4) for Anatase, Rutile and Brookite have been calculated by Zhang et al [83] using DFT calculations, while the electronic structure of TiO_2(B) was calculated by Nuspl et al [84]. From these works results that anatase appears to be an indirect band gap semiconductor, while rutile and brookite belong to the direct band gap category. As a result, indirect band gap anatase exhibits a longer lifetime of photoexcited electrons, property that can be useful in photocatalytic applications. In addition, from the simulations, anatase has the lightest average effective mass of photogenerated electrons and holes as compared to rutile and brookite, which implies a fast migration of

Figure 2.1-4: band structure and DOS for anatase (a), rutile (b) and brookite (c). [83]
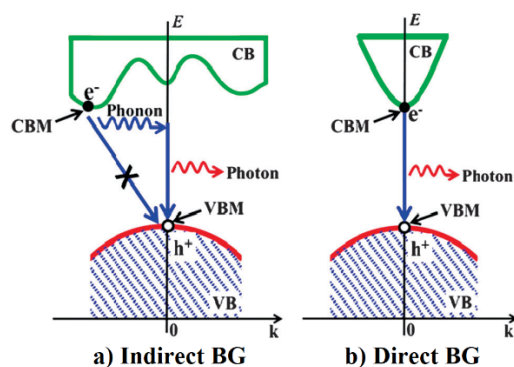
charges that can move to the surface, resulting in the lowest recombination rate of photogenerated electron-hole pairs [83]. From the calculations is also possible to underline how the valence bands DOS primarily consist of O 2p states (black lines) and a few Ti 3d states (blu lines), indicating the strong p–d hybridizations between the two states (bonding states), while the conduction bands are mainly composed by Ti 3d states, mixed with a few O 2p and Ti 3p states (red lines). Strong hybridization also appears between p-d conduction states (antibonding states).

TiO$_2$(B) is a semiconductor with a band gap of 3 - 3.2 eV. Similar to anatase and rutile, also the n-doped TiO$_2$(B) shows photoanodic and photocatalytic activity in UV light, sometime reported to be even superior to that of Degussa P25 [85], the material considered to be all purpose photocatalyst with excellent performance. The unique properties of P25 arise from its special composition that is actually a mixture of anatase and rutile with some amorphous portion in a ratio of about 78:14:8 respectively [86]. In facts, samples containing a mixture of anatase and rutile, outperform pure phase samples [87][88] (depending also on crystallites sizes) due to the band alignment of around 0.4 eV between anatase and rutile, with anatase possessing the higher electron affinity.

Table 2.1-2: Phase pure energy gap values of the natural occurring TiO$_2$ phases.

	Eg (eV)	Ref. (Eg)
Anatase	3.19 - 3.23	[89][90][91][92][93]
Rutile	3.0 - 3.031	[89][90][91][93][94]
Brookite	3.1 - 3.4	[90][91][95]

2.1.4 Raman features of TiO₂ polymorphs

Many studies have clearly established that anatase (tetragonal, space group: I4$_1$/amd) structures have 6 Raman-active modes (A_{1g} + 2B_{1g} + 3E_g) with characteristic scatterings at 146 (E_g), 396 (B_{1g}), 515 (A_{1g}) and 641 cm^{-1} (E_g) [96][97][91]; brookite (orthorhombic, space group: *Pbca*) structures have 36 Raman-active modes (9A_{1g} + 9B_{1g} + 9B_{2g} + 9B_{3g}) with commonly visible peaks at about 128 (A_{1g}), 153 (A_{1g}), 247 (A_{1g}), 322 (B_{1g}), 366 (B_{2g}), and 636 cm^{-1} (A_{1g}) [91][98][99][100][101], while rutile (tetragonal, P4$_2$/mnm) have 4 (A_{1g} + B_{1g} + B_{2g} + E_g) Raman active modes which gives typical scatterings at 143 (B_{1g}), 235 (two-phonon scattering), 447 (E_g), and 612 cm^{-1} (A_{1g}) [91][97].
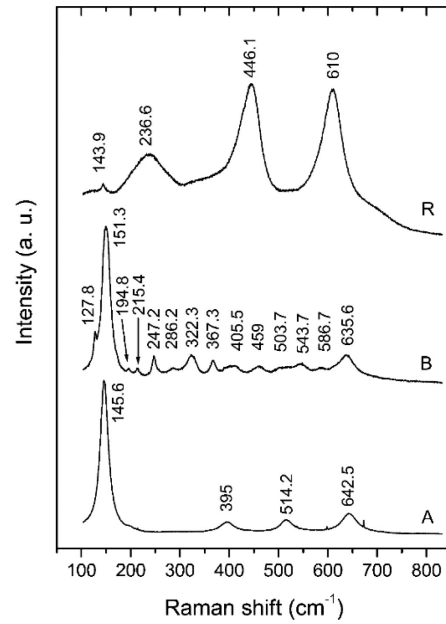
Figure 2.1-6: Raman spectra of the three phase-pure powders (A=anatase, B=brookite, R=rutile) [91]
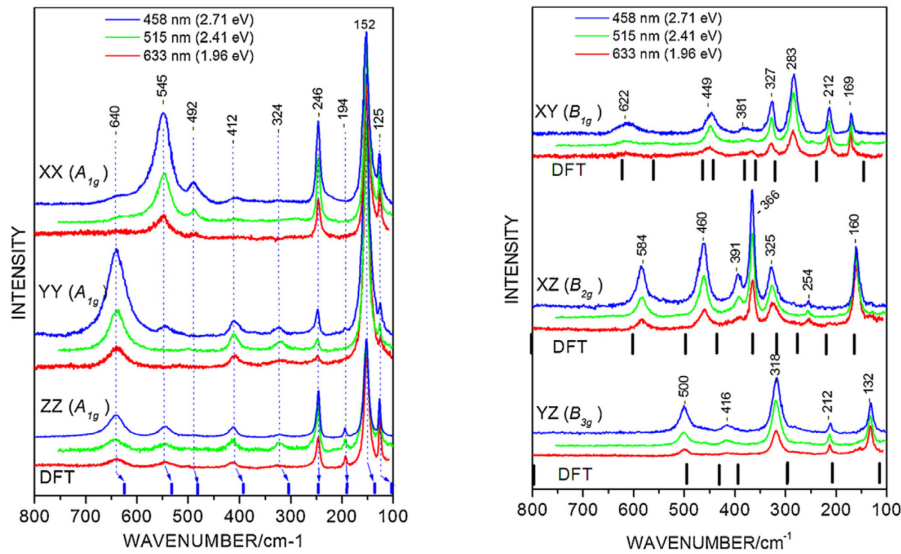
Figure 2.1-7: Raman spectra of brookite crystal at 300 K at different laser sources excitation and polarizations direction. DFT-calculated values are shown at the bottom. Reprinted with permission. Copyright of respective journal. [98]

2.3 Solution-Based Synthesis Methods of Titanium Dioxide Nanoparticles

Literature provides hundreds of methods to prepare nanoparticles and nanostructures. We can firstly distinguish physical, chemical and bio-assisted methods as well as top-down and bottom up methods classification. Physical methods usually depend on the top-down approaches where small particles are obtained from larger ones. Physical methods usually apply mechanical stresses, high energy radiations or thermal or electrical energy to cause material melting/evaporation/condensation or abrasion, exfoliation or atoms/clusters sputtering. Some examples are high energy ball milling (HEBM) [102], laser ablation (LA), electrospraying, inert gas condensation (IGC), physical vapour deposition (PVD), melt mixing. These methods can be advantageous as they are free of solvent contamination and are most suited to produce large quantities of material but often lacks in size resolution control (tens of nanometres).

In contrast, chemical/bio assisted methods proceed uses in most cases (but not always) a bottom-up approach, in which molecular precursors react to grow a larger structure. Some examples of bottom-up methods include self-assembly of monomer/polymer molecules, chemical or electrochemical precipitation, sol–gel methods, chemical vapour deposition (CVD), laser, plasma and flame (FSP) pyrolysis synthesis and bio-assisted synthesis. Most commonly used chemical methods for NPs synthesis, are sol–gel techniques, microemulsion methods, hydrothermal, chemical vapour synthesis and plasma enhanced chemical vapour deposition (PECVD).

Bio-assisted methods also known as biosynthesis or green synthesis, provides a low-toxic, cost-effective and efficient routes to synthesize NPs. These methods employ plant extracts, bacteria, fungi, viruses, yeast, actinomycetes, and other biological systems to produce nanoparticles like Ag, Au, Pd, TiO2, CdS and many other by, for instance, turn the metal ions into the element metal through enzymes. Lactobacillus bacterium as an example was used for the synthesis/nucleate/grow of Au, Ag and TiO_2 NPs [103][104], as well as there are many reports on the NPs biosynthesis of SiO_2, TiO_2 [105], magnetite [106], and ZrO_2 [107] using fungal species.

Chemical ways are performed at a smaller scale but with resolutions that can approach the atomic-layer limit [108]. For this reason, in a context of material characterization and laboratory scale production, such as in this research work, the latter is preferred, especially solution-phase methods where long organic molecules can be used as protecting structure and/or directing agents in solution to control/limit the growth and the nanoparticles size. The choice of the synthetic method depends on important factors, such as the consideration that the conversion of a heterogeneous catalytic reaction takes place over the surface of materials and therefore, increasing the number of active sites and their nature are somewhat priorities in the material design. Thermal stability is another issue that can be optimised by other strategies like exploiting the use of supports of different

materials that are more thermally stable [109]. In this context, supported metal oxide catalysts are usually prepared by impregnation, ion-exchange, coprecipitation and deposition precipitation methods [110] or using "one-pot" routes such as sol-gel technique.

The sol-gel method refer nowadays in the synthesis of solid materials from solution-state precursors (wet chemistry) which require low temperatures in contrast to more classical methods [111], which can be a big advantage in terms of process energy consumption and thus CO_2 emissions. Classically the term "sol" refers to the colloidal suspension of solid particles in a liquid, while "gel" refers to polymers containing liquid as this process consist in the creation of suspensions in the liquid that lead to the formation of a network of particles [112] through hydrolysis and condensation steps, where respectively water disintegrate the bonds of the precursor to start the first step in formation of the gel phase, followed by condensation that leads to the formation of nanomaterials where the excess water is removed. The fundamental steps of the sol-gel method can be summarized as follows:

i. Preparation of the solution of precursors;
ii. Hydrolysis and partial condensation of alkoxides ($M(OR)_x$ where R is the alkyl group). A nucleophilic substitution of a water molecule results in the replacement of an alkoxy group with a hydroxyl one (MOH) with the alcohol (R-OH) as the leaving group (reaction n° 1) [112][113];
iii. Formation of the gel via polycondensation of two hydrolyzed precursors (M-OH species) (reaction n°2 and 3) to form a three-dimensional polymeric network (the gel);
iv. Drying the gel to form a dense "xerogel" caused by the evaporation of the solvent and consequent collapse of the gel network, or an aerogel through supercritical drying;
v. Heat-threatment/calcination to obtain mechanically stable materials.

$$\equiv M-OR \ + \ HOH \ \rightleftharpoons \ \equiv M-OH \ + \ ROH \quad (1)$$
$$\equiv M-OH \ + \ \equiv M-OH \ \rightleftharpoons \ \equiv M-O-M\equiv \ + \ HOH \quad (2)$$
$$\equiv M-OH \ + \ \equiv M-OR \ \rightleftharpoons \ \equiv M-O-M\equiv \ + \ ROH \quad (3)$$
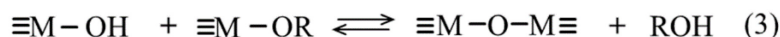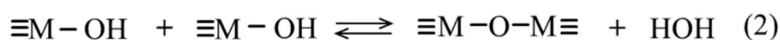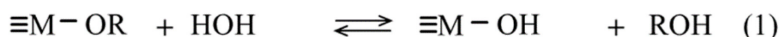
The choice of precursors, solvents and their percentage, pH of the solution, water content, type and concentration of additives (catalysts, surfactants, structure directing agents), reflux temperature and time, pre- and post-heat treatment and temperatures, drying methods and aging time are some of the main parameters that can be used in order to achieve the desired nanomaterial. Reaction rates, for instance, depends on and increases with the increase in the difference (N-z) (coordination number and the charge of the element M respectively) [112], while decrease with steric encumbrance of the alkoxide in accordance with a nucleophilic substitution mechanism. In the case of non-metal alkoxides (e.g. Si, P, Ge), the rates

of hydrolysis are slower compared to metal alkoxides where the M-O-R bonds are usually high polarized. For this reason, mixed oxide preparation can be tricky as the different rate of hydrolysis can lead to different gelation times and consequently phase separation.

2.3.1 Template assisted sol-gel synthesis

A subcategory of sol-gel method is the template assisted sol-gel synthesis (TASG), where reactions take place in a confined environment by exploiting the self-assembly of molecules into a remarkable range of nanostructures depending on the environment, such as the self-assembly of lipids or surfactants molecules immersed in two mutually immiscible components which are usually a polar (usually water) and non-polar (usually a hydrocarbon liquid or oil) phases or, environmentally-viable supercritical carbon dioxide [114][115] that solve the problems of difficult separation and removal of solvent from products in conventional reverse micellar syntheses. To reduces the interfacial tension, in facts, surfactant molecules creates an interfacial layer separating the polar and the non-polar phases. Parameters such as surfactant shape and type, solvent properties (e.g ionic force), pH and other physical properties as temperature and pressure determines the final thermodynamically stable phase structure. Some examples are micelles (spherical aggregates), cylindrical and lamellar structures. A schematic phase diagram is reported in figure 2.3-1, whereas figure 2.3-2 shows the effect of surfactant shape over the final phase structure [116][117].
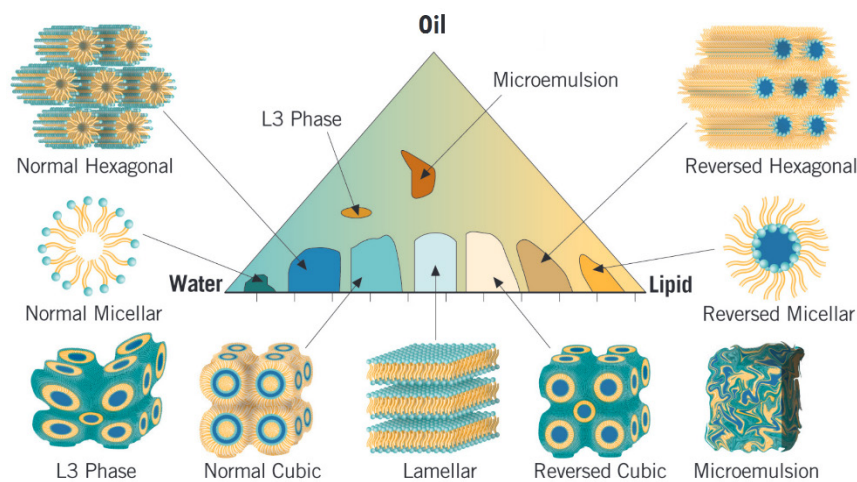
Figure 2.3-1: Schematic phase diagram as a function of the three components composition. [116]
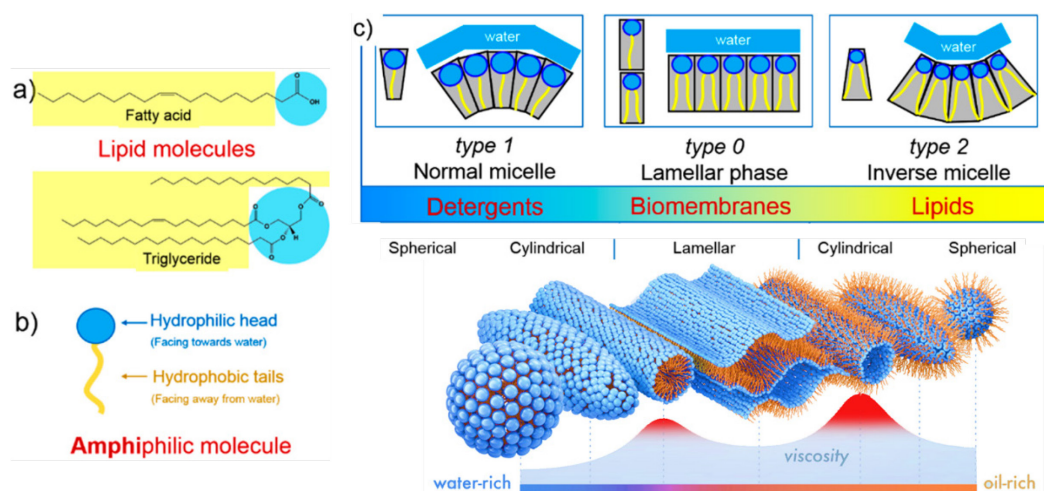
Figure 2.3-2: (a) Two examples of typical lipid molecules; (b) Schematic of an amphiphilic molecule with the hydrophilic and hydrophobic parts; (c) Average shapes of self-assembling in water/oil; Adapted from [116] and [117].

Surfactants exists in countless compositions, shapes and different types as shown in figure 2.3-3. We can distinguish ionic surfactants (cationic and anionic) such as carboxylic acids and amines, non-ionic as alkyl ethoxylates or esters that carry no charge and are relatively non-toxic [118] and finally a special class of zwitterionic and amphoteric surfactants which possess both charges in different regions of the chain that are used for special needs. Every class has its peculiar characteristics and behaviour: ionic surfactants like tetradecyltrimethylammonium bromide (TTAB) aren't affected greatly by temperature as can be seen from the phase diagram in figure 2.3-4 contrary to the non-ionic counterpart as tri-block-copolymers such as Pluronics®: for them it has been shown [119] that the aggregation number increases with temperature, while the core, as expected, become dehydrated at higher temperatures, therefore non-ionic surfactants are more susceptible to temperature changes due to the change in solvent properties and subsequently interaction with the polar groups (e.g swelling) as shown in the phase diagram of P85 non-ionic surfactant (figure 2.3-4 right) [120].

22
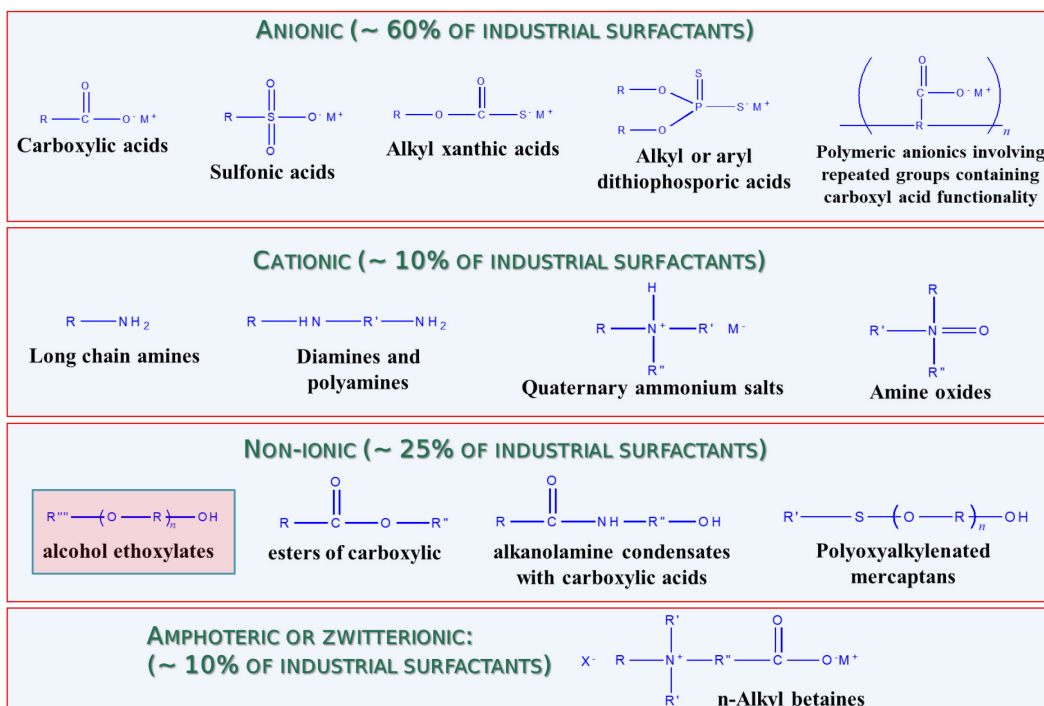
Figure 2.3-3: Main types of surfactants with examples and molecular structures.
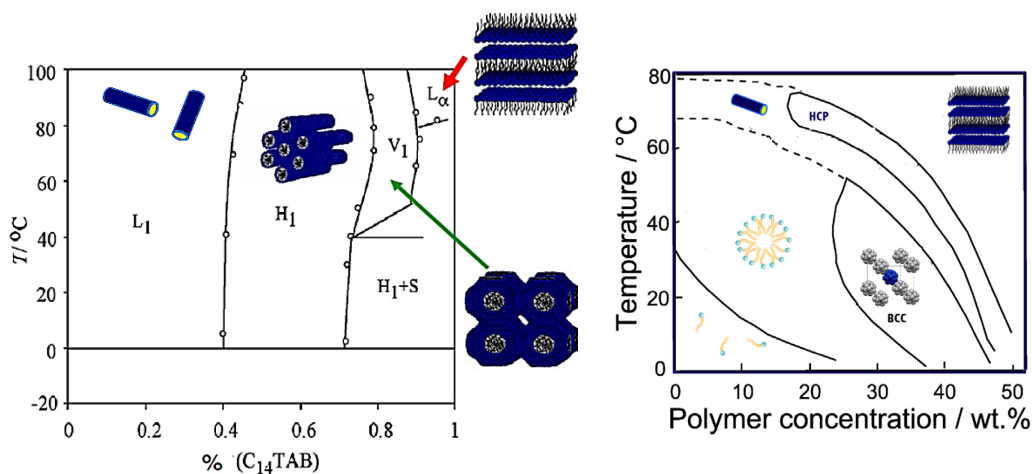
Figure 2.3-4: Phase diagrams of (left) the TTAB ionic surfactant and (right) the non-ionic P85 tri-block-copolymer (adapted from [120]**).**

Is therefore possible to exploit many parameters in order to tune the nanoreactor size and shape of a template assisted synthesis. In this work, we opted for a non-ionic surfactant (a polyoxoethylene-oleyl-ether) as it is a flexible choice (temperature tuneable) and can be potentially recycled after use by solvent extraction. In facts, non-ionic surfactants are the most common type used in preparing micelles due to stability, compatibility, low toxicity and tend to not change the physiological pH in solution compared to their anionic, amphoteric or cationic counterparts [121][122].

The water/oil reverse micellar system acts as an excellent reaction site for the NPs synthesis. The template assisted synthesis with reverse micelle is known since the 1960s but only used as nano-templates for materials synthesis of monodispersed metal particles of Pt, Pd, Rh and Ir in 1982 [123]. Even though the reverse micellar system is heterogenous, it is an equilibrium system and thus thermodynamically stable as the interactions between polar head-groups of the surfactant molecule and the nonpolar tails favour only aggregates of a very specific size and configuration, so the microemulsions typically have narrow droplet size distributions.

The sol-gel method within reverse micelle presents different advantages:

- micelles can solubilize high amount of polar solvent present in the medium with increasing the water or polar components/surfactant ratio;
- has excellent control of the final powders stoichiometries;
- is able of atomic scale mixing;
- reach narrow sizes distributions with control of sizes and shapes as the surfactant molecules creates a layer separating the polar and apolar phases acting as a steric barrier which prevents the coalescence of the droplets and particle nucleation can be initiated simultaneously at a large number of locations (inside the micelles), well isolated from each other;
- obtained particles might also be extremely well dispersed;
- low energy consumption (low temperature);
- use of simple equipment;
- is a flexible method in terms of composition and precursors that can be used, along with doping materials.

To achieve reverse micelles or other structures it is necessary to reach specific range of water/oil/surfactants composition and especially water/surfactant molar ratio (ω) and the critical micelle concentration (CMC), which is the minimal concentration of surfactant molecules above which micelles are formed that are function of surfactant types and physical-chemical properties of the environment, such as ionic force (especially for ionic surfactants where the effective dimension of the polar head is a function of it), pH and temperature (that is instead especially important for non-ionic surfactants as it changes the solubility and so the swelling of the polar section). Usually, the higher the ω, the larger the water pools of the micelles and the nanoparticles formed within, and *vice versa*. Although such a correspondence between the size of the synthesized nanoparticle and the parameter ω was approved in many experiments, it has been put into question lately, since within a number of performed syntheses a similar correspondence could not be established. Zhang et al. for instance have studied the

Figure 2.3-5: Interface curvature as a function of the packing parameter P.

synthesis of Ag NPs within reverse micelles and the effect of the ω parameter on the particle size and their size distribution. Their studies revealed that there is continuous decrease in the particle size from 5 to 1.5 nm decreasing the ω value from 15 to 2.5 [124]. Aziz et al [125] found that, by increasing the molecular weight of chemical modifier reagent or decreasing calcination temperature, NPs size decreases. An increase of polar head group volume increases particle dimensions, whereas increasing polarity of hydrocarbon tails have the opposite effect as reported in a study of the hydrodynamic diameters of reverse micelles of different non-ionic surfactants di-block copolymer (brij-52, brij-56, brij-58 and brij-93) in ethylammonium nitrate/benzene emulsion [126]. Other researchers reported that the size of reverse micelles (hydrodynamic diameter) of non-ionic surfactants (e.g triton-X-100) increase as ω ratio increases [127][128].

Phase diagrams, along with the packing parameter (P) (figure 2.3-5) or more advanced models as the net and average curvature framework [129] with the hydrophilic−lipophilic parameter (H) [130] can be useful tools to guess the starting point for a correct emulsion composition and temperature.
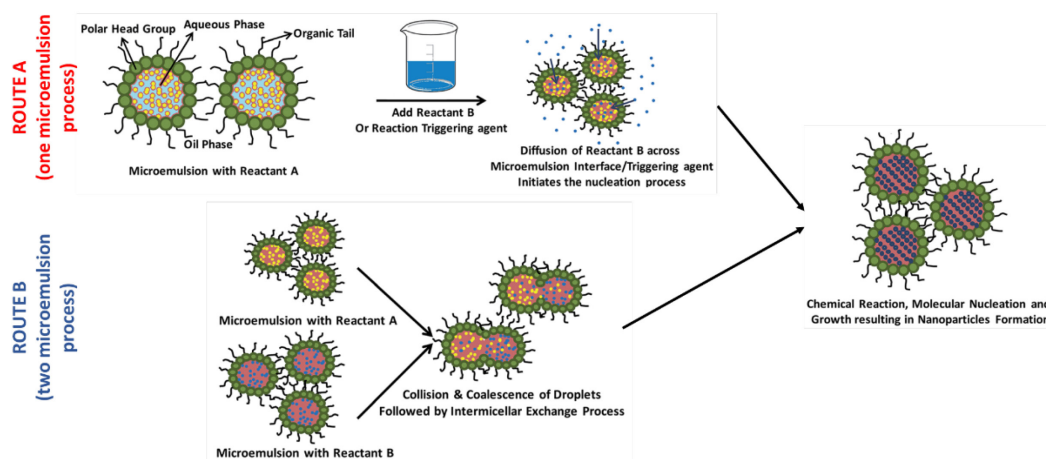
Figure 2.3-6: Typical reverse micelle system and microemulsion routes to synthesize NPs. Adapted from [124]

Within reverse micelle method, we can distinguish two main microemulsion synthesis routes as shown in figure 2.3-6: In route A, microemulsion processes are diffusion controlled since the reactant B must diffuse through the interface encapsulating the reactant A. In route B instead, the two microemulsions carrying the separate reactants are mixed together in appropriate ratios, while Brownian motion of the micelles lead to intermicellar collisions that, if sufficiently energetic, leads to the mixing of the micellar components allowing the chemical reaction to take place in this nanoreactor.

2.4 Molybdenum

Its name is derived from 'molybdos', the Greek word for "lead", discovered by the Swedish chemist Peter Jacob Hjelm but incorrectly regarded as a lead ore because its black molybdenite ore is similar to graphite in appearance until it was analysed by the German-Swedish chemist Carl Wilhelm Scheele in 1778 [131], whom research proved that it was neither graphite nor lead but could not isolate the metal. Later, Peter Jacob Hjelm by using carbon, molybdic acid and linseed oil was able to
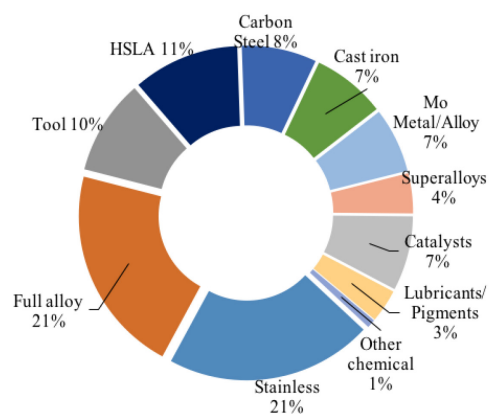
Figure 2.4-1: Molybdenum consumption (2016) [133]

produce molybdenum metal by heating this paste. The new element was than announced in the autumn of 1781. Its average abundance in the earth's crust is about 1 mg/kg or 1 part per million (ppm) and is one of the most highly concentrated trace elements in sea water at 10 parts per billion (ppb) [132].

Molybdenum is an element with a rich chemistry, vital within the biosphere for the activity of a large group of enzymes and have many versatile applications, such as in metallurgy thanks to its anti-wear properties as lubricants particularly in extreme environment, as pigments as they are non-toxic and act as efficient corrosion inhibitors and smoke suppressants. Molybdenum is used in steel to make lighter and stronger alloys that have been in high demand in the aerospace and automotive sector, or in cast iron to improve strength, weldability and corrosion resistance. Among other non-metallurgical uses, catalysis represents the 7% of the consumption in 2016 and increasing. It is estimated 60 percent of global molybdenum supply comes as a by-product of copper smelting while the remainder comes from primary molybdenum mines [133].

Thanks to its many oxidation states (±1 ±2, +3, ±4, +5, +6) and coordination numbers (from 4 to 6), Molybdenum can form multiple Mo-Mo bonds and compounds with most inorganic and organic ligands, resulting in many catalysis applications. Molybdates are in fact used as catalysts for the selective oxidation of olefins to unsaturated aldehydes and acids, in the synthesis of acmylomitride by the ammonoxidation of propane by bismuth molybdate, and in the liquefaction of coal. The use of molybdenum compounds in homogeneous catalysis is also significant.[134]

The element is located in the 4d-block between Nb and Tc, has six valency electrons and nine atomic orbitals. In the metal oxidation state, the efficient overlap of the 4d-orbitals and the number of bonding electrons available is reflected in its high strength of interatomic bonding. In fact, with a moderate Pauling electronegativity (1.8), all six valency electrons are available for chemical bonds in contrast to the more electronegative later d-block transition metals which normally

use up to two electrons. Molybdenum ions have also relatively large radii (Table 2.3.1-2) [135], which imply a low polarity, higher coordination numbers (CN) are usually observed and for many molybdenum compounds the observed CN is 6 as, for example, with MoO_3 where the molybdenum ions occupy octahedral sites. This coordination is comfortable to avoid steric overcrowding or unsaturation, in contrast with the larger lanthanides, where CN of 7-8 are common. Lower CN may reflect the requirements of the 18-electron rule, or, the presence of bulky ligands, whereas higher CN arise when small ligands are present, especially when combined with an 18-electron environment.

Property		Mo
Atomic number		42
Electronic configuration		$[Kr]4d^5 5s^1$
Valency orbitals		4d 5s 5p
Ionisation enthalpies	1st	685
ΔH^{π}_{ion} (kJ mol^{-1})	2nd	1558
	3rd	2618
	4th	4480
Electronegativity		1.8
Radius of atom in metal (pm)		139
Ionic radii for six co-ordination (O.S.), (pm)		59 (VI) - 69 (III)
MP/°C		2623
BP/°C		4650
Temperature at which evaporation is 1 gh^{-1}cm^{-2},		2610
ΔH_{vap}/ kJ mol-1		590 (± 21)
$\Delta H_{formation}$ (monatomic gas)/ kJ mol-1		664 (±13)
Atomic weight		95.94
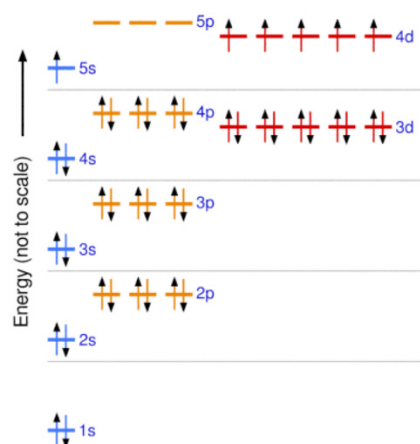
Table 2.4-1: Fundamental properties of molybdenum and electronic configuration

The d-band is divided into halves by a deep minimum which is characteristic of body-centered cubic (Fig. 2.3.1-2 [136]), whereas a continuous *d* band is typical of face-centered cubic metals [137]. As consequences, the melting point of Mo is 2623°C so it is a 'hot strength' material. Mo is resistant to most chemical reagents but can be attacked by oxidising acids and fused alkalis. In air it oxidises slowly at 350°C and rapidly above 650°C, a weakness for high temperature uses in atmospheres containing water or NO_x. Its relatively low thermal neutron cross section makes it suitable for nuclear applications.

27
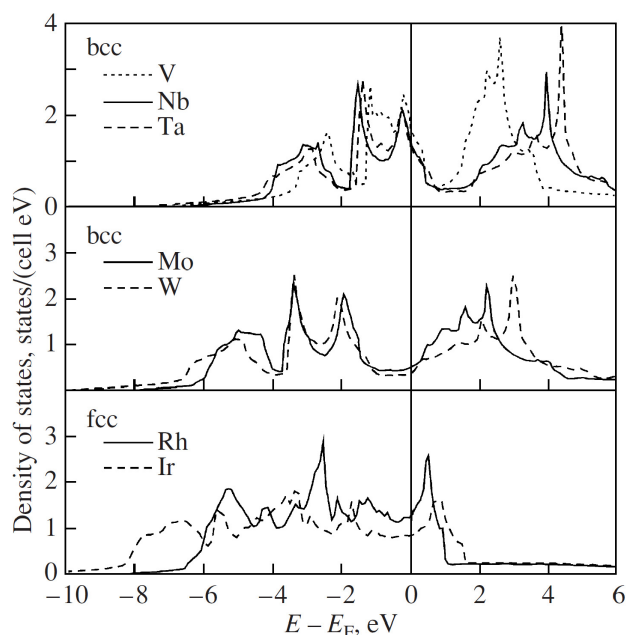
Figure 2.4-2: Calculated densities of states for transition metals with a cubic structure from the 3*d*, 4*d*, and 5*d* periods of the periodic table (vanadium, niobium, tantalum, molybdenum, and tungsten with a BCC structure, rhodium and iridium with a FCC structure). [136]

Table 2.4-2: Shannon-Prewitt Effective Ionic Radius and coordination numbers of Molybdenum. [135]

Ion charge	Coordination number	Shannon-Prewitt Effective Ionic Radius (pm)
+3	6	69
+4	6	65
+5	4	46
	6	61
+6	4	41
	5	50
	6	59
	7	73

There are many molybdenum compounds with homopolar Mo-Mo bonds, as well as many compounds with strong covalent bonds to other elements. The oxidation state principle is not useful for the classification of these compounds in the same manner of organic compounds. An example is the $[MoO_3]_n$, which can be described as covalent polymer. For these reasons, molybdenum compounds are classified with a notation composed by 3 functions of the ligands attached as following: $MoL_lX_xZ_z$ where l, x and z are integer numbers including zero. X is a singly occupied orbital on the ligand, L is a filled orbital containing two electrons which are donated to an empty orbital on the metal and Z is an empty orbital on the ligand which can accept the donation of an electron pair from the molybdenum. In figure 2.3.1-3 are represented: (i) only the orbitals for the Pπ-X-function, (ii) only the orbitals for the $\rho\pi$-L-functions, (iii) only the orbitals for the Pπ-Z-function. The shading of orbitals indicated they are occupied by two electrons, while white orbitals have no electrons or one electron (small arrow inside).
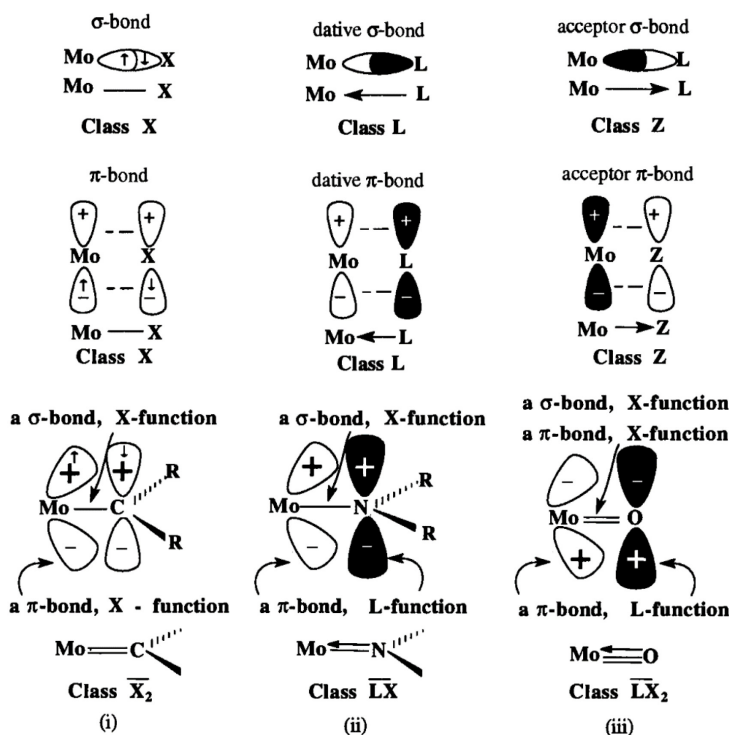
Figure 2.4-3: Relationship between the nature of the primary molybdenum-ligand bonding and the class of the ligand for monodentate ligands (only a single ligating atom). [138]

The oxides of molybdenum, used in a variety of industrial applications, for example as catalysts, are many and diverse in chemistries and structures. There are: binary oxides (dioxide, trioxide, and intermediate phases of general formula Mo_nO_{3n-m} (with n for instance up to 8 or 9 and m=l); ternary oxides are even more diverse, like polymolybdates (Mo^{VI}), bronzes (compounds with generic formula $A_xMo_yO_z$ where A may be hydrogen, Ti^+ or an alkali metal cation), insertion compounds containing typically (Mo^V / Mo^{IV}), and metal cluster compounds with molybdenum in oxidation states down to 2.5. Another special feature of Molybdenum is the apparent coexistence of oxidations states of Mo^{VI} Mo^V and Mo^{IV}, characteristic not present in the neighbouring elements Nb and W, or likewise the ability for Mo^{VI} to assume different geometries in contrast to Cr^{VI} and W^{VI}. For a detailed discussion the reader can refer to the excellent and complete work of Braithwaite et al [138].

Molybdenum in heterogeneous catalysis

Transition metals are widely used as catalysts of a great number of different reactions. In particular, regarding Molybdenum, few important examples are the hydrodesulfurization of petroleum on Mo-based catalysts which is one of the most important heterogeneous catalytic processes employed [139], the liquefaction of coal, the selective oxidation of olefins to unsaturated aldehydes and acids [140] and the synthesis of acrylonitrile by ammoxidation of propene on bismuth molybdate. Some other important examples and a comparison of Mo-compounds type with their applications are reported in table 2.4-3 and 2.4-4 respectively. As can be seen there are reactions involving hydrogens or oxygens, addition or decomposition

which are usually classified as acid-base processes, as well as reactions of isomerization and polymerization.

Reaction	Example	Catalyst	T	Conversion and Selectivity or yield (y)
Isotopic exchange	$H_2 + D_2 \rightarrow 2HD$	MoO_3/Al_2O_3	80	High
Isomerization (structural)	n-pentane $\rightarrow$ isopentanes	MoO_3/Al_2O_3	425-450	50 95
Ring contraction	Cyclohexane $\rightarrow$ methyl cyclopentane	MoO_3/Al_2O_3	455-495	y=37
Epoxydation	Propylene + $H_2O_2 \rightarrow$ propylene oxide	MoO_3 (in H_2O_2 + pyridine)	60	80 100
Polymerization	Ethylene $\rightarrow$ polyethylene	MoO_3/Al_2O_3	200-260	50 _
Dehydratation	Isopropanol $\rightarrow$ propylene	MoO_3	191-224	100 _

Catalyst	Application	Reaction
S-Co-Mo or Ni-Mo on Al_2O_3	Hydrotreating, hydrodesulfurisation	Remove S from crude petroleum
Bi-Mo oxides	Propene selective oxidation, ammoxiation	Synthesis acrolein, acrylonitrile
Mo-V oxides	Acrolein oxidation	Synthesis acrylic acid
Fe-Mo oxides	Methanol oxidation	Synthesis formaldehyde
Mo oxide on Al_2O_3	Olefin metathesis	Propene to ethene and butene
Mo complexes	Epoxidation	Olefin to epoxide
Heteropolyacids-phosphomolybdate	Propene hydration	Propene to alcohol

Catalytic behaviour is somewhat difficult to relate to single physical-chemical feature, nonetheless one important parameters is the oxidation state: Fiedor et al [141], in a study of Mo oxides over TiO_2 support found the distribution of Mo oxidation states at different degrees of reduction with hydrogen. From this data and the catalytic yield for different reactions it was concluded that the insertion of oxygen in hydrocarbon molecules is catalysed by the oxide of Mo^{6+} [142], while metathesis of propene involves Mo^{4+} ions as active centres. Results indicated that

Mo oxidation states $\leq +4$ are required for propene hydrogenation as Mo^{3+} ions are the main active centres for hydrogenation reaction, whereas hydrogenolysis require the presence of Mo^0 metal atoms [143].

Chapter 3

Synthesis and Characterization of Titania and Metals Doped Titania

3.1 Introduction

Literature and patents provide many synthetic routes to produce TiO_2 nanopowder [144][145]. Out of the different syntheses reported by the literature, the reverse micelles method proposed by Chandra et al [146] allows obtaining high surface area of doped TiO_2, SiO_2 and ZrO_2 NPs. By such method, the self-assembly of surfactant molecules in the organic phase produces a "nanoreactor" where reactions in water phase take place; the size of the reverse micelles, tuneable through the polar head group and the alkyl tail length and structure, allows controlling both size and shape of the NPs [126] as explained in the previous chapter. The reverse micelle core provides a suitable environment for the controlled nucleation and growth of TiO_2 NPs, simultaneously affording a good dispersion of metal oxides MoOx and MnOx species as consequence of Mn and Mo doping. Micelles nanoreactors have been produced by using the non-ionic Brijs surfactant which consist of varying numbers of polar head group containing polyoxyethylene groups that can be solvated by H-bonding, giving them a stronger amphiphilic character and a separate hydrophobic tail consisting of polymethylene chain. This approach will be regarded as "reverse-micelle template assisted sol-gel method".

3.2 Undoped Titania

The most used commercial TiO_2 is the P25, from Degussa (recently named Evonik-Degussa Airoxide) that consist of a rutile/anatase mixture around 20/80 ratio, respectively. P25 is an efficient photocatalyst under UV illumination and is commercially synthesized through a flame hydrolysis process of titanium tetrachloride that produce highly fine aggregates formed by anatase and rutile, intensively interlinked between them [147].
High surface area NPs, possibly characterized by hierarchical inter-and/or intra-particle porosity, can be obtained by using soft templates in order to improve the material catalytic activity and to facilitate the diffusion of reagents/products [148]. For instance, mesoporous TiO_2 particles have been obtained by using either a triblock copolymer (*e.g* Pluronic P123) or an ionic surfactant (*e.g.* cetyltrimethylammonium bromide), whereas when di-block copolymers are used (*e.g.* Brij-n) porosity forms among the NPs [148].

Non-doped TiO₂ powders studied in this work were obtained by two types of templated assisted sol-gel (TASG) synthesis and one sol-gel (SG) synthesis carried out at acidic pH in the absence of any template. In details the three synthetic routes were the following and schematised in figure 3.2-1:

a) a TASG method in the presence of a tri-block copolymer forming micelles in water/ethanol, so to obtain TiO₂ NPs characterized by both intra- and interparticle mesoporosity (M-TiO₂ sample);

b) a reverse-micelle TASG method, where a di-block surfactant is used in a cyclohexane/water mixture, so to obtain TiO₂ NPs characterized by interparticle mesoporosity (RM-TiO₂ sample);

c) a SG method under pH control, so to obtain brookite-containing TiO₂ NPs and then to further tuned the brookite content and the NPs size by varying the calcination temperature (200 and 600 °C) (B-TiO₂-200 and -600 samples).
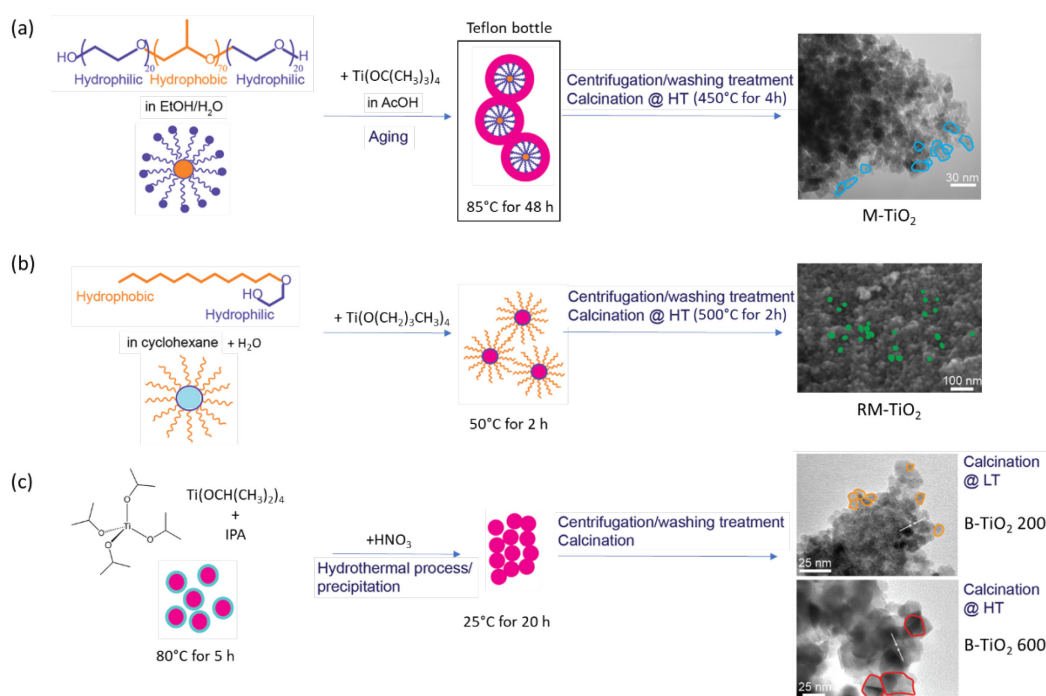
Figure 3.2-1: Schematic representation of the three adopted synthetic routes for M-TiO₂ sample (a), RM-TiO₂ sample (b) and B-TiO₂ samples (c).

3.2.1 Synthesis of undoped Titania

All the reagents for the syntheses where ACS grade chemicals from Sigma-Aldrich, whereas a commercial sample of Degussa P25 (P25) was used as reference. The TiO₂ NPs obtained by TASG method in the presence of tri-block copolymer micelles (referred from now on as M-TiO₂) were synthesised as follows: two solutions were prepared, solution A was obtained by drop-wise adding 5.0 g Ti(OC(CH₃)₃)₄ (titanium(IV) *tert*-butoxide, 97 %) to 30.0 mL acetic acid solution (20 %, v/v) and vigorously stirring for about 4 h; solution B was obtained by mixing

33

3.0 g Pluronic P123 and ca. 20.0 mL ethanol. Solution B was then dropwise added to solution A: the resulting mixture was sealed, stirred for 24 h at room temperature and transferred into a Teflon autoclave for hydrothermal treatment at 85°C for 48 h. The resulting precipitate was centrifuged, dried at 80°C and calcined in air at 450°C for 4h [33][36].

The TiO2 NPs obtained by reverse-micelle TASG method (referred from now on as RM-TiO2) were synthesised as follows [146][149]: the di-block copolymer (polyoxyethylene (20) oleyl ether (commercial name: Brij O20) dispersed in cyclohexane (the oil phase) by stirring at 50 °C. Afterwards, MilliQ water was added to the mixture and stirred for 45 min, leading to the formation of a water in oil (w/o) microemulsion of surfactant-incapsulated water nanoreactors. Ti(O(CH2)3CH3)4 (titanium(IV) butoxide, 98 %) is then dropwise added to the emulsion. The mixture is stirred for 2 h at the constant temperature of 50 °C and finally the emulsion is broken by addition of 2-propanol, followed by sonication. The solid phase is collected by centrifugation and dried at 100 °C for 24 h, followed by calcination in air at 500 °C for 2h with a temperature ramp of 2.5 °C min^{-1} to remove the surfactant.

The TiO2 NPs obtained by SG method in acid conditions to obtain high brookite content (B-TiO2) were synthesised by slightly modifying the method developed by Mutuma et al [150]. In a typical preparation, 30 ml titanium isopropoxide (Ti(OPr)4) was mixed to 30 ml isopropyl alcohol and stirred (at 500 rpm) for 20 min in a 150 mL beaker; bi-distilled water (300 mL) was added to the mixture under vigorous stirring. After mixing, the solution was heated at 80 °C in a stove for 5 h and, then, cooled down to room temperature (r.t.). The resulting liquid was dark yellow. After cooling, pH was varied by addition of 1.0 M HNO3 solution, in order to obtain a pH equal to 2.0. The sol was then left to gel at r.t. under stirring for 20 hours. The so-obtained gel was repeatedly washed with bi-distilled water, centrifuged for 12 minutes at 4000 rpm and dried in a Teflon autoclave inside a stove kept at 100 °C for 12h. Then, the sample was separated in two aliquots and treated at either 200 °C (B-TiO2-200) or 600 °C (B-TiO2-600) for 2h (heating ramp of 5 °C min^{-1}) before cooling down to r.t. (cooling ramp of 5 °C min^{-1}). Before use, both B-TiO2-200 and B-TiO2-600 were washed four times with an ethanol/water (1/3) mixture, centrifuged for 10 min at 8000 rpm and dried for 24 h at 60°C.

3.2.2 Textural, optical and surface properties of undoped Titania

The five undoped TiO2 NPs (P25, M-TiO2, RM-TiO2, B-TiO2 200 and 600 versions), were characterized by means of X-ray powder diffraction (XRD) followed by Rietveld Quantitative Phase Analysis (QPA); TEM or SEM microscopy; N2 adsorption/desorption isotherms at -196 °C; Diffuse Reflectance (DR) UV-Vis spectroscopy; ζ-potential measurements. Those techniques were adopted with the aim of assessing, respectively, the type and amount of occurring TiO2 phases; the NPs size and shape; the NPs Specific Surface Area and pore size distribution; their band gap energy (E$_g$) and the NPs surface charge.

X-Ray Powder Diffraction

Powders X-ray diffraction patterns were collected on a X'Pert Philips PW3040 diffractometer using Cu Kα radiation (2θ range from 20° to 70°; step = 0.026° 2θ; time per step = 0.82 s). Equipped slits are 0.25° divergence, 0.5° scattering, 7.5° receiving and a PIXcel 1D detector. Diffraction peaks were indexed according to the Powder Data File database (PDF 2000, International Centre of Diffraction Data, Pennsylvania). Crystallites average size (D) was determined by using the Williamson-Hall plot calculated by the *X'Pert High Score Plus 3.0e* software, while the phase content (QPA, Quantitative Phase Analysis) was evaluated by the full-profile Rietveld method applied to the diffraction patterns by using the same software.

The XRD patterns of the five TiO_2 powders are reported in figure 3.2-2 and the results of QPA and crystallite sizes are reported in table 3.2-1.
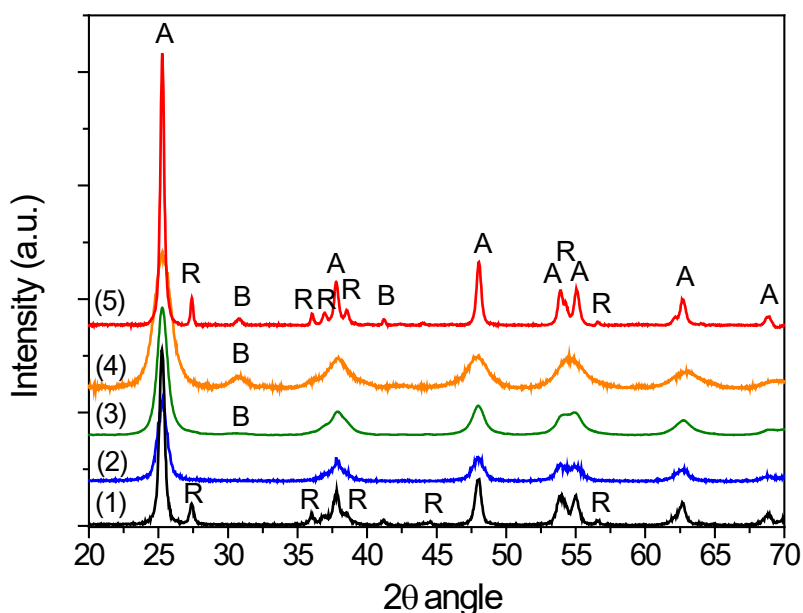
Figure 3.2-2: XRD patterns of P25 (1, black curve); M-TiO₂ (2, blue curve); RM-TiO₂ (3, green curve); B-TiO₂-200 (4, orange curve) and B-TiO₂-600 (5, red curve). Peaks ascribed to Anatase Rutile and Brookite are labelled as A, R and B, respectively.

From the acquired data, P25 (curve 1), in agreement with the literature [86][147], results as a mixture of anatase (88.8 wt.%) and rutile (11.2 wt.%). For the M-TiO_2 sample (blue curve 2), only anatase peaks are observed (at 25.5 (011), 37.4 (004), 47.9 (020), 54.0 (015), 54.9 (121), 62.6 (024), 68.9 (116) 2θ values (ICDD ref. code: 01-089-4203), and, accordingly, an anatase content of 100 wt.% was determined by QPA. From the Williamson-Hall method, the size of M-TiO_2 crystallites (Table 3.2-1) is 12.4 nm, as confirmed from TEM micrograph of the sample (Fig. 3.2-3) that shows the occurrence of NPs with elongated shape and rather homogeneous size.
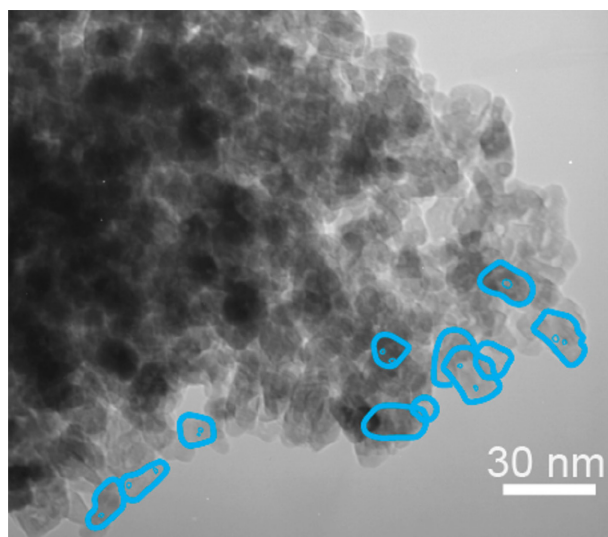
Figure 3.2-3: TEM image of M-TiO₂ sample, with some particle and inner pore contours highlighted.

The RM-TiO₂ sample (green curve 3), shows peaks of anatase (at 25.2 (011), 37.8 (004), 47.9 (020), 53.8 (015), 54.9 (121), 62.6 (024), 68.7 (116) 2θ values), and a weak and broad peak due to the (121) brookite diffraction at about 30.7 2θ. QPA analysis shows a composition of 83.0 wt% anatase, 14.9 wt.% brookite and a smaller amount of rutile (2.1 wt%). The formation of brookite in the sample is likely due to the adopted synthesis procedure, as the aqueous nano-reactors in the reverse micelle likely contain a high concentration of Ti-precursor, which may, in turn, lead to high concentrations of H^+ ions, as (small) Ti^{4+} ions have high charge/surface ratio and may lead to formation of an acid environment (where TiO₂ NPs form and grow) ultimately favouring brookite formation [27,28]. To this respect, the presence of brookite has been found to favour the transition to rutile in anatase/brookite mixed NPs obtained in acid medium [151].
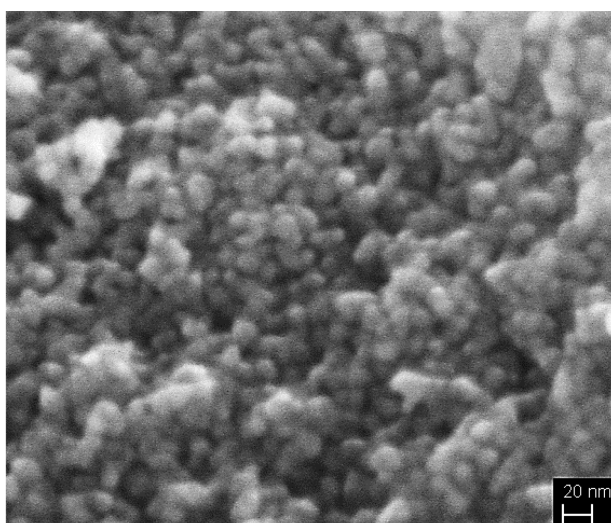
Figure 3.2-4: SEM image of the RM-TiO₂ sample.

36

As a whole, the reverse-micelle method, using a calcination temperature of 500 °C for 2h, allows the formation of almost spherical NPs with homogenous shape with a non-negligible amount of brookite, and a small fraction of rutile. The anatase crystallite size (10.5±0.4 nm) was very close to the NPs size (*ca.* 12 nm) as shown in Fig. 3.2-4. The NPs morphology (shape and size) is important as it should affect also the type of porosity occurring in the samples (as we will see later).

The B-TiO$_2$-200 sample (orange curve 4 in the XRD pattern) showed, instead, the diffraction peaks of only anatase (78.0 wt.%) and brookite (22.0 wt.%), with smaller anatase crystallite size (5.5±0.6 nm) more likely polycrystalline and NPs of inconstant shape and size (Fig. 3.2-5 left).
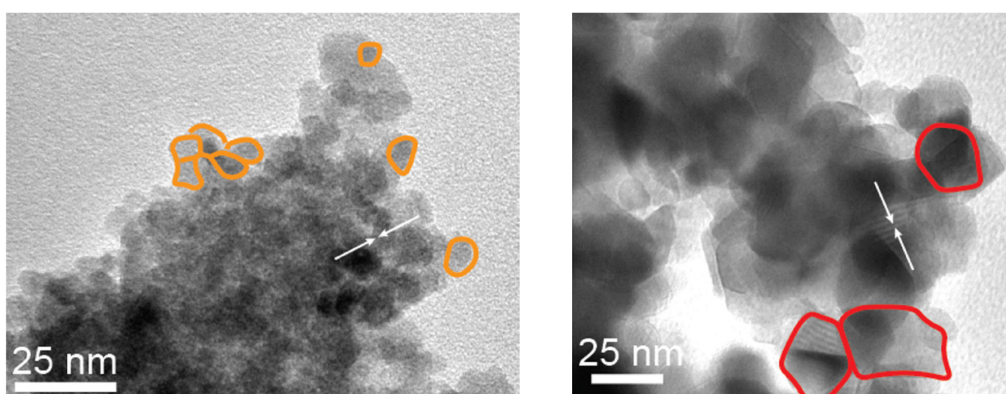
Figure 3.2-5: TEM image of B-TiO$_2$-200 (left) and B-TiO$_2$-600 (right) sample, with some particle's contours highlighted.

With the B-TiO$_2$-600 sample, the thermal treatment at higher temperature lead to a change in the phase composition and, in particular, a decrease of the amount of brookite and the appearance of rutile, in agreement with Hu et al. [151], as shown by B-TiO$_2$-600 XRD patterns and the related QPA results. Such a phenomenon should also affect the sample surface area that will be discussed later. As the morphology, TEM image (Fig. 3.2-5 right) show the occurrence, as expected from a higher temperature treatment, of larger NPs (with respect to the sample calcined at 200°C, B-TiO$_2$-200), with interference fringes, the assignment of which was, however, not straightforward as the three polymorphs have very close interplanar distances.

Table 3.2-1: Structural and textural properties of the studied samples as obtained by XRD and N$_2$ isotherms at -196°C. Band-gap energy values, as obtained by DR-UV-Vis spectroscopy. pH at the isoelectric point (pH$_{IEP}$), as obtained by ζ-potential measurement.

Sample	Synthesis method	Crystallite size (nm)[a]	QPA results (wt.%)[b]	SSA (m^2 g^{-1})[c] / Total Pore Volume (cm^3 g^{-1})	Band-gap energy (Eg, eV)[d,e,f]	pH$_{IEP}$
P25	flame hydrolysis of TiCl$_4$[g]	19 ± 3 (A) 23 ± 4 (R)	88.8 (A) 11.2 (R)	74	3.30[d]	6.2-6.9[g]
					3.28[e]	
				0.10	3.51[f]	
M-TiO$_2$	TASG with tri-block copolymer followed	12.4 ± 1.3 (A)	100 (A)	150	3.25[d]	2.37
					3.23[e]	

		crystallite size (a)	phase comp. (b)	SSA / pore vol. (c)	band gap (d,e,f)	(g)
	by calcination at 450 °C			0.28	3.35 [f]	
RM-TiO₂	TASG with di-block copolymer followed by calcination at 500 °C	10.5 ± 0.4 (A) 5.4 ± 0.1 (B) 7.8 ± 0.2 (R)	83.0 (A) 14.9 (B) 2.1 (R)	70 / 0.09	3.17 [d] 3.15 [e] 3.29 [f]	3.56
B-TiO₂-200	Template-free SG followed by calcination at 200°C	5.5 ± 0.6 (A) 3.8 ± 0.4 (B)	78.0 (A) 22.0 (B)	210 / 0.31	3.37 [d] 3.38 [e] 3.57 [f]	2.77
B-TiO₂-600	Template-free SG followed by calcination at 600°C	39.0 ± 5.5 (A) 16.8 ± 3.6 (B) 52.1 ± 8.1 (R)	81.6 (A) 9.3 (B) 9.1 (R)	31 / 0.09	3.22 [d] 3.22 [e] 3.36 [f]	2.36

[a] As obtained by applying the Williamson-Hall method
[b] As obtained by Rietveld refinement
[c] As obtained by applying the BET method
[d] As obtained by linear extrapolation of the absorption edge
[e] As obtained by applying the Tauc plot method for indirect band-gap semiconductor $(F(R)*h\nu)^{1/2}$
[f] As obtained by applying the Tauc plot method for direct band-gap semiconductor $(F(R)*h\nu)^{2}$
[g] As reported in the literature for P25 NPs with average size in the 20-40 nm range and from [147]

N₂ adsorption/desorption isotherms

N₂ adsorption/desorption isotherms, reported in figure 3.2-6, were measured at liquid nitrogen temperature (-196 °C) by means of a Micromeritics ASAP 2020Plus instrument on powders outgassed at 150 °C for 4h to remove water and other atmospheric contaminants from material surface. The powder Specific Surface Area (SSA) was determined according to the Brunauer-Emmett-Teller (BET) method; pore total volume was measured at $p/p^0 = 0.99$ and the Pore Size Distribution (PSD) was calculated by applying the BJH (Barrett-Joyner-Halenda) method to the isotherm desorption branch.
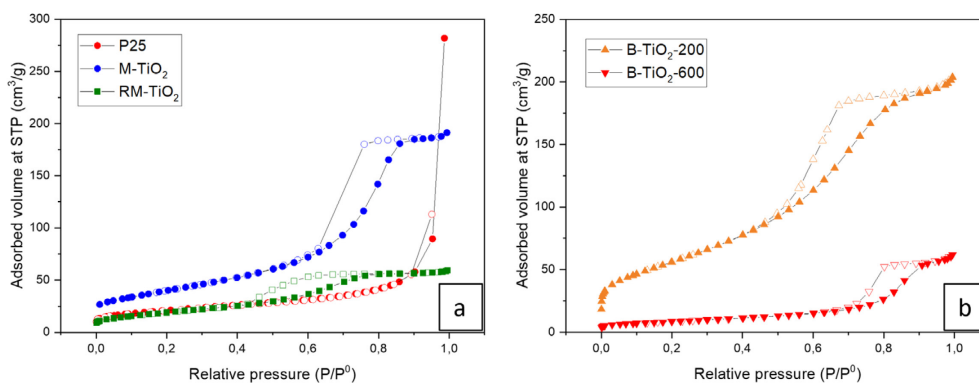
Figure 3.2-6: N₂ adsorption/desorption measured at -196°C of P25 (red circles), M-TiO₂ (blue circles) and RM-TiO₂ (green squares) in section (a); B-TiO₂-200 (orange triangles) and B-TiO₂-600 (red triangles) in section (b). Full marks: adsorption branch; empty marks: desorption branch.
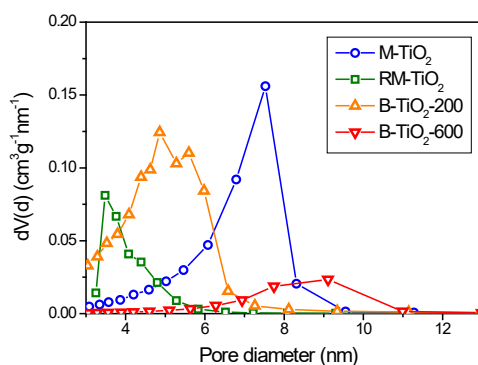
Figure 3.2-7: PSD as obtained by applying the BJH method to isotherms desorption branch with the samples: M-TiO₂ (blue circles), RM-TiO₂ (green squares); B-TiO₂-200 (orange triangles); B-TiO₂-600 (red triangles).

P25 shows a type II isotherm as expected from literature [152][153], with N_2 condensation occurring at high relative pressure (i.e., $P/P^0 > 0.85$) due to the presence some large (inter-particle) meso-macroporosity. The M-TiO₂ sample showed instead a type IV isotherm likely due to the occurrence of both intra- and inter-particles mesopores, with the corresponding value of the SSA (Table 3.2-1) being more than twice that of P25. The observed H2(b) type hysteresis loop is typical of *"ink-bottle"* inter-particle mesopores associated with pore blocking [154][155] (Fig. 3.2-8 e), with size distribution of neck widths very broad, as confirmed by the corresponding PSD which show heterogeneous mesopores dimensions: the most abundant family have a diameter of around 7.5 nm, whereas smaller mesopores are likely intra-particle mesopores.
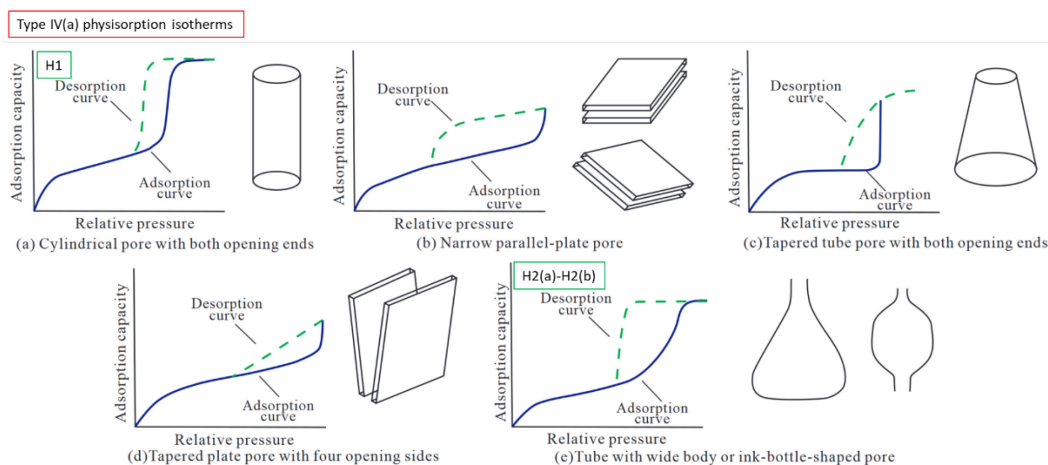
Figure 3.2-8: Schematic representation of some typical Type IV(a) physisorption isotherms and corresponding pores geometry. Adapted from [154]

M-TiO$_2$ sample, on the other hand, has undergone calcination at 450 °C for 4h to allows the removal of the organic template, but causing the crystallization/synterization of the material and some structure collapse, with consequent loss of SSA and interparticle mesopores stemming from the template removal and consequent pore shrinkage occurring during calcination. M-TiO$_2$ sample also shows some smaller intra-particle mesopores as also visible from the TEM image (Fig. 3.2-4), probably due to the adopted synthesis/micelles removal.

RM-TiO$_2$ sample showed a type IV isotherm with H2 type hysteresis loop, ascribed to capillary condensation within inter-particle mesoporosity, but a lower SSA area (71 m^2 g^{-1}). The corresponding PSD shows a maximum at 3.5 nm and a tail towards larger diameter mesopores.

B-TiO$_2$-200 sample is the one showing the highest SSA, likely due to the very low temperature adopted during the thermal treatment. The N$_2$ isotherms of both B-TiO$_2$-200 and B-TiO$_2$-600 samples are compared in Fig. 3.2-6 b: type IV isotherms with H2 hysteresis loops are observed, but lower total adsorbed volume and SSA were measured with the high temperature threated one, which also showed highly crystalline NPs, as confirmed by the sharpness of XRD peaks (red curve n°5, Fig. 3.2-2).

By considering only the Pore Size Distributions (PSD) (Fig. 3.2-7), all samples showed occurrence of mesopores. The smallest mesopores diameters are obtained with RM-TiO$_2$ sample. The M-TiO$_2$ sample showed an asymmetric PSD curve, with maximum at 7.5 nm and a large pore volume. By increasing the calcination temperature, two effects are observed on pore volume and size of B-TiO$_2$-200 and B-TiO$_2$-600, respectively: the pore volume dramatically decreases and only few larger mesopores are observed. Such phenomena are in agreement with the largest particle size observed by TEM analysis.

Diffuse Reflectance UV-Vis spectroscopy

Diffuse Reflectance (DR) UV-Vis spectra of powder samples were measured on a Cary 5000 UV-Vis-NIR spectrophotometer (Varian instruments) equipped

with a DR apparatus (integration sphere). The obtained DR spectra are reported as Kubelka–Munk function described in *Eq.* (3.2.1) where R is the absolute reflectance of the layer, *s* is the scattering coefficient and *k* is the molar absorption coefficient with the assumption of "infinite" thick layer.

$$F(R) = \frac{1 - R^2}{2R} = \frac{k}{s} \qquad (3.2 - 1)$$

DR-UV-Vis spectra of all the samples are reported in Fig. 3.2-9. All the studied powders, except B-TiO$_2$-200 sample, absorb in a slightly broader range of wavelengths with respect to P25, with the onset of absorptions at 382 nm (M-TiO$_2$), 390 nm (RM-TiO$_2$), 368 nm (B-TiO$_2$-200), 385 nm (B-TiO$_2$-600) and 375 nm for P25. Energy gap calculation are reported in Table 3.2-1 with the corresponding values of E$_g$ as calculated according to three different methods as we are dealing with mixed phases which can be considered either indirect band or direct band gap materials. As expected, the E$_g$ values calculated by linear extrapolation of the onset of absorption and by the Tauc's plot method for indirect transitions (F(R)*hν)$^{1/2}$) are very close, whereas higher values were obtained by using the equation for direct transition (F(R)*hν)^2) [156]. Though we are making an approximation, is possible to use the values obtained by the first two methods to evaluate a possible trend in the set of samples studied here. With B-TiO$_2$-200, the small NPs sizes (~5 nm), that implies higher quantum confinement, and the presence of only brookite, along with anatase, brings about an increase of the E$_g$ value with respect to both the M-TiO$_2$ sample (pure anatase) and to the other samples, containing a certain amount in rutile, in agreement with literature, which reports usually higher E$_g$ values for brookite (3.1-3.4 eV), with respect to anatase (3.19-3.23 eV) and rutile (3.0-3.031 eV) (Table 2.1-1 for references).
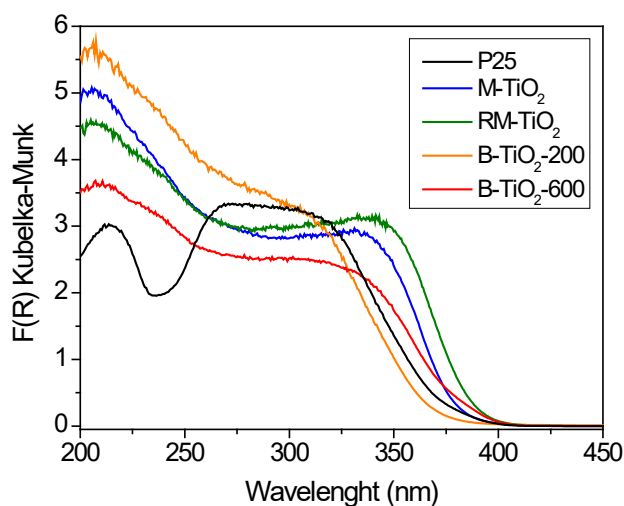
Figure 3.2-9: DR-UV-Vis spectra in the range 200-450 nm of P25 (1, black curve); M-TiO$_2$ (2, blue curve); RM-TiO$_2$ (3, green curve); B-TiO$_2$-200 (4, orange curve) and B-TiO$_2$-600 sample (5, red curve).

Zeta potential

The surface of TiO$_2$ nanoparticles dispersed in water is covered by hydroxyl groups, and, as reported by Biswas et al [157], extra hydrogen ions are produced

and the solution pH decreases with the increase in the solution of mass concentrations / particle surface area as shown in Eq. 3.2-2. These hydroxyls, however, can confer an amphoteric behaviour to the surface, where Ti-OH can react either in basic way (Eq. 3.2-3) at low pHs or in acid way (3.2-4) at high pHs, or, with another point of view, when solution pH is less than pH$_{IEP}$, Eq. 3.2-2 results in creation of the positive surface charge (OH$_2^+$) and positive zeta potential. When pH is larger than pH$_{IEP}$, Eq. 3.2-4 results in creation of the negative surface charge (O$^-$) and negative zeta potential [158][159].

$$Ti^{IV} + H_2O \quad \rightarrow \quad Ti^{IV}\text{-OH} + H^+ \quad (3.2\text{-}2)$$
$$Ti^{IV}\text{-OH} + H^+ \rightarrow \quad Ti^{IV}\text{-OH}_2^+ \quad (3.2\text{-}3)$$
$$Ti^{IV}\text{-OH} \quad \rightarrow \quad Ti^{IV}\text{-O}^- + H^+ \quad (3.2\text{-}4)$$
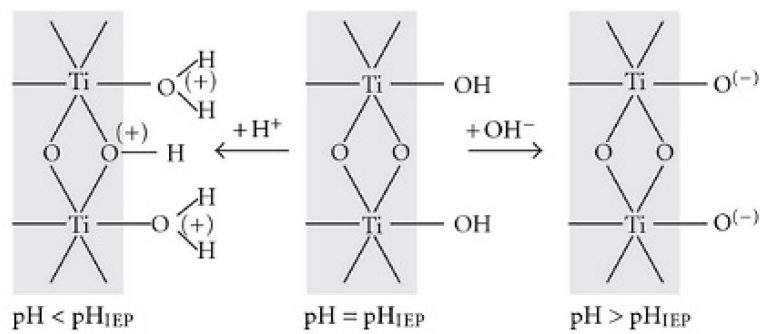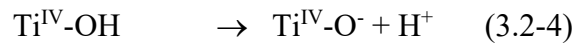
Figure 3.2-10: Schematic representation of titania surface-water interaction

The value of pH that discern this behaviour (pH$_{IEP}$), and consequently the surface associated properties, can be evaluated by means of zeta potential measurements. In general, the pH at which the surface of a solid is neutral is the *isoelectric point* (IEP) which corresponds with the *point of zero charge* (PZC) if no adsorption of the ions in the solution takes place on the particle surface.
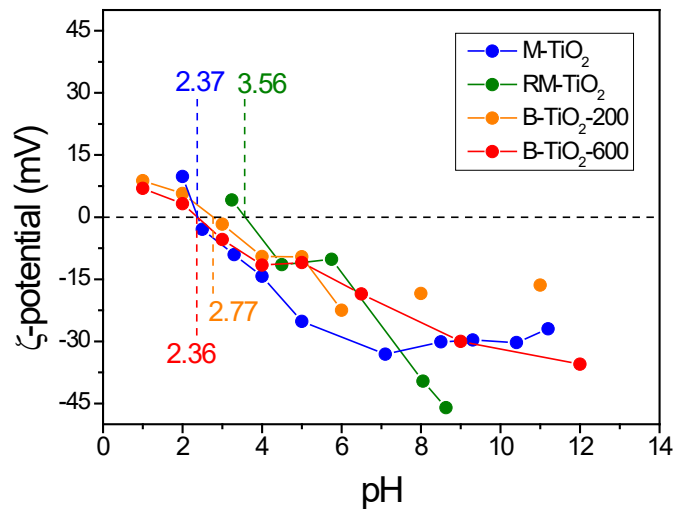
Figure 3.2-11: ζ-potential measurement on the studied samples.

The ζ-potential curves (reported in figure 3.2-10) of the TiO$_2$ NPs were obtained by measuring the electrophoretic mobility as a function of pH by means of electrophoretic light scattering (ELS) (Zetasizer Nano-ZS, Malvern Instruments, Worcestershire, UK). Each sample powder was suspended in ultrapure water (MilliQ) and either sonicated for 2 min (10 W/ml, 20 kHz, Sonoplus, Bandelin, Berlin, Germany) or magnetically stirred for 5 min. The ζ-potential was measured at room temperature after adjusting the pH step by step by addition of either 0.1 M NaOH or 0.1 M HCl.

The isoelectric point (pH$_{IEP}$) for all samples results below the values reported for P25 NPs of 6.2-6.9 pH$_{IEP}$ (Table 3.2-1) with average particle size in the 20-40 nm range [147] and of pure anatase NPs ($\sim$6.2pH$_{IEP}$) with average size in the 7.0-20 nm range [157]. According to ref. [157], the primary particle size and the surface area are the main factors affecting the charge of TiO$_2$ NPs obtained by sol-gel methods, whereas the type of crystalline phase do not affect the NPs surface charge as they tested 100% to 36% anatase composition with fixed nanoparticles dimension (36nm) reporting a variation of only $\sim$0.2 pH$_{IEP}$.

As nanoparticle size decreases, it is known that the percentage of surface atom/molecule increases significantly. Moreover, surface electronic structure, surface defect density, and surface sorption sites also are strongly modified [160]. Additionally it has been observed that modification of the nanoparticle surface coordination environment and the crystallographic orientation of exposed surface lead to changes in the surface acidity constants/pH$_{IEP}$ [161][162]. Consequently, nanoparticle pH$_{IEP}$ become function of particle size.

Nonetheless, Holmberg et al. [163] predicted that TiO$_2$ NPs with a diameter below 10 nm have a higher surface charge with respect to larger NPs, and so the pH$_{IEP}$ should increase with smaller NPs. In facts this trend is followed by the B-TiO$_2$-600 (40nm) in comparison to the B-TiO$_2$-200 (5nm) and for the RM-TiO$_2$ that showed a higher pH$_{IEP}$, the former higher of other studied samples probably due to the type of adopted synthesis, which allows to obtain NPs with controlled size by nucleation and growth within the reverse micelles.

For pure TiO$_2$ NPs (with diameter in the range of 14 - 33 nm) a PZC of 6.8 [164] was reported; Allard et al found a PZC of 6.1 with commercial anatase NPs (with a diamater of ca. 20 nm) [165]; Al-Hetlani et al found a PZC of 5.98 for smaller anatase NPs (around 7.2 nm [166]); Huijun et al reported a PZC of 6.2 for anatase NPs (5-10 nm) [167]. The much lower value of PZC measured here may be ascribed, rather than to the size of NPs, to the type of synthesis [168,169] that probably favors the formation of a very acidic surface, in agreement with previous work [157].

3.3 Manganese doped Titania

3.3.1 Synthesis of Manganese doped Titania

Mn doped TiO_2 and pure TiO_2 nanoparticles were prepared by reverse micelle microemulsion sol–gel method [146][149][170] in a process similar to that of undoped sample RM-TiO_2 of the previous chapter, using Brij O20 as surfactant and cyclohexane as apolar phase, titanium(IV) butoxide 97% (Ti-(O-$(CH_2)_3CH_4)_4$ or for short Ti-$(BuO)_4$) and Manganese(II) nitrate tetrahydrate ($Mn(NO_3)_2 \cdot 4H_2O$, Sigma-Aldrich, *purum* p.a. $> = 97\%$) as precursors of the two respective metals. All chemicals provided by Aldrich.

Different precursors amounts were used in order to obtain contents of 0, 1, 5 and 10 %wt Mn/(Mn+TiO_2) with corresponding samples name of TiO_2, Mn_1, Mn_5, Mn_10 respectively. The synthesis procedure consisted in the following steps: Brij-O20 was dispersed in cyclohexane by stirring at 50 °C. Meanwhile the salt precursor of Manganese was dissolved in MilliQ water at the same temperature. The homogeneous solution was added afterwards to the oil/surfactant solution and stirred for 45', which resulted in the formation of water in oil (w/o) emulsion of surfactant nanoreactors containing the metal salt. Ti-$(BuO)_4$ was then added to the emulsion. At this point, the deionized water hydrolyses the Ti-$(BuO)_4$ alkoxide end groups forming titanium hydroxide groups. Afterwards, hydroxide groups undergo polycondensation reaction and finally form titanium oxide (Ti–O–Ti) bonds [171] and mixed Ti–O–Mn bonds. The mixture was stirred for 2h always maintained at 50 °C and finally the emulsion was broken by addition of 2-propanol, followed by sonication. The solid phase was then collected by centrifugation and dried at 100 °C for 24h, followed by calcination in air at 500 °C for 2h with a temperature ramp of 2.5 °C/minute to remove the surfactant. For comparison, sample was prepared by Incipient Wetness Impregnation (IWI) method by using manganese(II) nitrate tetrahydrate $Mn(NO_3)_2*4H_2O$: the TiO_2 support was impregnated by dropwise addition of the concentrated salt aqueous solution under stirring at 80 °C. The resulting powder was then calcined in the same condition as previous samples and will be referred to as Mn_10IMP.

3.3.2 Textural, optical and surface properties of Manganese doped Titania

As for the undoped Titania samples, the Manganese doped ones have been characterised to understand the physico-chemical propertied and differences in comparison to the undoped and reference TiO_2 materials by maintaining the same synthetic conditions of RM-TiO_2 to avoid new variables to get involved in the material modification. This synthetic method will be used also used for Molybdenum doped samples (chapter 3.4) due to a trade-off of obtained surface areas, phases contents and time requirements for the synthesis. Same characterization parameters have been used, if not otherwise specified.

X-Ray Powder Diffraction

Manganese doped samples X-ray diffraction patterns were collected in the 20 - 90 2θ° range, by using scan step = 0.02 2θ, a time per step = 2 s to improve signal to noise ratio and resolution compared to undoped titania samples as we are introducing Manganese that may produce overlapped peaks and increase pattern complexity.

The XRD patterns of the five samples: undoped TiO_2 (same as previous RM-TiO_2), Mn_1, Mn_5, Mn_10, Mn_10IMP are reported in figure 3.3-1 and the results of QPA and crystallite sizes are reported in table 3.3-1.
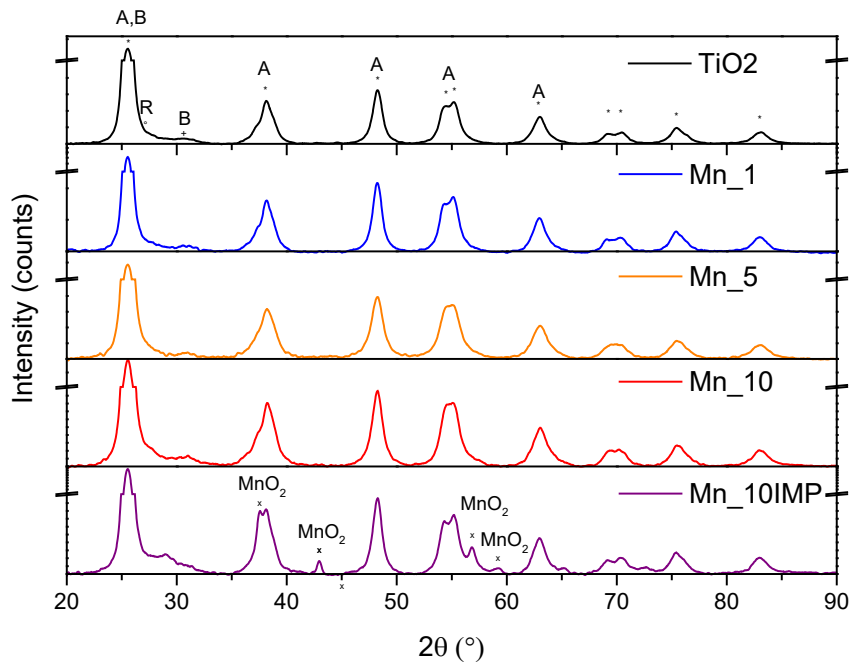
Figure 3.3-1: XRD patterns of TiO₂ and Manganese doped TiO₂. Peaks ascribed to Anatase Rutile and Brookite are labelled as A, R and B, respectively.

In the powder diffraction spectra the reflection peaks of anatase (Ref. code ICSD 01-073-1764) are seen at 2θ around 25.3 (101) for the main peak, three overlapping lines at 37.1(103), 37.9 (004) and 38.6 (112). One strong diffraction at 47.96 (200), two lines at 54.0 (105) and 55.0 (211), two overlapping at 62.0 (213) and 62.7 (204), two at 68.9 (116) and 70.2 (220), three close lines at 74.2 (107), 75.1 (215) and 75.9 (301), and lastly a double peak at 82.7 (224) and 83.1 (312).

The secondary phase patterns of brookite (ICSD 01-076-1934) diffracts two small peeks under the anatase one (not detected without curve fitting) and a secondary non overlapped peek at around 30.6° (211), which is visible in all the acquired powder XRD. Lastly, a barely visible rutile phase can be detected with main peek at 27 2θ° (110).

Table 3.3-1: Crystallite sizes and QPA of undoped and doped samples with goodness of fitting (GOF) and standard deviations.

Crystallite sizes (Williamson-Hall) (nm)

45

	GOF	Anatase	st dev	Brookite	st dev	Rutile	st dev	MnO_2
TiO₂	2,11	10,2	0,3	6,5	0,1	7,3	0,1	-
Mn_1	2,51	9	0,3	4,6	0,1	4,6	0,1	-
Mn_5	2,06	6,4	0,2	3,5	0,1	3,3	0,4	-
Mn_10	1,83	8,3	0,2	5,1	0,1	4,3	0,2	-
Mn_10 IMP	2,51	8,7	0,2	5,6	0,1	8,1	0,4	9,7

Phases content (Rietveld) (%)

	Anatase	Brookite	Rutile	MnO_2
TiO2	81,3	16,2	2,5	-
Mn_1	81,1	13,6	5,3	-
Mn_5	74,6	18,5	6,9	-
Mn_10	76,3	16,7	7,0	-
Mn_10 IMP	69,2	18,1	4,0	8,7

For the impregnated sample Mn_10_IMP, the diffraction peaks of MnO_2 (Ref. code 03-065-2821) are seen with main peeks at 28.8 (110), 37.5 (101), 43.0 (111), 56.9 (211), 59.2 (220), 64.9 (002), 72.6 (002). It is important to notice that only the impregnated sample in the XRD spectra gives sharp peaks for the metal oxide (MnO_2) despite the relatively high metal concentrations of 10% weight also present in the one pot counterpart sample (Mn_10). This feature can be indicative of high dispersion, low crystalline/amorphous structure (crystallites of Mn oxides are too small to be detected) and/or the metal is incorporated in the TiO_2 lattice as substitutional atoms, as the Pauling's rule [172] states that an octahedral coordination is possible if the ratio between cation and anion radius, in our case $r^{M^{n+}}/r^{O^{2-}}$, is in the range between 0.732 and 0.414, where $r^{O^{2-}} = 1.40$ Å is the oxygen anion Pauling radius and $r^{M^{n+}}$ is the metal cation Pauling radius, which is $r^{Ti^{4+}} = 0.68$ Å. Since Mn have oxidation states of Mn^{2+} (0.80 Å), Mn^{3+} (0.66 Å) or Mn^{4+} (0.60 Å), octahedral coordination after the isomorphic incorporation of Mn into the titania framework can be obtained for all these oxidation states [173] provided that charge neutrality is maintained in the solid.
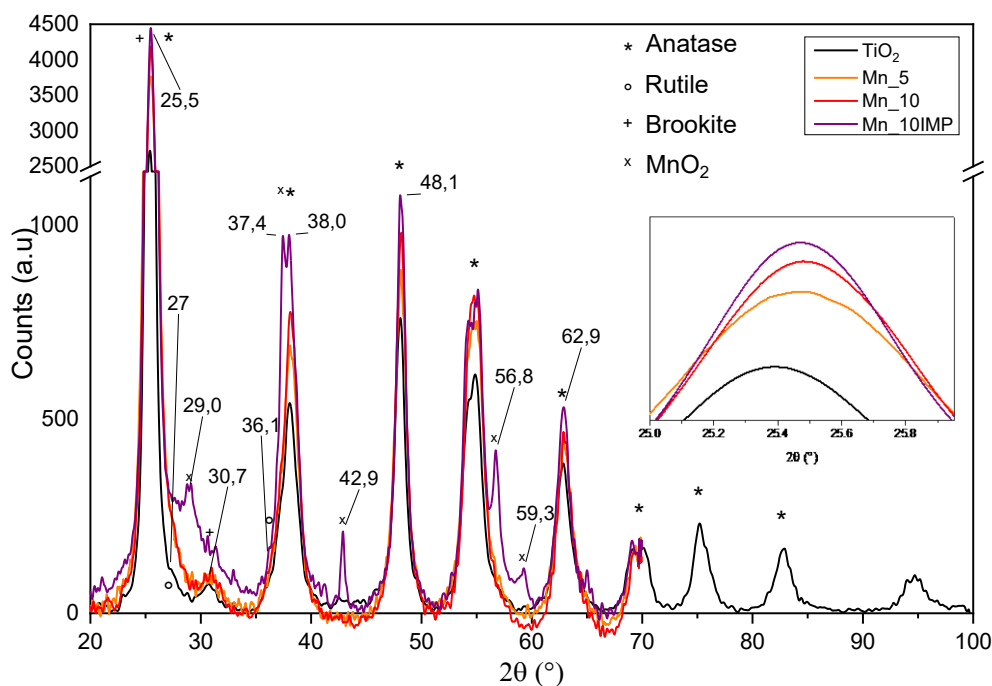
Figure 3.3-2: Details and overlapping XRD patterns of TiO₂, 5, 10 and 10% Mn impregnated samples. In the inset the magnification of the main anatase diffraction peak (101).

Scattering intensities, as highlighted in Fig. 3.3-2, increase with doping level, as expected since manganese have higher scattering factor than titanium for Cu Kα energy. In Fig. 3.3-2 inset the (101) peek is shifting to higher diffraction angles for doped samples, as the titania lattice is perturbed by the Mn substitution. Isostructural substitution can be confirmed by the lattice size almost linearly changing with the dopant percentage (Vegard rule). As expected, the impregnated sample (101) peek position is at lower angles as compared to the one-pot synthesised Mn_10 sample, as most of manganese remains at the surface, while the impregnated sample peak position is somewhat the same of the 5% one pot sample. We could dare to say that TiO₂ lattice can accommodate only up to the 5% composition of Mn atoms.

No other phases can be detected with our instrumentation, but it is known that Mn₂O₃ is more amorphous than MnO₂ [174], so more difficult to detect by XRD.

X-ray Photoelectron Spectroscopy

Manganese have six stable oxidation states (0, II, III, IV, VI and VIII), three of them with significant multiplet splitting (II, III, IV), one with less defined splitting or broadening (VI). Due to these multiplet splitting structures, a serious challenge arises for both qualitative and quantitative analysis by XPS. In table 3.3-2 the binding energies for reference Mn oxides of Mn2$p_{3/2}$ peaks are reported [175] [176][177][178].

Chemical state		Binding energy Mn2p$_{3/2}$ (eV)
Mn metal	Mn^0	638.6
MnO	Mn^{2+}	640.4-641.7
Mn$_3$O$_4$	Mn$^{2+/3+}$	641.3-641.7
Mn$_2$O$_3$	Mn^{3+}	641.7-641.9
MnO$_2$	Mn^{4+}	641.9-642.6

The surface atomic concentrations for manganese, oxygen and titanium with the atomic ratios Mn/Ti are listed in Table 3.3-3 based upon the binding energies of O1s, Mn2p, and Ti2$p_{3/2}$ in the bare and doped titania oxide material. All the values are referenced to the Ti2$p_{3/2}$ BE value of 458.3 eV due to its intensity, lack of interferences and absence of other oxidation states.
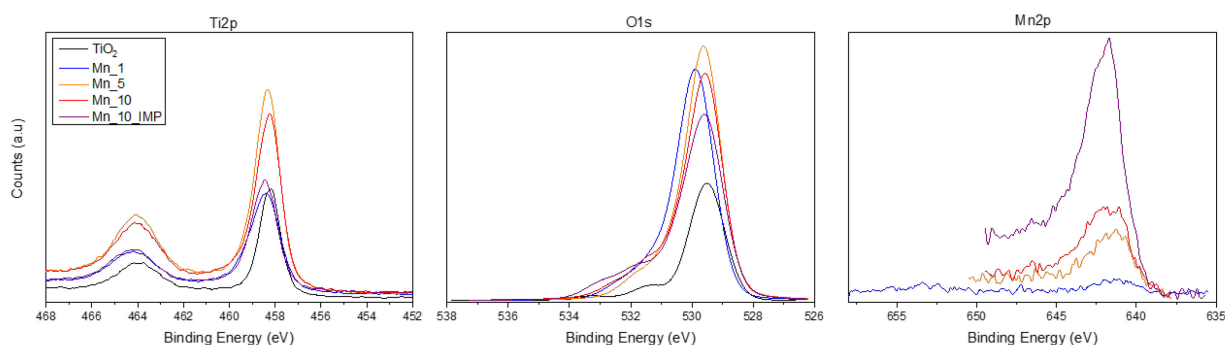
Figure 3.3-3: High resolution XPS spectra of Ti2p, O1s and Mn2p regions for undoped and Mn-doped titania samples.

The doublet of Ti2$p_{3/2}$ and Ti2$p_{1/2}$ (464.0 eV) arises from spin orbit-splitting. These peaks are consistent with Ti^{4+} in TiO$_2$ lattice [179]. The XP O1s spectrum from all the samples was curve fitted and the results are reported in Fig. 3.3-4. There are three (for TiO$_2$, Mn_1 and Mn_5) to four peak components (Mn_10 and Mn_10_IMP): the lower binding energy peak is due to lattice oxygen bonded to Ti and/or Mn (529.7±0.2 eV), whereas the higher BE one (around 531.4±0.3 eV, green curve) is attributed to non-lattice oxygen/OH due to adsorption of OH$^-$ at the surface. Lastly, the blue curve component at 530.5±0.1 eV is due to the oxygen in oxygen-deficient regions, whereas the higher binding energy peak (magenta curve) at 533.2±0.2 eV is ascribed adsorbed/structural water which increases in Mn_10 and Mn_10_IMP samples [180][181]. It is important to notice how oxygen vacancies increase with doping concentration, as can be derived by the relative abundance peak component at 530.5±0.1 eV: it is around 10-11% in Mn_5 and increases up to 16% in Mn_10 and Mn_10_IMP.
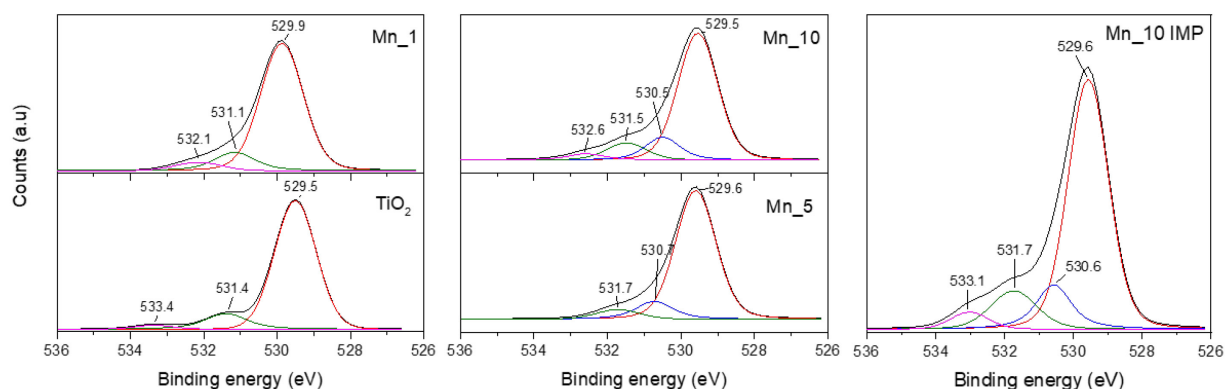
Figure 3.3-4: O1s deconvoluted peaks for TiO₂, Mn_1/5/10 and Mn_10_IMP samples.

The curve fitting procedure applied to Mn2$p_{3/2}$ XP spectra of Mn_5 to Mn_10_IMP samples shows (Fig. 3.3-5) five peak components that can be attributed to Mn^{2+} (640.0±0.3 eV, red curve), Mn^{3+} (641.36±0.3 eV, blue curve) [182], Mn^{4+}
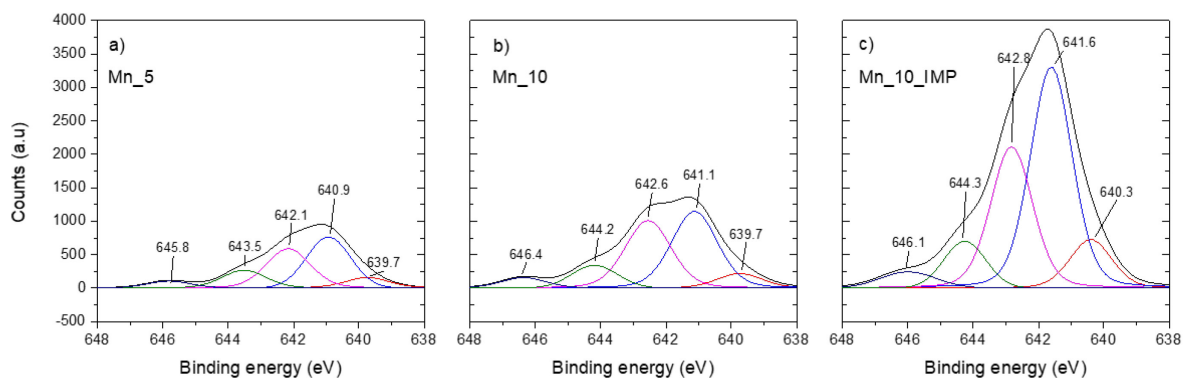
Figure 3.3-5: Deconvoluted spectra of Mn2p₃/₂ region of a) Mn_5, b) Mn_10 and c) Mn_10_IMP samples

(642.5±0.3 eV, magenta curve), partially undecomposed Mn-nitrate (644.2±0.1 eV, green curve) [183][184] and a satellite peak (shake-up) located at 646.0±0.2 eV (dark blue curve) due to Mn^{2+} ions. Mn2$p_{3/2}$ XP spectrum of Mn_1 was not curve fitted due to the very low signal-to-noise ratio.

Table 3.3-3: Atomic surface concentrations and ratios as determined by XPS.

Mn content (wt %, *at%*)	XPS surface atomic concentrations (%)ᵃ							
	(Mn ox. states relative abundance)							
	Manganese	Mn²⁺	Mn³⁺	Mn⁴⁺	Mn nitrate	Titanium	Oxygen	Mn/Ti
1 (*0.49*)	1.1 ±0.2					26.5 ±1.6	72.4 ±1.6	0.042±0.004
5 (*2.49*)	2.6 ±0.3	10	40	34	16	26.3 ±1.1	71.1 ±1.4	0.10±0.01
10 (*5.11*)	3.5 ±0.5	8	43	37	12	24 ±2	73 ±2	0.15±0.02
10* (*5.11*)	10.5 ±0.5	11	49	30	10	17.5 ±1.0	72.3 ±1.3	0.58±0.04

Raman spectroscopy and Energy Dispersive X-ray Spectroscopy

Raman spectra, in the region of 80–1000 cm^{-1}, shown in Fig. 3.3-6, were acquired on a Renishaw InVia Reflex micro-Raman spectrometer (Renishaw plc, Wotton-under-Edge, UK) equipped with a cooled CCD camera. The Raman source was a diode laser (λ_{ex}=514.5 nm), and the inspection occurred over pelletized samples to ensure a "flat" surface, through a microscope objective (10X), in backscattering light collection. The following conditions were employed to collect each spectrum: 5mW laser power for all sample except for TiO$_2$ that was exited with 0.1mW due to detector saturation, 5 s of exposure time and 4 accumulations. Data for undoped TiO$_2$ was afterward normalised by a factor of 50.

Anatase TiO$_2$ shows strong Raman peaks at 143 (E$_g$), 399 (B$_{1g}$), 516 (A$_{1g}$+B$_{1g}$) and 638 cm^{-1} (E$_g$) [96]. Some small brookite peeks are also visible around 121 (A1g), 132 (B3g), 170 (B1g), 197 (A1g), 246 (A1g) and 330 cm^{-1} (mostly B modes) [98] confirming the XRD results. Also the strongest Rutile peek is visible in the undoped TiO$_2$ (M-TiO$_2$) at around 445 cm^{-1} and 450 cm^{-1} for P25 [91]. Spectra of Mn_10_IMP confirm the presence of nitrate precursor as the 1050 cm^{-1} band can be ascribed to ν_1 NO$_3$ vibration [185].
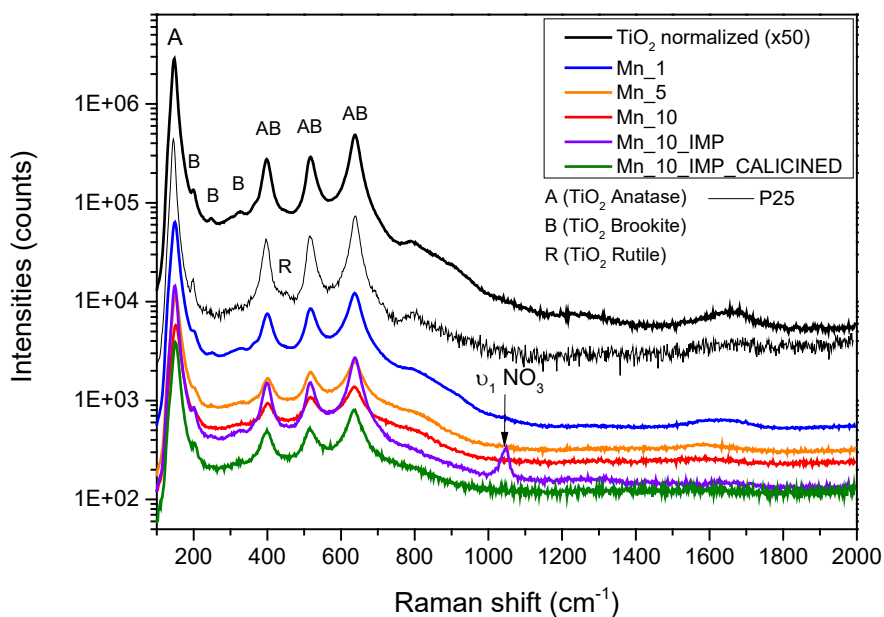
Figure 3.3-6: Raman spectra (log scale) of TiO$_2$ and Mn doped TiO$_2$ samples under 532nm laser excitation. P25 spectra have arbitrary intensities.
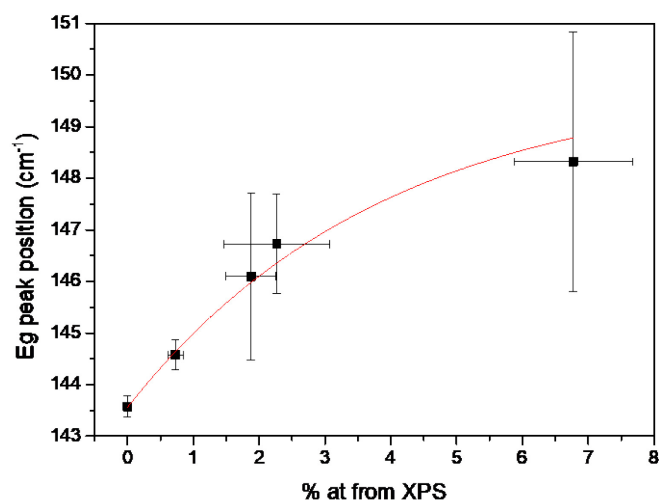
Figure 3.3-7: Eg position for TiO$_2$ and Mn-doped TiO$_2$ samples vs atomic concentrations obtained by XPS.

In Fig. 3.3-7, the Eg Raman scattering peak shifting to higher wavenumbers can be better appreciated as doping concentration increases. The shift can be ascribed to the distortion of Ti–O band by Mn incorporation. Raman spectra were acquired multiple times on different spots and Eg positions errors were estimated. From the Eg vs XPS atomic surface concentration plot an idea of heterogeneity of the material, that reaches higher value of uncertainty, can be highlighted. High doped samples, especially the impregnated one have the highest surface heterogeneity, both in Mn concentration and Raman Eg peak position as confirmed by EDX maps analysis reported in Fig. 3.3-8.
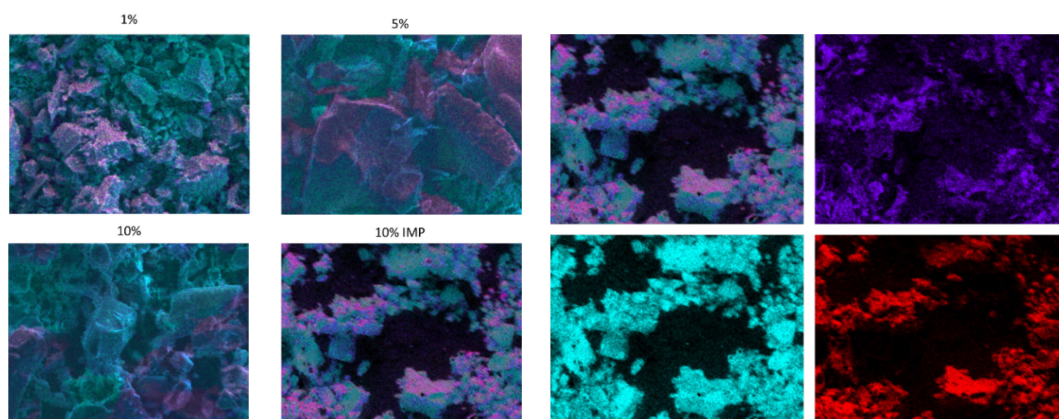
Figure 3.3-8: EDX survey elemental mapping of doped TiO$_2$ samples (left) and Mn (violet), Ti (light blue) and O (red) K$_{\alpha1}$ signals for the 10 %w impregnated sample (right).

Moreover, by comparing the atomic ratio of dopant determined by the surface technique XPS and the bulk one EDX it is clear that manganese is prone to localize on surface as Mn/Ti ratio seen by XPS is higher than bulk values. Only for the 10% and 10% impregnated sample the ratio is lower than the nominal one, probably due to aggregation/loss of manganese.
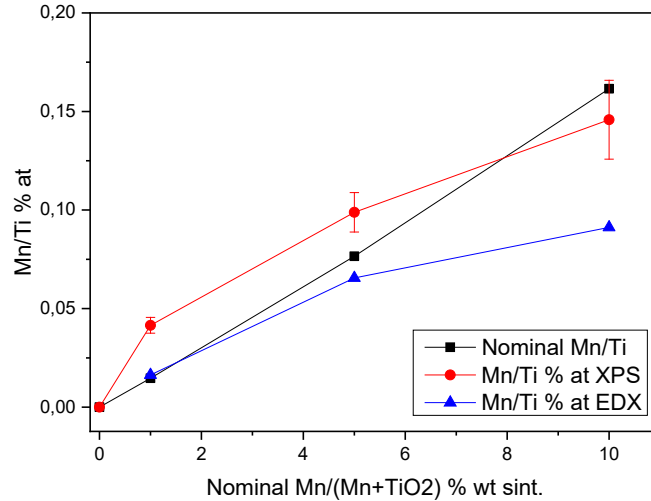
N$_2$ adsorption/desorption isotherms

N$_2$ sorption/desorption isotherms in the case of Mn-doped samples were acquired on a Micromeritics Tristar II instrument. Samples were outgassed at 200 °C for 2h prior the measurements at around liquid nitrogen temperature of −196 °C. Nitrogen gases with super high purity (99.999%) was used for the physisorption measurements. Samples specific surface area (SSA) was calculated according to the Brunauer–Emmett–Teller (BET) method; pore total volume was measured at $p/p^0 = 0.99$; pore size distribution (PSD) was calculated by applying the BJH (Barrett-Joiner-Hallenda) method to isotherm desorption branch.
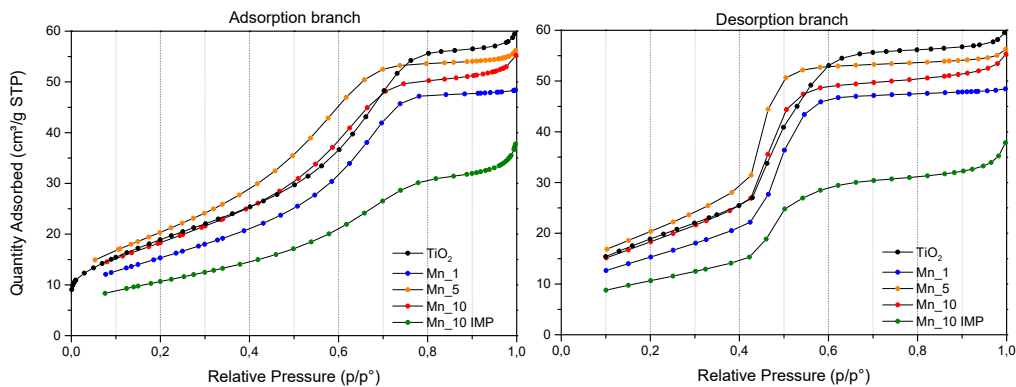
Data shows pronounced H2(b) type loop for Manganese doped samples that can be associated with pore blocking with a larger size distribution of the necks widths. The impregnated Mn_10_IMP sample has the lowest area and cumulative pore volume (pore volume peak area in figure 3.3-11) as expected by impregnation method which consist in the coverage of the external surface area and may occlude some pores in the process. It is interesting to notice the mirror feature of BET area

and pore diameter (peak position) as at smaller pores corresponds higher surface area (many small pores) and at larger pores a low surface area (few large pores).
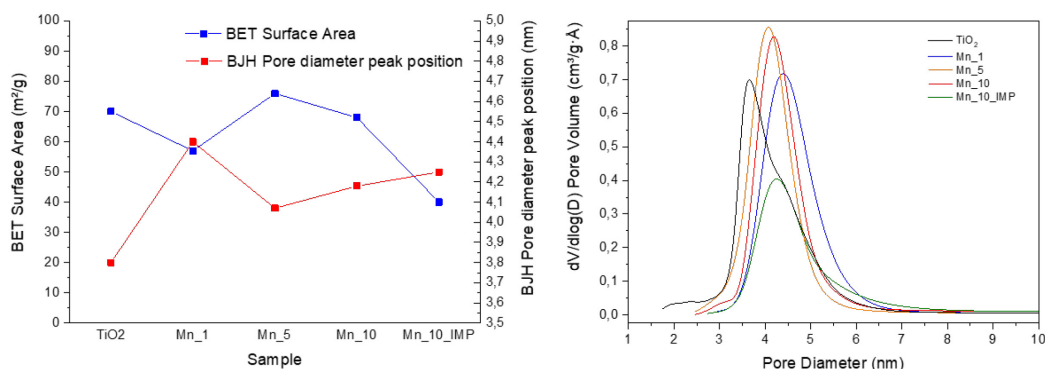
Figure 3.3-11: Surface area and pore diameter for undoped and Mn-doped samples.

Table 3.3-4: Surface texture properties of prepared samples.

Mn synthesis content (wt %)	BET SSA (m²/g)	BJH Cumulative Pore Volume (cm³/g)	BJH Pore diameter peak position (nm)
0	70	0.0900	3.8
1	57	0.0962	4.4
5	76	0.1092	4.1
10	68	0.1020	4.2
10*	40	0.0700	4.3

* impregnated

Thermal analysis (H₂-TPR and TGA)

As a complementary technique of XRD, hydrogen TPR can detect the presence of manganese oxides on atomic level on the opposite of XRD and Raman in terms of hydrogen consumption due to reduction reactions on the surface. It is also important to evaluate the reducibility of the TiO_2 doped samples as it is known that the ease of reduction of metals promote catalytic reactions such as the low-temperature SCR activity [186].

H_2-TPR (Temperature Programmed Reduction) analysis was carried out on a TPD/R/O 1100 ThermoQuest instrument using 50 mg per sample. The powder was held under constant flow (20 mL min^{-1}) of 5% H_2/Ar mixture and heated from room temperature to 900 ° with a ramp of 10 °C min^{-1}. H_2 uptake was then normalized by sample weight, while TGA (Thermogravimetric analysis) has been performed with a TA Instrument Q50. Samples were held at 50°C for 15 minutes to equilibrate, followed by a thermal ramp of 10 °C min^{-1} till 1000 °C were reached under a purge flow of 60 mL min^{-1} of Ar gas. Results of H_2 consumption between ambient temperature and 800 °C for prepared samples are illustrated in Fig 3.3-12 and reported with the integral H_2 consumption for each sample in Table 3.3-5. The consumption data has been related to the EDX manganese atomic percent content

and is presented inf Fig. 3.3-11. The trend results almost linear in the whole range with doping atomic content.

Table 3.3-5: Integral H$_2$ consumption of H$_2$-TPR analysis.

Sample	H$_2$ consumption (total) (mmol/g)
10% IMP	2.01872
10% OP	0.73728
5% OP	0.36353
1% OP	0.12922
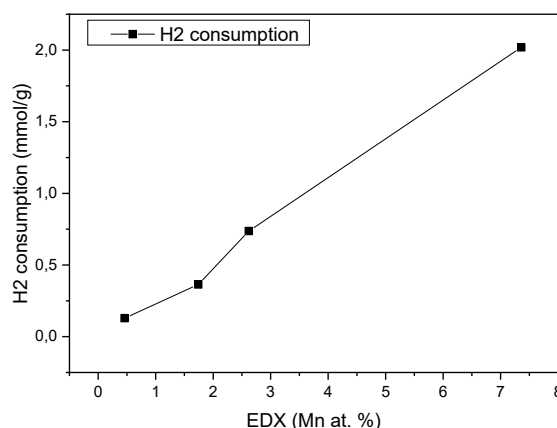
Figure 3.3-12: Hydrogen consumption as a function of EDX manganese atomic percent content detected for 1, 5, 10 and 10% manganese impregnated samples.

As basic assumptions we know that:

1) As general rule, high valence ions of transition metals are reduced at lower temperature than low valence ions, so the reduction process of manganese oxides takes place in the following order in accordance with [187][176]: MnO_2 -> Mn_5O_8 -> Mn_2O_3 -> Mn_3O_4 -> MnO (Mn^{+4} -> mixed Mn^{+4}/Mn^{+3} -> Mn^{+3} -> mixed Mn^{+3}/Mn^{+2} -> Mn^{+2}), in the ranges of 290–350 °C for MnO_2 reduction (up to 430 for β-MnO_2), 350–420 °C for Mn_2O_3 and 450–500 °C for Mn_3O_4 [177][188][189]. Furthermore, MnO_2 exists in several shapes and crystallographic forms as different polymorphs: α, β, γ and δ-MnO_2, whose prevalence depend strongly on temperature condition of the synthesis route. Their reducibility is in the order δ, α, γ, β [190];

2) support oxide determines the reactivity of the bridging M–O–Support functionalities [191] and so the sample preparation route, morphology (surface area, porosity) and oxidation state can influence peak positions [192]. A strong interaction with the support can cause a shift of the transition metal oxides to higher temperatures;

3) bulk reactions occur at higher temperatures than surface reactions;

4) reduction temperature depends on H$_2$ partial pressure and heating rate;

5) particle size, lattice oxygen mobility and structural defects had been established in the literature that cause shift in the peak position of the reduction temperature [193].
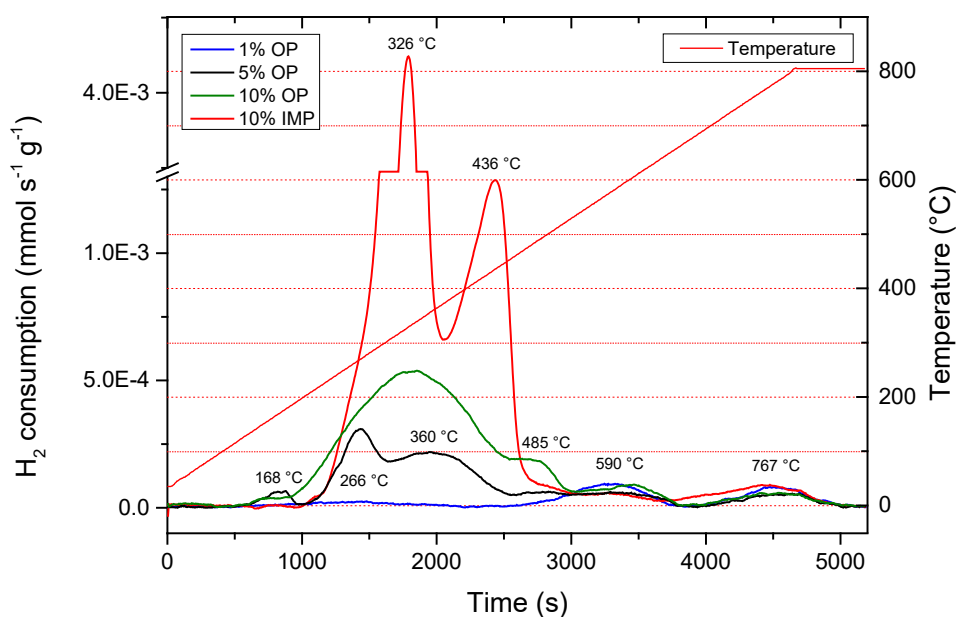
Figure 3.3-13: H_2-TPR using 5% H_2 in Ar. Specific H_2 consumptions vs time are reported for 1,5,10 wt% Mn doped TiO₂ and 10 wt% impregnated TiO₂ nanoparticles with peaks temperature values.

For all these reasons, literature comparisons are challenging, nevertheless from the acquired data we can deduce that the low doped TiO_2 is characterized by a weak reduction behaviour and a H_2 consumption only after 500 °C as extensively reported in literature [177][194] due to the hardly reducible support. For instance, the peak at 590 °C can be ascribed to reduction of surface Ti^{4+} [195]. The main peak located at 266-326 can be attributed to the reduction of highly dispersed and/or easily reducible MnO_2 that was not clearly detected by XRD, which need enough large crystallites; peaks at 360-436 °C are related to Mn_2O_3 [189], bulk MnO_x or β-MnO_2 phases that are reduced to Mn_3O_4 and/or MnO, with lower temperatures for the 5% and 10% one-pot synthetized samples. A small reduction peak located around 485 °C could be attributed to reduction of Mn_3O_4 to MnO. A very low temperature reduction peak at 168 °C and a shoulder around under 266 °C can also be observed for 5 and 10% OP samples. These features represents the reduction of Ti^{4+} to Ti^{3+} and Mn^{4+} (MnO_2) to Mn^{3+} respectively due to interaction between titania support and manganese oxide species [177], facilitating the reduction of high valent ions due respect to single phases taken alone. These reduction temperatures are lower than those reported by Ettireddy et al on anatase Mn-TiO_2 doped titania (Hombikat[1]). It is interesting to notice a higher heterogeneity of manganese oxides species for 10% sample, with a more pronounced shoulder around 200 °C and 485

---

[1] https://www.americanelements.com/hombikat-13463-67-7

°C. The impregnated sample have instead a dominant MnO_2 reduction peak followed by the Mn_2O_3 reduction at 436 °C that forms mainly MnO and only a lower fraction of Mn_3O_4.

Likewise, TGA in inert argon flow has been done for all the samples (Fig. 3.3-13) to get more insight into phases transitions and water and oxygen evolutions. A first feature can be observed from 200 to 350 °C only for the impregnated sample and is assigned to loss of structural water from MnO_2 [196][197]. Peaks located at 200-350 °C and the high temperature peaks in the 500 and 650-750 °C ranges are caused by oxygen evolution due to MnO_2 and Mn_2O_3 decomposition to Mn_2O_3 and Mn_3O_4 respectively [198] (Equations 3.3-1 and 3.3-2).

$$MnO_2 \xrightarrow{\Delta} \frac{1}{2}Mn_2O_3 + \frac{1}{4}O_2 \qquad (3.3-1)$$

$$Mn_2O_3 \xrightarrow{\Delta} \frac{1}{2}Mn_3O_4 + \frac{1}{6}O_2 \qquad (3.3-2)$$
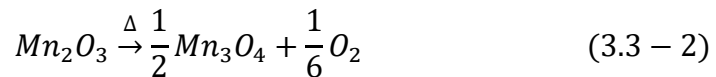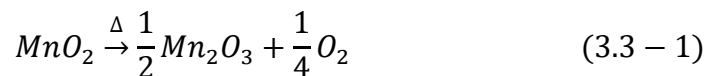
In the H_2-TPR profile, the peaks associated with these decompositions are located at lower temperatures (436-486 °C) as hydrogen has been used instead of argon gas, thus promoting the reduction reactions.
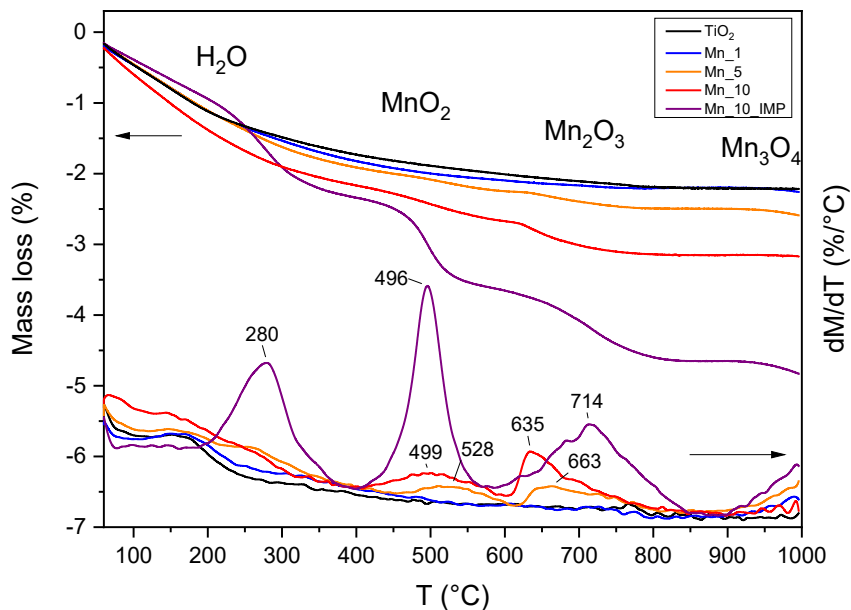
Figure 3.3-14: TGA profiles in Ar flow of bare TiO_2 and Mn-TiO_2 doped samples (1, 5, 10 w% one-pot synthetized and 10% impregnated).

Is also interesting to notice the higher hydration for Mn_10 and Mn_10_IMP samples as shown from the relative mass loss till 350 °C, where also the structural water is removed. As the BET surface area of the Mn_10 sample (68 m^2/g) and

Mn_10_IMP (40 m^2/g) are lower than the bare TiO$_2$ (90 m^2/g), one can conclude that the higher amount of water adsorbed can be caused by another factor apart from surface area, like a more hydrophilic surface due to the presence of manganese oxides, especially for the Mn_10 sample where no structural water peak is visible.

Zeta potential

To acquire insight of the surface acidity/basicity, samples were also characterized to obtain the *pH$_{IEP}$* (or PZC with the assumption of no ion adsorbed on the powder surface). The ζ-potential curves acquired with the same methodology and instrumentation of undoped titania (chapter 3.2) and are reported in figure 3.3-14 along with the corresponding points of zero charge. As Manganese content increases the surface became more basic as PZC overall increases from 3.5 of undoped TiO$_2$ to the highest value of circa 6 for Mn_1 sample.
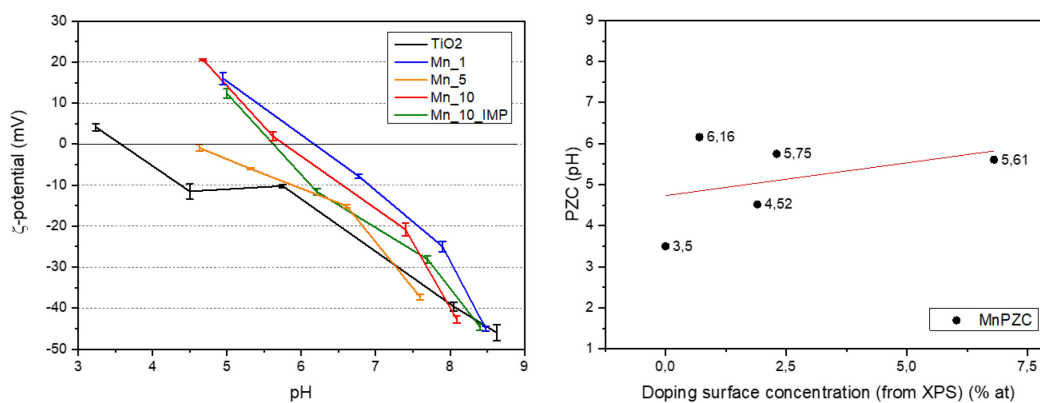
Figure 3.3-15: ζ-potential curves at different pHs (left) and corresponding points of zero charge (right) for TiO$_2$ and Mn-doped TiO$_2$ samples.

Diffuse Reflectance UV-Vis spectroscopy
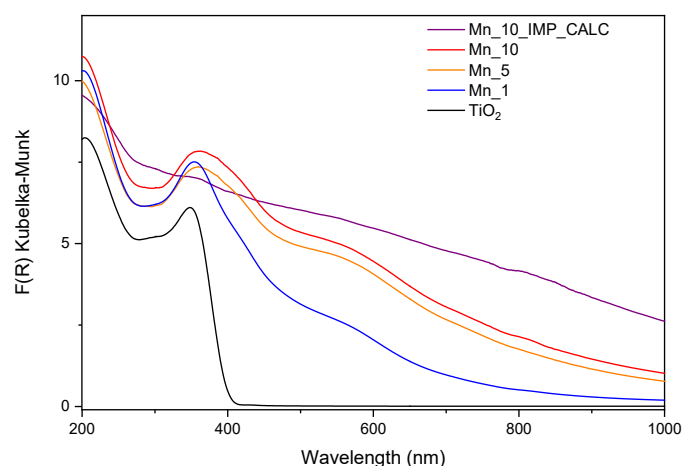
The optical absorption at wavelengths shorter than 400 nm is mainly attributed to the electron transitions from the valence band to conduction band (band-to-band transition, O 2p → Ti 3d).With incorporation of dopant ions, the absorption edge is extended to the broader visible region up to over 1000 nm for the impregnated sample, and hence a red shift is observed in the doped TiO₂ attributed to different causes: optical absorption at the wavelength range from 400 nm to 550 nm results from sub-band transitions closely related to the surface oxygen vacancies (SOVs) , the impurity levels created by $Mn^{2/3/4+}$ ions within the band gap of TiO_2. Due to the different valence states of Mn ions due respect the host (Ti^{4+}), oxygen deficiencies are generated along with e extra energy levels which are responsible for the apparent red shift [199].

3.3.3 Catalytic test application: SCR of NOx

SCR of NOx (NO and NO₂) with NH₃ to harmless N₂ and H₂O proceeds by the overall reactions:

$$4NO + 4NH_3 + O_2 \rightarrow 4N_2 + 6H_2O \quad (3.3\text{-}1)$$
$$4NH_3 + 6NO \rightarrow 5N_2 + 6H_2O \qquad\quad (3.3\text{-}2)$$
$$2NH_3 + NO + NO_2 \rightarrow 2N_2 + 3H_2O \quad (3.3\text{-}3)$$
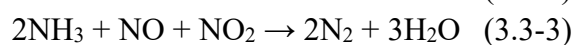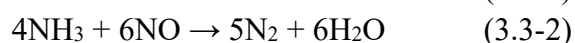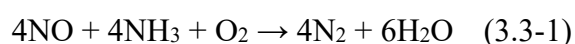
Equation (3.3-1) is the so-called *standard SCR reaction* which implies a 1:1 stoichiometry between NH₃ and NO. The reaction (3.3-2) where oxygen is not involved is much slower and therefore can be neglected. On the other hand, the reaction rate of (3.3-3) with equimolar amounts of NO and NO₂, is much faster than (3.3-1). As side reactions, commonly used catalysts tend to form nitrous oxide (N₂O) at high temperatures (>400 °C). One of the possible reactions is described in equation (4) where N₂O can derive from direct reaction of NO (or NO₂ using one oxygen instead of three) [200][201] with adsorbed NH₃. As temperatures increase to 500 °C and above, the undesirable oxidizing behaviour of the SCR catalysts become important and the oxidation of NH₃ to NO tend to limit the maximum NO_x conversion (3.3-5), while at lower temperatures below 200 °C ammonium

nitrate (NH_4NO_3) can be produced according to Eq. (3.3-6) [202]. N_2O can also be formed from direct oxidation of ammonia in the presence of oxygen (Eq. 3.3-7) [203].

$$4NH_3 + 4NO + 3O_2 \rightarrow 4N_2O + 6H_2O \qquad (3.3\text{-}4)$$
$$4NH_3 + 5O_2 \rightarrow NO + 6H_2O \qquad (3.3\text{-}5)$$
$$2NH_3 + 2NO_2 \rightarrow NH_4NO_3 + N_2 + H_2O \qquad (3.3\text{-}6)$$
$$2NH_3 + 2O_2 \rightarrow N_2O + 3H_2O \qquad (3.3\text{-}7)$$
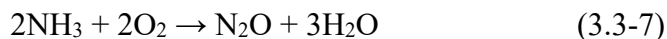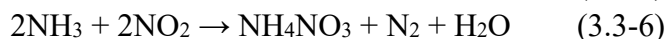
SCR of NO_x was carried out by placing 500 mg catalyst powder in a fixed bed tubular quartz reactor (inner diameter = 10 mm) under a total feed gas flow rate of 300 NmL min^{-1} which translates to gas hourly space velocity (GHSV) to about 50000 h^{-1} as values above 30000 h^{-1} are typically used industrially. The gas mixture had the following composition: 500 ppm NO, 500 ppm NH_3, 3% O_2, and balance N_2. Catalytic tests were performed under isothermal conditions, by raising the temperature from 50 to 350 °C with steps of 32 °C, and by waiting to reach stable temperature and concentrations of the reactive species before each temperature increase.

The NO_x concentration was analysed by means of a NO/NO_2 UV Limas gas analyser (ABB SpA), and the N_2O and NH_3 concentrations by a ND-IR Uras gas analyser (ABB SpA). The NO_x and NH_3 conversions and the N_2 selectivity were calculated from gases concentration according to the following equations:

$$NO_x \ (NO + NO_2) \ conversion \ [\%] = \ 100 \times (NO_{x \ in} - NO_{x \ out})/NO_{x \ in} \quad (3.3 - 8)$$
$$N_2 \ selectivity \ [\%] = \ 100 \times N_2/(N_2 + N_2O) \qquad (3.3 - 9)$$
$$Yield \ [\%] = \ N_2 \ selectivity \times NO_x \ conversion \qquad (3.3 - 10)$$

The results of catalytic activity in terms of NOx conversion and N_2 selectivity of all samples operating under identical experimental conditions are illustrated in Fig. 3.3-17a and 3.3-17b, whereas the yield (Eq. 3.3-1) is reported in Fig. 3.3-18 with an error lower than 5% due to the 5ppm limit of the instrument. As can be seen from these results, the flat line represents the bare titania, while we can notice that the 10% Mn doped material reaches higher conversion than the impregnated sample and performs almost always higher selectivity. In fact, the highest conversions are achieved for 10 and 5% Mn doped TiO_2, but only the 5% sample reaches also high selectivity, as can be more easily expressed by the yield plot, with the highest value of around 80% at 205 °C. At this temperature the material provides peaks of 87% NOx conversion and 98.7% N_2 selectivity. At higher temperatures NO oxidation to NO_2 is an exothermic reversible reaction and as such is less favoured thermodynamically at higher temperature and limited by the thermodynamic equilibrium. NO oxidation is thus kinetically controlled at low temperatures whereas thermodynamically controlled at higher temperatures.
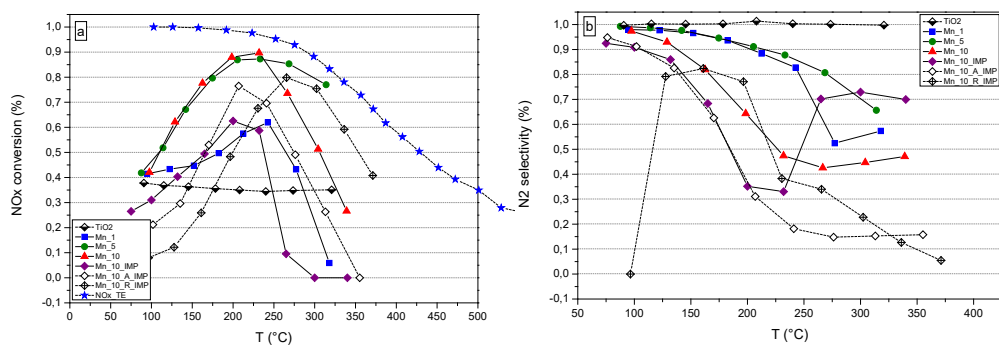
Figure 3.3-17: (a) NOx conversion and selectivity (b) for samples 1, 5, 10 %w (Mn_1-10), and 10%w impregnated (Mn_10_IMP) with references of: pristine TiO₂, Mn impregnated on anatase (Mn_10_A_IMP) and rutile (Mn_10_R_IMP) TiO₂ nanoparticles. NO₂/NOx in thermodynamic equilibrium is denoted with blue stars.
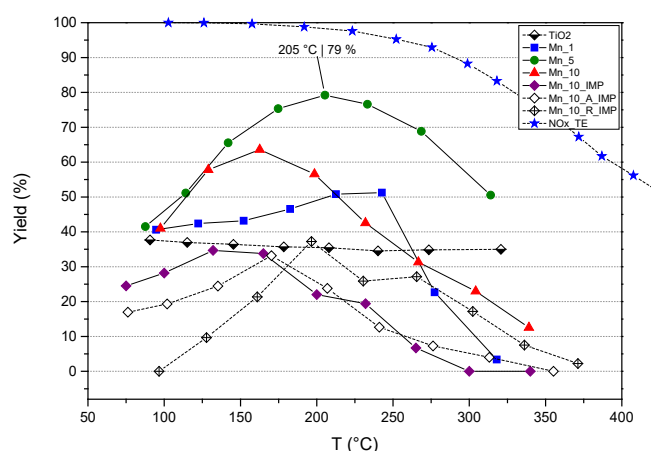
Figure 3.3-18: Yield (equation 3.3-10) for all the samples and NO₂/NOx in thermodynamic equilibrium (blue star)

As preliminary catalytic test of NOx removal, results are promising with margins of improvement as doping concentration can be finely tuned and co-doping can be explored.

3.4 Molybdenum doped Titania

3.4.1 Synthesis of Molybdenum doped Titania

As in the case of Manganese doped Titania, Mo-doped TiO_2 NPs were prepared by the same sol–gel reverse micelle microemulsion method [14] where the used Mo precursor was the ammonium heptamolybdate tetrahydrate salt $((NH_4)_6Mo_7O_{24} \cdot 4H_2O$, purum p.a. $> = 99.9\%)$ as this molybdate is often preferred in catalyst preparations due to its greater solubility than the dimolybdate, allowing higher concentrations of Mo to be used. Proper precursor amounts were used in order to obtain different nominal contents from 0 to 10. % wt Mo/(Mo+TiO₂), together with similar process procedure of Mn doped TiO_2 powders described in the previous chapter.

3.4.2 Textural, optical and surface properties of Manganese doped Titania

X-Ray Powder Diffraction and Raman spectroscopy

Figure 3.4-1a reports the powders XRD patterns from 20 to 90 2θ range of TiO2, and Mn_1/5/10 samples. As already described in chapter 3.2, the TiO$_2$ sample showed the main peaks of anatase (labelled by asterisks), along with the additional broad peak of brookite (circle label). The presence of such phase can be assigned to the adopted synthesis and the calcination temperature. The XRD patterns of the Mo_1 sample did not differ much from those of TiO$_2$, whereas with both Mo_5 and Mo_10 samples two additional peaks (marked with a cross) at 27.2 and 54.4 2θ values are respectively assigned to the (110) and (211) diffraction peaks of rutile. From powder diffraction, no signals ascribable to MoOx phases were detected or can be discerned using Rietveld refinement (main peaks in order of intensities at 2θ values of 27.3 (021), 23.3 (110) and 12.8 (020) ref. code 01-076-1003 for MoO$_3$; 25.7 (110), 36.7 (101) and 53.2 (211) ref. code JCPDS 01-074-4517 for MoO$_2$), even at the highest Mo content: Mo-containing phases, if present, could be very well dispersed-amorphous and cannot be detected by XRD. Crystallite sizes for all detected phases, volume and cell parameter *c* for the dominant phase (Anatase) and phases content are reported in table 3.4-1 and graphically reported in figure 3.4-2a and b including two additional Mo concentration samples to have a better trend estimation.
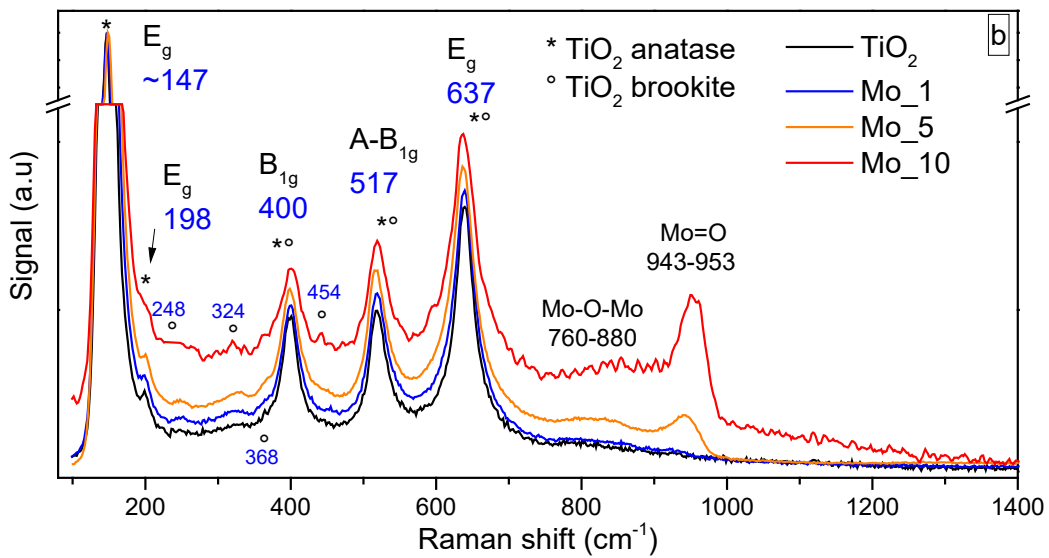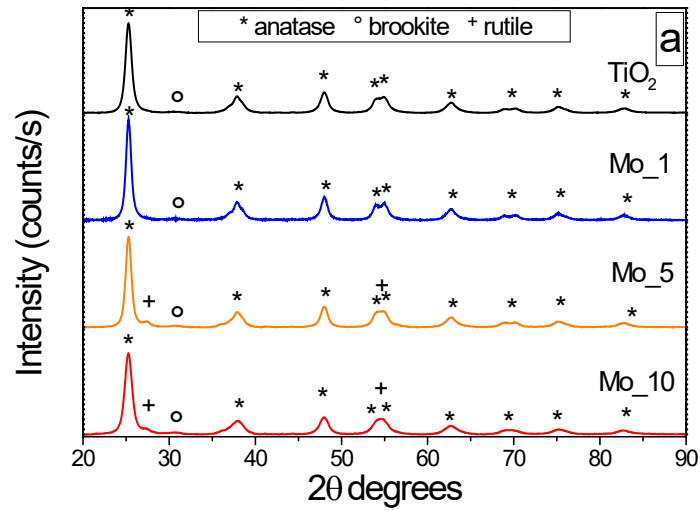
Figure 3.4-1: XRD patterns (a) and Raman spectra (b) of undoped TiO₂ and 1, 5 and 10% Mo doped powder samples.

Crystallites sizes of all phases tend to increase up to the 5-7.5% doping values. Trends that is in contrast to the monotonic decrease of crystallites size of Mo-doped TiO₂ obtained by using the hydrothermal method of Malik et al [204].

Table 3.4-1: Crystallite sizes, volume and cell parameter *c* for the dominant phase (Anatase) and phases content as calculated using Williamson-Hall method.

	GOF	Anatase	st dev	Brookite	st dev	Rutile	st dev	c (Å)(Anatase)	Cell Volume (Å³)(Anatase)	Anatase	Brookite	Rutile
Mo_0	2,11	10,5	0,4	5,4	0,1	7,8	0,2	9,49	61,97	83,0	14,9	2,1
Mo_1	3,32	11,1	0,4	16,7	0,6	6,9	0,3	9,49	65,28	92,7	4,8	2,4
Mo_2.5	2,7	11,8	0,4	12,2	0,2	8,6	0,2	9,48	62,67	73,6	16,5	9,9
Mo_5	2,65	12,5	0,4	20,9	0,7	8	0,1	9,48	62,23	80,3	12,0	7,7
Mo_7.5	2,61	13,6	0,5	5,05	0,4	8,3	0,2	9,48	62,03	73,5	17,0	9,5
Mo_10	2,55	9,2	0,2	5,64	0,5	4,4	0,1	9,48	61,77	73,5	20,6	6,0

One eye-catching feature in figure 3.4-2a is the lattice and cell volume parameters lowest value for Mo_5 sample.

62
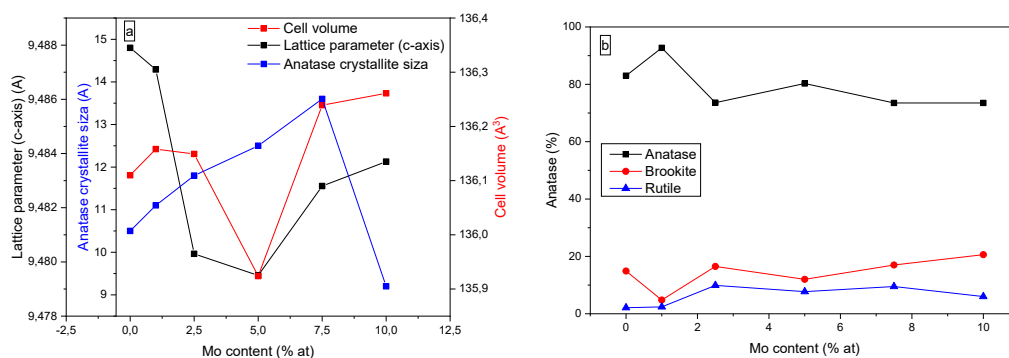
Figure 3.4-2: (a) Lattice parameter *c* and cell volume for the dominant phase (Anatase) for Mo-dopes TiO$_2$ nanoparticles as calculated using Williamson-Hall method. (b) Phase contents of anatase, brookite and rutile.

The Raman spectra in Figure 3.4-1b on the other hand confirm the XRD results detecting the main two phases: with all the samples, the Raman modes of anatase are observed at 147 (E$_g$), 199 (E$_g$), 399 (B$_{1g}$), 519 (B$_{1g}$) and 639 (E$_g$) cm^{-1}, and with the Mo_5 and Mo_10 samples, the band at 639 cm^{-1} is slightly red-shifted (637 cm^{-1}) with respect to undoped TiO$_2$ where the most intense mode of rutile (A$_{1g}$) occurs indeed at 636 cm^{-1} and so the observed shift could be ascribed to the simultaneous presence of both rutile and anatase, in agreement with the corresponding XRD patterns. Additional Raman signals (labelled by circles) are observed and their intensities increasing with the Mo content: they are assigned to the A$_{1g}$ (246 cm^{-1}), B$_{1g}$ (327 cm^{-1} and 448 cm^{-1}) and B$_{2g}$ (362 cm^{-1}) modes of brookite. The most intense band of brookite (B$_{1g}$ mode) usually found at 152 cm^{-1} is likely superposed to that of anatase. Indeed, the maximum of the main peak is blue-shifted with the Mo_10 sample, suggesting a strong interaction of Mo atoms with the TiO$_2$ matrix.

Two additional components are observed in the Mo_5 and Mo_10 samples: peaks at 944 cm^{-1} for 5% doping and 956 cm^{-1} for 10% (asterisk label), and a broad signal occurring in the 760-880 cm^{-1} range. The former signal is assigned to Mo=O groups stretching [205][206], while the high wavenumber peak suggests the presence of Mo$_7$O$_{24}$$^{6-}$ or Mo$_8$O$_{26}$$^{4-}$ species, where Mo is octahedrally coordinated as with systems where comparable amount of MoO$_3$ was supported on TiO$_2$ by incipient wetness impregnation, a similar band was observed in the 934 – 954 cm^{-1} range, shifting to higher wavenumbers with the Mo content, and having a broad and asymmetric shape, as here [207]. Tetrahedral hydrated MoO$_4$$^{2-}$ species (that should give a band at 934 cm^{-1}) are not observed here, even at the lowest Mo content, indicating that Molybdenum doping is mainly related to the TiO$_2$ bulk, whereas for higher Mo contents, formation of polymolibdate species takes place at the surface of the NPs.

N$_2$ adsorption/desorption isotherms, SEM, EDX and XPS

N$_2$ adsorption/desorption isotherms at -196 °C are shown in Figure 3.4-3 of undoped and Mo-doped samples (a), and the corresponding pore size distribution (PSD) as calculated by applying the BJH method to the isotherm desorption branch

(b). All the samples are characterized by a Type IV isotherms with Type H2 hysteresis loop, due to N_2 condensation within intra-particles porosity. The BET SSA value (Table 3.4-2) is almost unaffected for Mo loading up to 5 wt.%, while it increases with the Mo_10 sample. PSD is quite sharp for undoped TiO_2 with peak in the 3 – 6 nm range, suggesting a small distribution of particles size which is confirmed by statistical analysis of FESEM micrography images (Fig. 3.4-6) obtained using ImageJ software. The intra-particle pore size is compatible with the particle size measured by the FESEM analysis (vide infra). Instead, by doping with Molybdenum, the PSD becomes broader for Mo-doped samples, with Mo_5 sample characterized by the broadest PSD in the 3 -14 nm range. Actually, both the size and shape of the particles could affect the BET SSA and the PSDs, and, probably, less homogeneous (in both size and shape) particles are obtained in the presence of Mo.
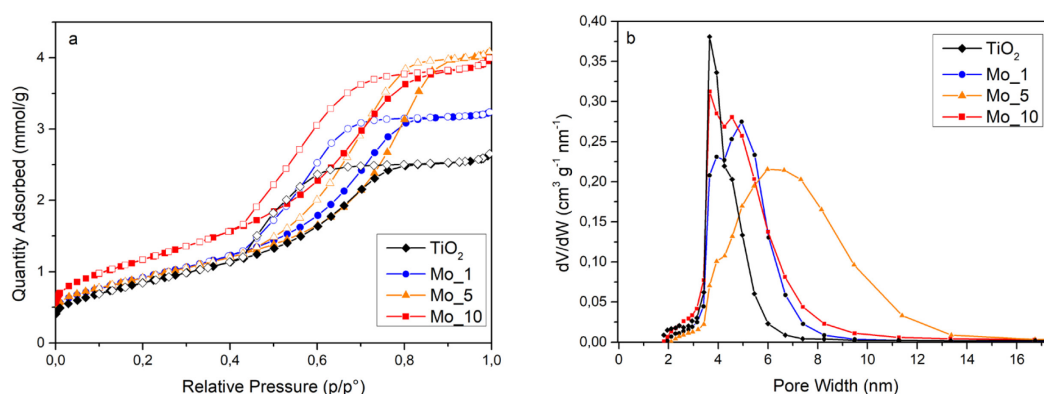
Figure 3.4-3: a) Adsorption/desorption isotherms of N_2 at -196°C and b) pore size distributions of selected undoped and Mo-doped TiO_2 nanoparticles.

Fig. 3.4-4 and 3.4-5 report the FESEM back-scattering electrons and secondary electrons images respectively of pristine and Mo-doped samples of four selected samples. The BSE images black/white contrast emphasizes the Mo rich regions (white spots/clusters), showing a non-uniform distribution of Molybdenum in the whole powder for all samples.

From secondary electron (SE) images, NPs with quasi-round shape are observed, but the addition of Molybdenum seems to lead to a slight size increase due to induced structural changes (Fig. 3.4-6 and Table 3.4-2).
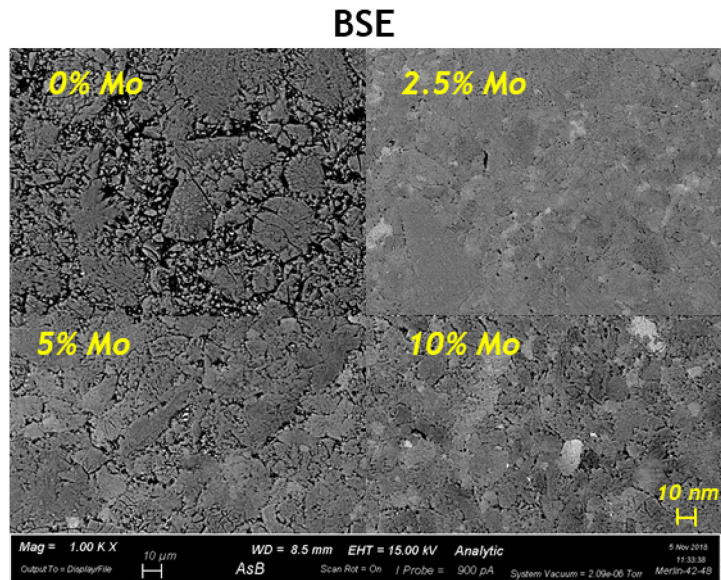
Figure 3.4-4: Back Scattering Electron images of selected undoped and doped TiO₂ powders.
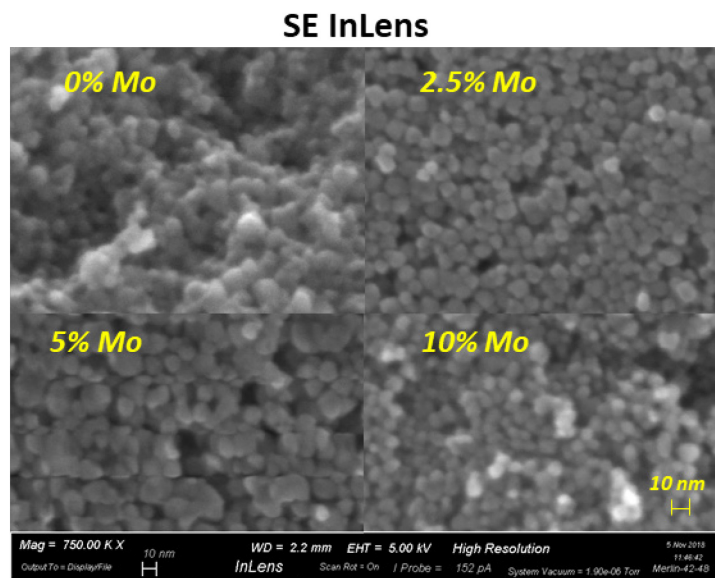
Figure 3.4-5: FESEM secondary electron micrography images of four selected TiO₂ and Mo-doped TiO₂ powders.
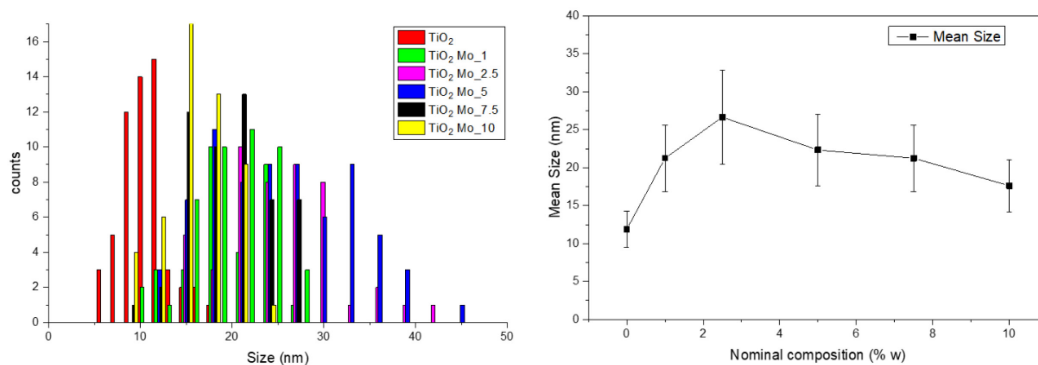
Figure 3.4-6: Statistical distribution of nanoparticles sizes as measured from SE FESEM images.

The EDX analysis allowed us determining the semi-quantitative composition of the samples (Table 3.4-2), showing that in the explored composition range, the actual Mo content was very close to the nominal value as better visible in figure 3.4-7, where the data is graphically represented. As can be seen, the XPS Mo/Ti atomic ratio is quite higher (as surface measure) than bulk/nominal ratio (more than in the case of Manganese doping), suggesting also in this case that Molybdenum prefer the outer nanoparticles shell region instead of a uniform distribution. On the other hand, the similarity of nominal and EDX measured ratios confirm that all the doping material during the synthesis is present in the final product.

Table 3.4-2: Textural and surface properties of the studied samples as determined by N$_2$ isotherms at -196 °C; FESEM; EDX and XPS analyses.

Sample	BET SSA (m^2 g^{-1})	Total pore volume (cm^3 g^{-1})	Average particle size (± 3 nm)	EDX determined Mo/Ti (nominal Mo/Ti) atomic ratios	XPS determined surface Mo/Ti atomic ratio
TiO$_2$	71	0.091	12	-	-
Mo_1	76	0.112	21	0.007 (0.0084)	0.042
Mo_5	74	0.141	22	0.05 (0.044)	0.150
Mo_10	96	0.137	18	0.090 (0.092)	0.194
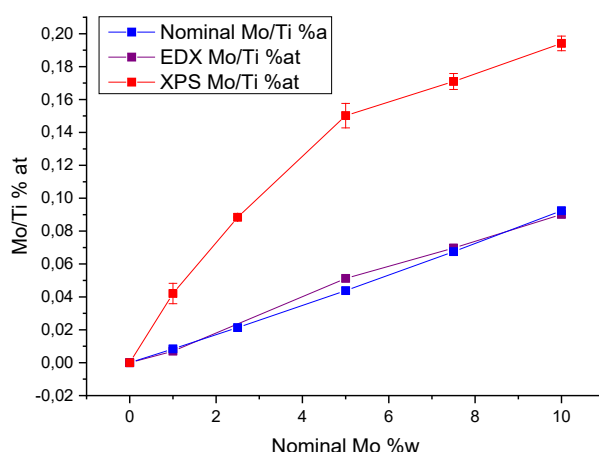
Figure 3.4-7: Distributions of Mo to Ti atomic ratios as measured from XPS (red curve), EDX (violet curve) due respect to nominal synthesis (blu curve) value.

Complementary, XPS shows an almost linear shift of the Ti2p$_{3/2}$ peak component binding energy caused by Mo doping (Fig. 3.4-9). That is an indication that molybdenum atoms indeed are substituting titanium atoms. The curve fitting of Mo3d spectral region (Fig. 3.4-8) shows the typical splitting spin-orbit 3d$_{5/2}$ and 3d$_{3/2}$, resulting in four peaks due to the presence of two different Mo oxidation states: Mo^{5+} (231.4±0.3 eV and 234.1±0.2 eV) and Mo^{6+} (232.7±0.2 eV and 235.9±0.2 eV). Presence of Mo^{5+} ions implied that doped samples are in
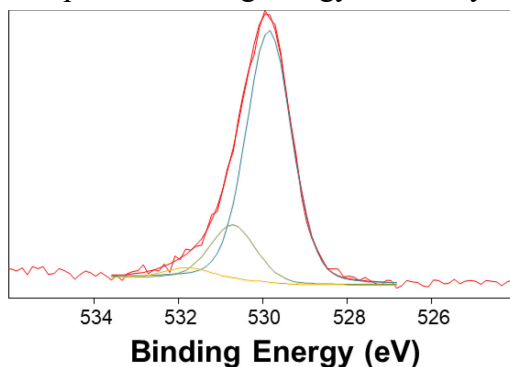
Figure 3.4-8: Mo3d binding energy region of Mo_5 sample.

oxygen deficiency state (as one titanium atom need two O atoms, but one molybdenum atom need three). This is also evident in the O1s XP spectrum (fig. 3.4-10), where the curve fitting procedure resulted in three peaks: the lower binding energy peak is due to lattice oxygen bonded to Ti and/or Mo (529.7±0.2 eV, cyan curve); the higher BE one (around 531.5 ±0.2eV, yellow curve) is attributed to non-lattice oxygen/OH due to adsorption of OH$^-$ on the surface. Lastly, the green curve at 530.6±0.2eV is due to the oxygen in oxygen-deficient. The surface deficiency of O could be complemented by adsorbing more oxygen, which can be beneficial to catalytic properties.
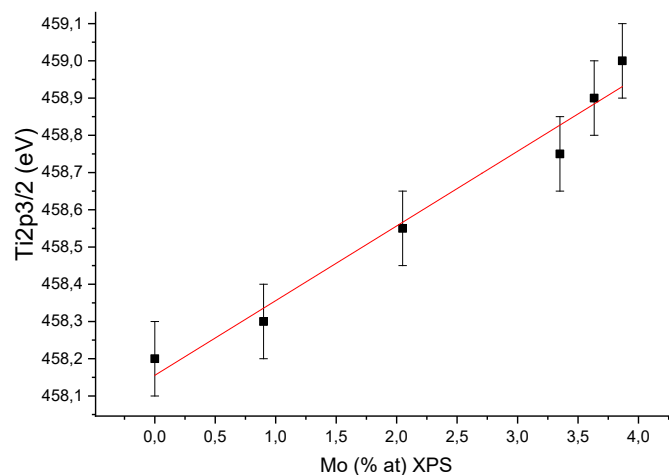
Figure 3.4-9: Ti2p$_{3/2}$ peak position versus Molybdenum doping content as measured by XPS. In red the linear best fit of data.

It is worth noting that the relative abundance of Mo^{5+} is almost independent of the molybdenum loading, with a minimum for the 5% Mo sample (Table 3.4–3).
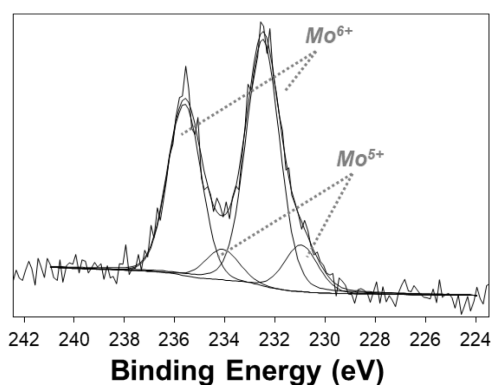
Figure 3.4-10: Typical XP Mo3d and O1s spectra, along with curve fitting results. The attribution of each component to the Mo chemical oxidation state is indicated.

67

Table 3.4-3: Ratio of Mo V and VI oxidation states for Mo-doped TiO$_2$ powder samples as calculated from XPS Mo3d peak area.

	Mo/(Mo+TiO$_2$) %$_{w/w}$				
	1.0%	2.5%	5.0%	7.5%	10.0%
% Mo^{6+}	84±3	80±3	89±3	85±3	84±3
% Mo^{5+}	16±3	20±3	11±3	15±3	16±3

Diffuse Reflectance UV-Vis spectroscopy

Figure 3.4-11 reports the DR UV-Vis spectra of the all produced doped samples. As expected, the TiO$_2$ sample absorbs only below 400 nm, whereas introduction of Mo heteroatoms brings about two main effects: the slight red-shift of the absorption edge and the appearance of a broad absorption band at ca. 545 nm, due to the d-d transitions of Mo atoms. Thus, Mo doping is modifying the band gap (E$_g$) which value had been calculated by the Tauc's plot method and reported, along with XPS valence band edge data, in figure 3.4-12. The two experimentally obtained data allow us to calculate the conductive band edge position (CB) as sum of these two terms previous terms (E$_g$ + VB). Interestingly, the Mo_5 and 7.5 samples showed the lowest E$_g$ values: likely, at higher contents, Mo tends to form surface species, rather than being dispersed in the bulk, as also confirmed by Raman and XPS (*vide supra*), in addition, no localized adsorption peaks are visible in the UV-Vis spectra but only a broad peak is present due to Mo centres, that can be a sign of substitutional doping of Mo in the titania network.
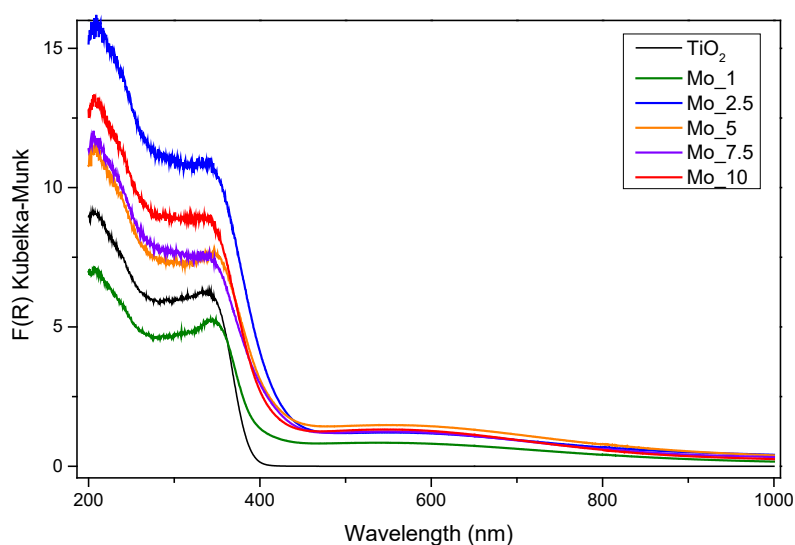
Figure 3.4-11: DR-UV-Vis spectra of TiO$_2$ and Mo-doped powder samples in the 200-1000nm range.
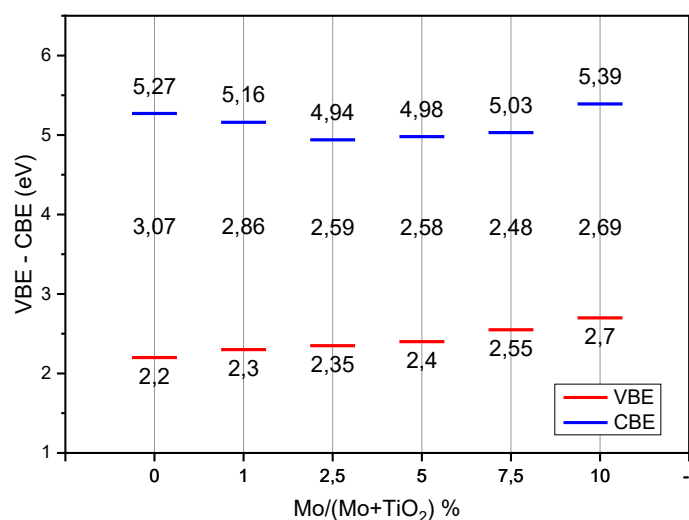
Figure 3.4-12: Diagram of valence (red curve) and conductive energy levels (blu curve) as measured and calculated from DR-UV-Vis and XPS data.

Zeta potential

The ζ-potential measurements (Fig. 3.4-13) show that the undoped TiO_2 sample has a PZC of 3.6, i.e. a value lower than usual for TiO_2: for instance, Degussa P25 (with particle size between 20 and 40 nm) has a PZC around 6.2-6.9 [157][208], or for pure TiO_2 NPs (with diameter in the range of 14 - 33 nm) a PZC of 6.8 [164] was reported; Allard et al found a PZC of 6.1 with commercial anatase NPs (with a diameter of ca. 20 nm) [165]; Al-Hetlani et al found a PZC of 5.98 for smaller anatase NPs (around 7.2 nm [166]); Huijun et al reported a PZC of 6.2 for anatase NPs (5-10 nm) [167].

The much lower value of PZC measured here may be ascribed, rather than to the size of NPs, to the type of synthesis [168,169] that probably favours the formation of a very acidic surface, in agreement with previous work [157]. Addition of Mo leads to a further and progressive decrease of the PZC (Fig. 3.4-13 right), even at the lowest Mo content (sample Mo_1). Such result confirms that the type of synthesis allows distribution of the heteroatoms not only in the bulk, but also at the NPs surface, with some superficial molybdenum ions lowering the PZC, as they are strong Lewis sites.
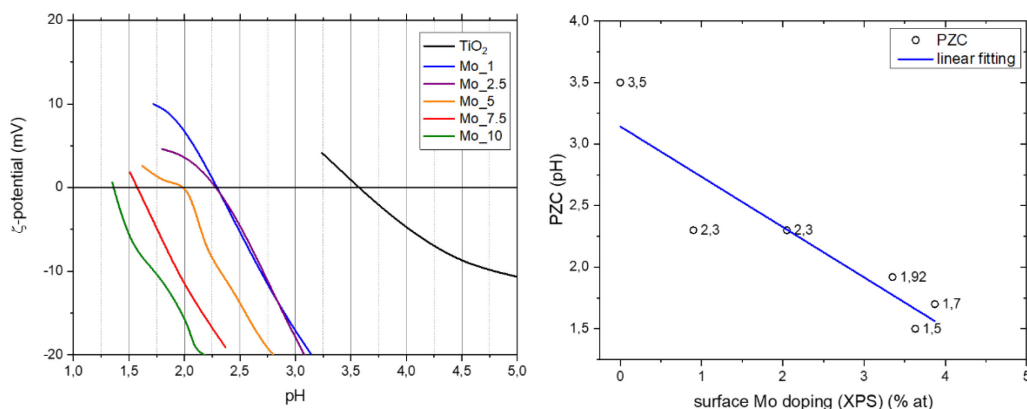
Figure 3.4-13: ζ-potential measurement on undoped and doped TiO₂ samples (left) and point of zero charge vs XPS surface Mo concentration (right).

The ζ potential measurements allowed us to figure out that even at low Mo content the surface of the NPs is affected by the presence of Mo as also highlighted by the XPS measurements (Fig. 3.4-7) which shows that the NPs surface is enriched in Mo atoms with respect to the bulk, in agreement with the type of synthesis adopted.

FTIR – CO probe molecule analysis

Acidity and basicity are tightly related concepts often used to explain the catalytic properties of materials such as metal oxides. To estimate proton-accepting (basic) properties of the surface, infrared spectroscopy for the study of adsorbates, is commonly used. As the coordination of the surface sites is lower than for the bulk ones, they are available for the interaction with probe molecules. Among different molecules, CO adsorption can be exploited to characterize both acidic and basic sites of metal oxides [209][210].

Samples were then characterized by infrared spectroscopy with carbon monoxide probe molecule. IR spectra where recorded at 2 cm⁻¹ resolution by means of a Bruker Equinox 55 FT-IR spectrophotometer, equipped with an MCT (Mercury Cadmium Telluride) cryodetector (Perkin Elmer).

To acquire infrared spectroscopy data in transmission mode using probe molecules, special cells are used as shown in Scheme 3.4-1. Spectra have been recorded at equilibrium conditions (equilibrium pressure and temperature) by closing the line valve and waiting some minutes to let the pressure stabilise as measured by means of an absolute pressure gauge (PIEZOVAC PV 20 Oerlikon Leybold). Moreover, as the interaction with CO molecules is too weak to be observed at room temperature, the sample needs to be cooled down by liquid N₂ by means of a *"cold finger"* on which a gold frame that encapsulate the sample is placed. The sample is fixed in place inside the cell between two KBr windows and the cell is then connected to the vacuum line where balloons of different probe gases can be connected.
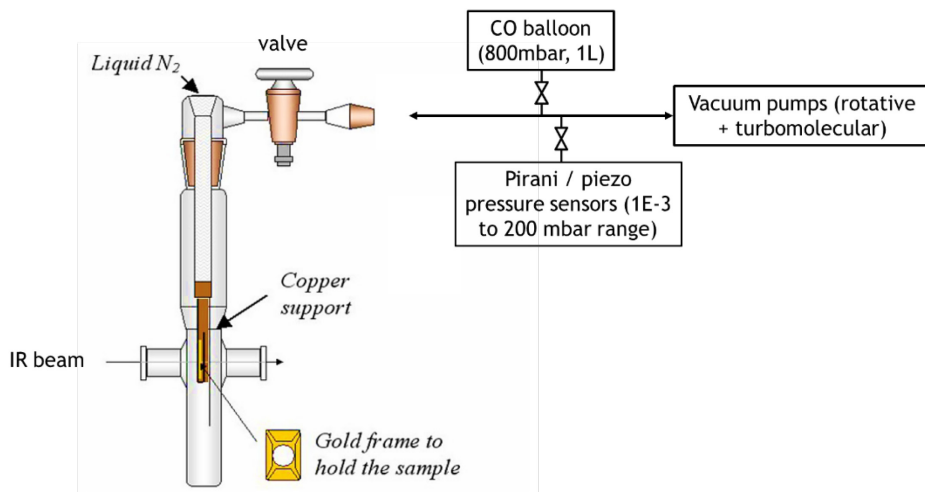
Scheme 3.4-1: Schematic representation of FTIR probe molecule cell setup

Solid samples to be analyzed in transmission mode needs to be carefully prepared in form of pellets with a surface density lower than $20mg/cm^2$ as IR signal would be entirely absorbed by the solid material with higher density. Besides, also lower limits exist, both for physical and signal problems. The former, which is the main issue, is due to mechanical limits (pellet could break), the latter due to interferences caused by thickness in the range of IR wavelength that causes fringes in the FTIR signal. This kind of preparation is exceptionally difficult and time consuming for titania nanomaterial due to its high hardness.
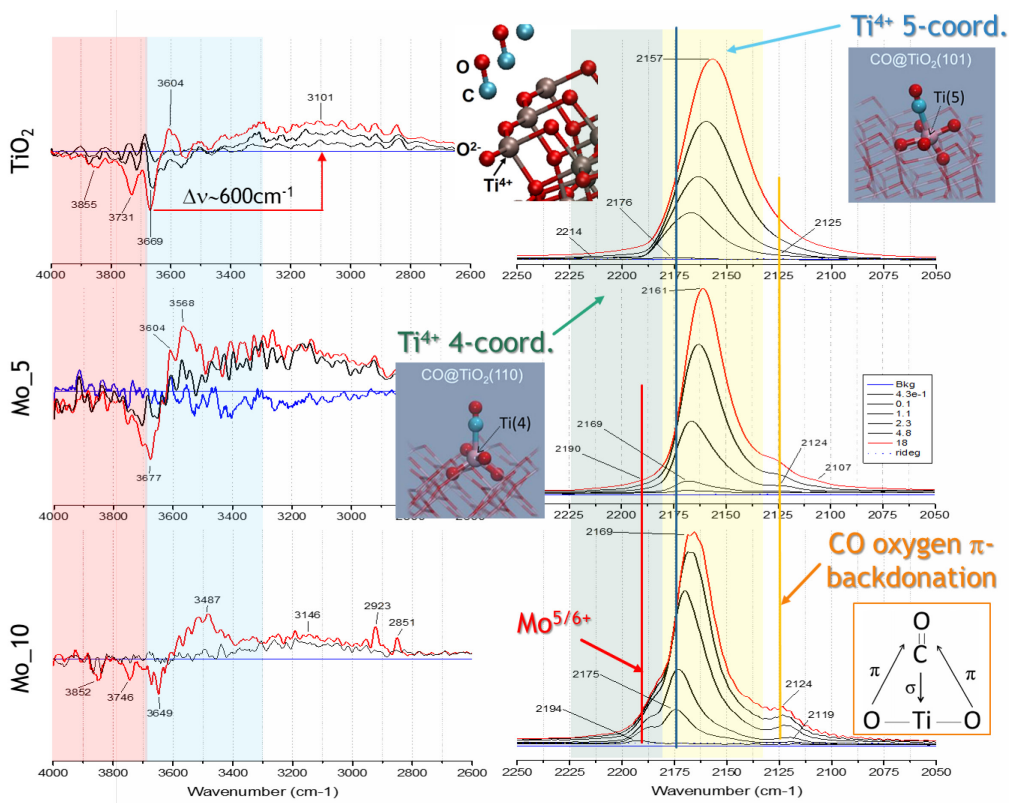
Scheme 3.4-2: FTIR spectra of undoped TiO₂, 5 and 10% Molybdenum doped nanopowders pellets during exposure to CO probe molecules from 10^{-3} to 18 mbar of pressure at liquid N₂ temperature.

Data is summarized and graphically explained in scheme 3.4-2 which shows the νOH (4000-2600 cm^{-1}) and νCO (2250-2050 cm^{-1}) regions for TiO$_2$, Mo_5 and Mo_10 samples previously outgassed at 400°C to remove any trace of water.

Whereas in scheme 3.4-3 are reported a) the representation of main possible surface groups configurations, b) the groups removals/addition due to heath treatment (water removal) and CO interaction and c) the typical IR adsorption regions.

Spectra are presented as difference due respect to the first unprobed IR spectra, so only the changes in intensities due to adsorption of CO are visible.

Unfortunately, producing low surface density pellets (under 10 mg/cm^2) is really difficult, especially for titania, and so OH region is quite noisy.
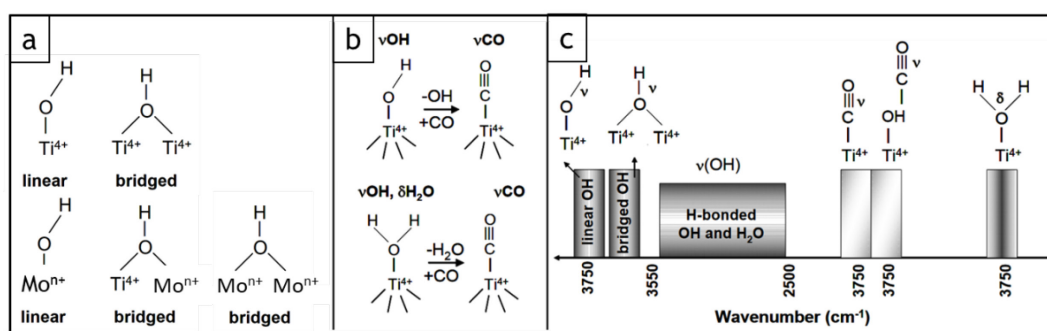
Scheme 3.4-3: a) Schematic representation of possible surface groups configurations for undoped and doped TiO$_2$; b) reactions due to CO interaction and/or after heat treatment; c) typical IR adsorption regions of relevant groups vibrations.

To understand the consequences of CO interaction, a brief overview should be given: when the CO molecules linearly coordinate to surface cations via C atom, three different interactions can be established: 1) Electrostatic (no electron transfer) due to interaction of CO charge distribution and the cation field. 2) σ bond between the HOMO (5σ) of CO and LUMO of metal ion, favoured for metal ions with unoccupied d orbitals. 3) π bond between the LUMO (2π*) of CO and the HOMO (d_{xy}, d_{xz}) of metal ion. 4) π back-donation, when the electron density is transferred from the metal ion to the CO ligand.

Returning to the results in scheme 3.4-2, bands at wavenumbers >3680 cm^{-1} (red highlighted region) were assigned to linear hydroxy groups νOH, while the ones at ν <3680 (blu region) to bridged –OH (Scheme 3.4-3) resulting from the dissociation of H$_2$O on acid-base pairs of coordinatively unsaturated Ti^{4+} and O^{2-} surface sites. Two/tree kind of oxydriles are visible that upon CO exposure shift to lower frequencies of about 400-500 cm^{-1}. This is an indication of quite acidic sites already present in undoped TiO$_2$.

In the linear CO stretching region we can observe the main peek shift starting from 2176 cm^{-1} of CO adsorbed on Ti^{5+} penta-coordinated (yellow highlighted region) beta and gamma sites (010 and 001 planes respectively that differs of ~10 cm^{-1}). An increase of CO pressure/coverage produce an increased interaction among parallel and close oscillators that brings a shift to lower wavenumber of the peak (from 2176 to 2159 cm^{-1}). Additionally, small peaks at wavenumbers >2190 cm^{-1}

(green highlighted region) can be ascribed to surface coordinative defect sites (α Lewis sites) that are more acidic than β and γ (e.g 2214 cm^{-1} Ti^{4+} tetra-coordinated unsaturated Lewis sites at steps-corners-kinks and consequently scarcely available) [211].

As Molybdenum doping increases, two new peaks became visible: at 2194 cm^{-1} due to CO on Mo$^{5/6+}$ (red line) and at 2124 cm^{-1} (orange line) due to CO over oxygen sites that gives pi-backdonation as the frequency increases with covering, trend that is opposed to the CO over Ti^{4+} sites [212]. This peek seems already present in the bare TiO$_2$ but covered by the broad intense peak that now is sharper, probably due to the disappearance of some Ti^{4+} surface site now occupied by Mo$^{5/6+}$.

As a final consideration, as we are dealing with nanometric materials, the broad features of all these peaks, along with small shift compared to crystalline materials, could be caused by surface defects (stressed bonds) and by the presence of secondary phases (brookite and rutile) that have small differences in bond lengths and so different vibrational frequencies that contribute to the broadening of all feature of the IR spectra.

3.4.3 Catalytic test application: degradation of model dye in water solution

In classical heterogeneous catalysis, the overall process can be broken down into five independent steps:

1. transfer of the reactants in the fluid phase to the surface
2. adsorption of at least one of the reactants
3. reaction in the adsorbed phase
4. desorption of the product(s)
5. removal of the products from the interface region
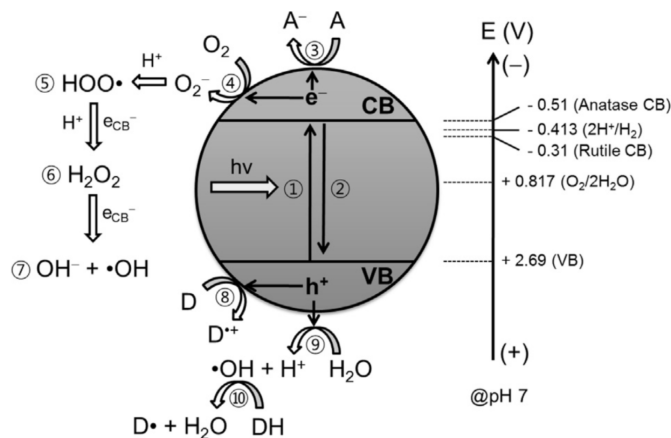
Figure 3.4-14: Main reaction mechanisms of TiO$_2$ photocatalysis with valence and conductive bands schematic. Main process are: 1) electron–hole charge pair creation; 2) charge pair recombination; 3) electron transfer to acceptor A; 4) electron transfer to oxygen molecule; 5) formation of hydroxy peroxyl radical via a reductive pathway and consecutive formation of hydrogen peroxide (6) and hydroxyl radical (7); 8) hole transfer to electron donor D (e.g organic pollutants); 9) hole transfer to surface hydroxyl group to generate

In the case of photocatalysis, the mode of thermal activation of the catalyst is replaced by a photonic activation which act in step 3 that contains all the photoelectronic processes: absorption of the photons if the photon energy is equal to or greater to the band-gap energy ($hv \geq E_G$), creation of electron-hole pairs, which dissociate into free photoelectrons in the conduction band and positive photo-holes in the valence band and finally the electron transfer reactions (charge neutralization, radical formation, surface reactions, etc).

Although, in recent years, photosensitization of dyes has also been reported as possible mechanism in which the dye molecules is the one excited by photons and transfer electrons into the conduction band of TiO_2, resulting in the cationic radicals of the dyes whereas the injected electrons react with O_2 adsorbed on the surface of TiO_2 to generate a series of oxygen radicals as in step 4-7 of figure 3.4-14. The subsequent radical chain reactions lead to the degradation and mineralization of the dye pollutants (step 10)
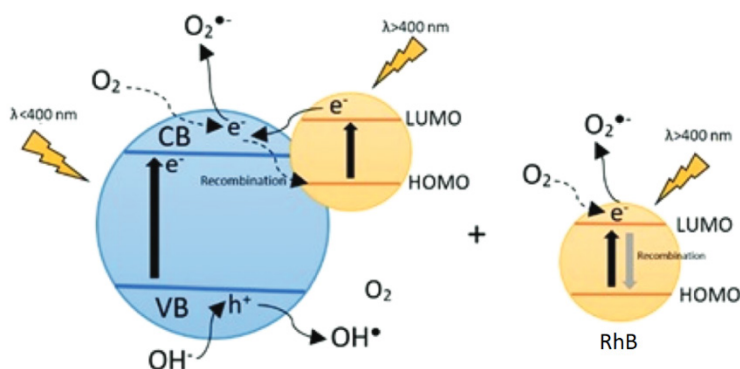
Figure 3.4-15: Schematic diagram of dye sensitization with the dye (yellow sphere) adsorbed onto the TiO₂ surface (blue sphere). [214]

As the ζ-potential measurements suggests that obtained samples are negatively charged in a wide pH range, they should preferably interact with positively charged species, such as the Rhodamine B (RhB) dye [215] (Fig. 3.4-16).
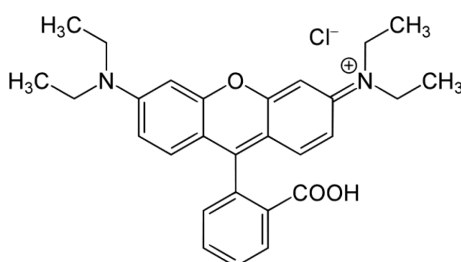
Figure 3.4-16: Scheme of Rhodamine B (RhB) molecule.
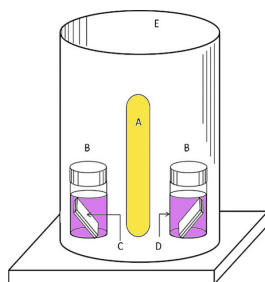
Figure 3.4-17: Diagram of test chamber.

RhB is a cationic Xanthene type dye, characterized by the presence of both diethylamine and carboxylic groups, which is commonly used as a model dye pollutant [216,217]. For these reasons, the photocatalytic RhB degradation was studied in water dispersions of Mo-doped samples and of bare TiO_2 as reference. 40 mg of photocatalyst was added to 50 ml of dye solution of Rh−B at 5mg/liter concentration. To test the feasibility of sun-driven photocatalytic reaction, fluorescent white lamp of 25 watts (spectrum range from 400 nm to 700 nm) was used as light source [218] and positioned as in figure 3.4-17. Each sample was initially left at rest for 60 minutes in dark, then irradiated under lamp. The visible light irradiation with a low irradiance value of 33 W/m^2 was measured at the bottle surface position. Every 60 seconds, suspension was sampled by UV-Vis spectrophotometer (Agilent Cary 60 UV-Vis) in the range 200-700 nm. Figure 3.4-18 shows the Mo_5 UV-Vis spectra case as example. The obtained RhB degradation curves obtained from ethylated rhodamine peak integration (Figure 3.4-19), along with two blank experiments carried out without any catalyst (mere photolysis) and in the presence of a commercial TiO_2 sample (Degussa P25), revealed that, under visible light, photolysis is the slowest process, while the bare titania samples (commercial P25 and our sample) showed indeed promising photodegradation activity towards RhB under Vis light as other mixed phases TiO_2 [219], with the higher activity in the case of our synthetized sample (black filled triangle symbol curve).
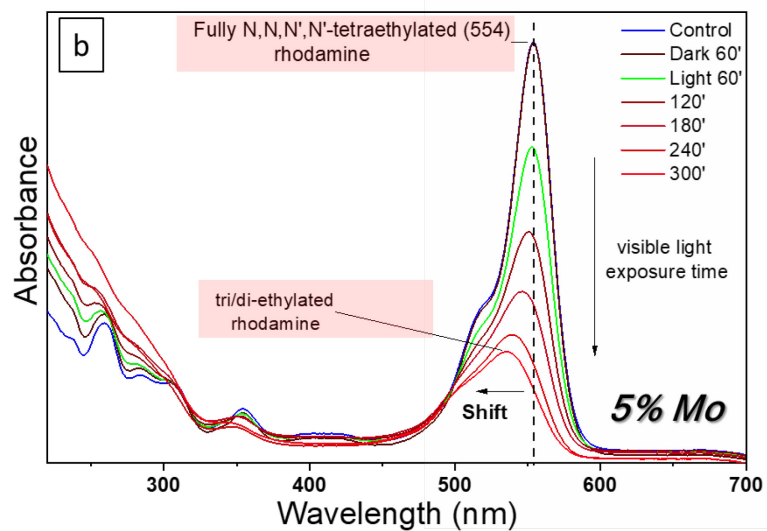
Figure 3.4-18: UV-Vis spectra at different times of RhB in Mo_5 water dispersion under solar light lamp exposure.
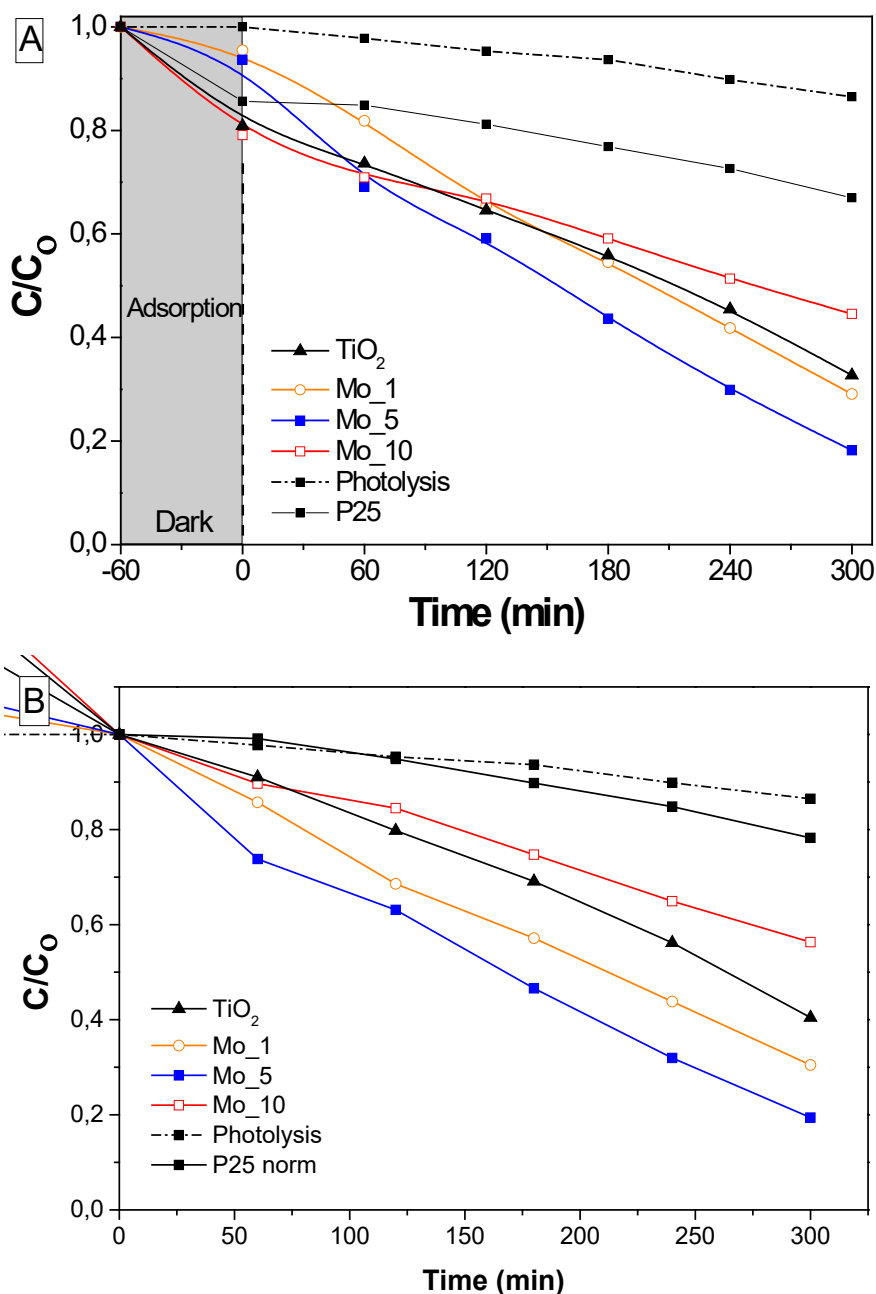
Figure 3.4-19: A) Relative concentration profiles of RhB degradation under visible light for different catalyst powders. B) Normalised C/C₀ values after dark

As compared to the bare TiO_2, the Mo_10 sample showed similar behaviour during the dark time frame, whereas under illumination, degradation efficiency was even lower than that of the bare TiO_2 at a longer reaction time. Considering its smaller band gap ($Eg = 2.69 eV$) and lower PZC, which should favour, respectively, photocatalytic activity and the interaction with diethylamine groups (protonated in the adopted reaction conditions), the (high) Mo content of the Mo_10 sample likely had a detrimental effect on RhB degradation. At a higher content, Mo tends to form surface species, as shown by both Raman and XPS spectroscopies (the Mo_10 sample has indeed a slightly larger band gap ($Eg = 2.69 eV$) than Mo_5 ($Eg = 2.58 eV$)). Nonetheless, the formation of surface polymolibdates (as detected by Raman

spectroscopy) could enhance surface electron/hole recombination, finally decreasing photocatalytic activity. Interestingly, an improved kinetic rate was achieved using Mo_5 sample, characterized by the smallest Eg value (Eg = 2.58 eV). Such results suggest that Mo_5 may have an optimum dopant concentration allowing the best compromise for a better exploitation of the light (due to the lowest band gap) and surface charge characteristics, notwithstanding the adsorption properties of the sample in dark conditions were worse than both TiO_2 and Mo_10, likely due also to the larger particles size of Mo_5 (22 nm). Similar considerations can be drawn for the adsorption behaviour of the Mo_1 sample, where the lower Mo content was instead responsible of its lower activity with respect to Mo_5. Concerning the kind of dye–surface interaction, complex phenomena may occur, such as electrostatic attraction between the protonated diethylamine groups of the dye and the surface negative charge of the samples, or, as RhB also contains carboxylate groups and some positive surface charges that may occur on TiO_2 nanoparticles, especially when Mo ions are at the surface of the NPs. Such combination of interactions could nonetheless improve the degradation rate by cleavage of the Xantene group. This result could be further confirmed from the shift of the main RhB peak from 554 nm to 535 nm observed in the dye UV–Vis spectrum (Figure 3.4-18): such shifts mainly occur when the dye undergoes photocatalytic degradation through a de-ethylation process/route and formation of triethylrhodamine, diethylrhodamine and ethylrhodamine, with different λ_{max} at 555, 539, 522 nm, respectively [216,217].

Conclusions

The *one-pot* synthesis of high surface area nanoparticles synthetized by templated assisted sol-gel (TASG) method, have proved an extremely flexible technique in terms of doping materials that can be used, nanoparticles size control, as well as the "green" and technological advantages such as the low temperatures required.

Both pure and doped TiO_2 NPs (with a size of ca. 10–20 nm), obtained by the reverse micelle sol–gel synthesis method, allowed the dispersion of dopant both in the bulk and at the surface of the NPs with different concentration profile, while substantially avoiding segregation of crystalline Molybdenum or Manganese oxides, even at highest concentration.

The doping of Mn and Mo into TiO_2 lattice shifts the position of its fundamental optical absorption edge toward the longer wavelength lowering its band gap energy so that it can absorb energy from a major portion of visible light, which is extremely important for photocatalytic applications. The 5 wt.% Mo content was found to provide an optimal lowering of the band gap (from 3.07 V for the bare TiO_2 to 2.58 eV), which resulted in the fastest kinetics during the photocatalytic degradation of the model dye Rhodamine B. The synthesis also led to a very acidic (polar) surface, characteristic already present in the undoped TiO_2 sample but enhanced by doping with Mo: the resulting NPs were indeed negatively charged in a wide pH range. This surface negative charge, however, did not enhance the degradation of the dye studied here, especially at the highest Mo content, because the surface polymolibdate species likely acted as recombination centres of electron/hole pair. Despite all this, the high acidity of the NPs surface could be exploited in applications requiring a very polar surface, due to the possibility to polarize some organic pollutant, finally promoting its adsorption and consequent degradation.

Manganese doping, on the other hand, produce a more basic shift of the surface charge, along with the production of oxygen vacancies that increases with doping concentration. Only the 5% and 10% Mn doped TiO_2 by TASG method shows in the H_2-TPR peaks of reduction of Ti^{4+} to Ti^{3+} and Mn^{4+} to Mn^{3+} ascribed to the interaction between titania support and manganese species which facilitate the reduction of high valent ions due respect to the single material phases taken alone (bulk titania and bulk manganese oxides), suggesting a synergy of the two materials in terms of performance for catalytic reduction of NOx gases as suggested by the SCR catalytic test results. The Mn-doped TiO_2, tested at high gas flow rates, outperform the undoped and the 10% Mn-impregnated samples with performance peak at the low temperature of 205 °C.

References

[1]   A. FUJISHIMA, K. HONDA, Electrochemical Photolysis of Water at a Semiconductor Electrode, Nature. 238 (1972) 37–38. https://doi.org/10.1038/238037a0.

[2]   C. Renz, Lichtreaktionen der Oxyde des Titans, Cers und der Erdsäuren, Helv. Chim. Acta. 4 (1921) 961–968. https://doi.org/10.1002/hlca.192100401101.

[3]   B. O'Regan, M. Grätzel, A low-cost, high-efficiency solar cell based on dye-sensitized colloidal TiO_2 films, Nature. 353 (1991) 737–740. https://doi.org/10.1038/353737a0.

[4]   R. van de Krol, Lithium Intercalation in Anatase TiO_2, (2000). https://repository.tudelft.nl/islandora/object/uuid%3A0f055d2a-9f8b-40f2-ab52-35b5196cb6e7.

[5]   G.P. And, P. Reynders, Angle-Dependent Optical Effects Deriving from Submicron Structures of Films and Pigments, (1999). https://doi.org/10.1021/CR970075U.

[6]   A. Salvador, M.C. Pascual-Martí, J.R. Adell, A. Requeni, J.G. March, Analytical methodologies for atomic spectrometric determination of metallic oxides in UV sunscreen creams., J. Pharm. Biomed. Anal. 22 (2000) 301–6. http://www.ncbi.nlm.nih.gov/pubmed/10719913 (accessed June 23, 2019).

[7]   T.A. Egerton, I.R. Tooley, UV absorption and scattering properties of inorganic-based sunscreens, Int. J. Cosmet. Sci. 34 (2012) 117–122. https://doi.org/10.1111/j.1468-2494.2011.00689.x.

[8]   B. Faure, G. Salazar-Alvarez, A. Ahniyaz, I. Villaluenga, G. Berriozabal, Y.R. De Miguel, L. Bergström, Dispersion and surface functionalization of oxide nanoparticles for transparent photocatalytic and UV-protecting coatings and sunscreens, Sci. Technol. Adv. Mater. 14 (2013) 023001. https://doi.org/10.1088/1468-6996/14/2/023001.

[9]   W. Dudefoi, H. Terrisse, M. Richard-Plouet, E. Gautron, F. Popa, B. Humbert, M.H. Ropers, Criteria to define a more relevant reference sample of titanium dioxide in the context of food: a multiscale approach, Food Addit. Contam. - Part A Chem. Anal. Control. Expo. Risk Assess. 34 (2017) 653–665. https://doi.org/10.1080/19440049.2017.1284346.

[10]   N. Shandilya, O. Le Bihan, C. Bressot, M. Morgeneyer, Emission of Titanium Dioxide Nanoparticles from Building Materials to the Environment by Wear and Weather, Environ. Sci. Technol. 49 (2015) 2163–2170. https://doi.org/10.1021/es504710p.

[11]   A.L. da Silva, M. Dondi, M. Raimondo, D. Hotza, Photocatalytic ceramic tiles: Challenges and technological solutions, J. Eur. Ceram. Soc. 38 (2018) 1002–1017. https://doi.org/10.1016/J.JEURCERAMSOC.2017.11.039.

[12]   M.R. Hoffmann, S.T. Martin, W. Choi, D.W. Bahnemann, Environmental Applications of Semiconductor Photocatalysis, Chem. Rev. 95 (1995) 69–96. https://doi.org/10.1021/cr00033a004.

[13]   A.L. Linsebigler, G. Lu, J.T. Yates, Photocatalysis on TiO_2 Surfaces: Principles, Mechanisms, and Selected Results, Chem. Rev. 95 (1995) 735–758. https://doi.org/10.1021/cr00035a013.

[14]   X. Chen, S.S. Mao, Titanium dioxide nanomaterials: Synthesis, properties, modifications and applications, Chem. Rev. 107 (2007) 2891–2959.

https://doi.org/10.1021/cr0500535.

[15] U. Diebold, The surface science of titanium dioxide, Surf. Sci. Rep. 48 (2002) 53–229. https://doi.org/10.1016/S0167-5729(02)00100-0.

[16] T.L. Thompson, J.T. Yates, Surface Science Studies of the Photoactivation of TiO_2 New Photochemical Processes, Chem. Rev. 106 (2006) 4428–4453. https://doi.org/10.1021/cr050172k.

[17] M.M. Mahlambi, C.J. Ngila, B.B. Mamba, Recent Developments in Environmental Photocatalytic Degradation of Organic Pollutants: The Case of Titanium Dioxide Nanoparticles—A Review, J. Nanomater. 2015 (2015) 1–29. https://doi.org/10.1155/2015/790173.

[18] S.T. Martin, A.T. Lee, M.R. Hoffmann, Chemical mechanism of inorganic oxidants in the TiO2/UV process: increased rates of degradation of chlorinated hydrocarbons, Environ. Sci. Technol. 29 (1995) 2567–2573. https://doi.org/10.1021/es00010a017.

[19] W. Choi, M.R. Hoffmann, Novel Photocatalytic Mechanisms for CHCl3, CHBr3, and CCl3CO2- Degradation and the Fate of Photogenerated Trihalomethyl Radicals on TiO_2, Environ. Sci. Technol. 31 (1997) 89–95. https://doi.org/10.1021/es960157k.

[20] M.R. Prairie, L.R. Evans, B.M. Stange, S.L. Martinez, An investigation of titanium dioxide photocatalysis for the treatment of water contaminated with metals and organic chemicals, Environ. Sci. Technol. 27 (1993) 1776–1782. https://doi.org/10.1021/es00046a003.

[21] F. Li, Q. Li, H. Kim, Spray deposition of electrospun TiO_2 nanoparticles with self-cleaning and transparent properties onto glass, Appl. Surf. Sci. 276 (2013) 390–396. https://doi.org/10.1016/J.APSUSC.2013.03.103.

[22] A. Fujishima, K. Hashimoto, T. Watanabe, TiO_2 photocatalysis : fundamentals and applications, BKC, 1999.

[23] R. Wang, K. Hashimoto, A. Fujishima, M. Chikuni, E. Kojima, A. Kitamura, M. Shimohigoshi, T. Watanabe, Light-induced amphiphilic surfaces, Nature. 388 (1997) 431–432. https://doi.org/10.1038/41233.

[24] H. Zhang, J.F. Banfield, Understanding Polymorphic Phase Transformation Behavior during Growth of Nanocrystalline Aggregates: Insights from TiO_2, J. Phys. Chem. B. 104 (2000) 3481–3487. https://doi.org/10.1021/jp000499j.

[25] Z.B. Zhang, C.C. Wang, R. Zakaria, J.Y. Ying, Role of particle size in nanocrystalline TiO2-based photocatalysts, J. Phys. Chem. Biol. 102 (1998) 10871–10878. https://doi.org/10.1021/jp982948+.

[26] H. Zhang, J.F. Banfield, Thermodynamic analysis of phase stability of nanocrystalline titania, J. Mater. Chem. 8 (1998) 2073–2076. https://doi.org/10.1039/a802619j.

[27] G. Oskam, A. Nellore, R.L. Penn, P.C. Searson, The growth kinetics of TiO_2 nanoparticles from titanium(IV) alkoxide at high water/titanium ratio, J. Phys. Chem. B. 107 (2003) 1734–1738. https://doi.org/10.1021/jp021237f.

[28] M. Wu, G. Lin, D. Chen, G. Wang, D. He, S. Feng, R. Xu, Sol-hydrothermal synthesis and hydrothermally structural evolution of nanocrystal titanium dioxide, Chem. Mater. 14 (2002) 1974–1980. https://doi.org/10.1021/cm0102739.

[29] H. Zhang, R.L. Penn, R.J. Hamers, J.F. Banfield, Enhanced Adsorption of Molecules on Surfaces of Nanocrystalline Particles, (1999). https://doi.org/10.1021/JP984574Q.

[30] H.D. Jang, S.K. Kim, S.J. Kim, Effect of Particle Size and Phase Composition of Titanium Dioxide Nanoparticles on the Photocatalytic

Properties, J. Nanoparticle Res. 3 (2001) 141–147. https://doi.org/10.1023/A:1017948330363.

[31] K. Ozawa, M. Emori, S. Yamamoto, R. Yukawa, S. Yamamoto, R. Hobara, K. Fujikawa, H. Sakama, I. Matsuda, Electron–Hole Recombination Time at TiO_2 Single-Crystal Surfaces: Influence of Surface Band Bending, J. Phys. Chem. Lett. 5 (2014) 1953–1957. https://doi.org/10.1021/jz500770c.

[32] B. Szczepanik, Photocatalytic degradation of organic contaminants over clay-TiO_2 nanocomposites: A review, Appl. Clay Sci. 141 (2017) 227–239. https://doi.org/10.1016/j.clay.2017.02.029.

[33] F.S. Freyria, M. Compagnoni, N. Ditaranto, I. Rossetti, M. Piumetti, G. Ramis, B. Bonelli, Pure and Fe-doped mesoporous titania catalyse the oxidation of acid orange 7 by H_2O_2 under different illumination conditions: Fe doping improves photocatalytic activity under simulated solar light, Catalysts. 7 (2017). https://doi.org/10.3390/catal7070213.

[34] J. Moma, J. Baloyi, Modified Titanium Dioxide for Photocatalytic Applications, in: Photocatal. - Appl. Attrib., IntechOpen, 2018. https://doi.org/10.5772/intechopen.79374.

[35] L. Clarizia, G. Vitiello, D.K. Pallotti, B. Silvestri, M. Nadagouda, S. Lettieri, G. Luciani, R. Andreozzi, P. Maddalena, R. Marotta, Effect of surface properties of copper-modified commercial titanium dioxide photocatalysts on hydrogen production through photoreforming of alcohols, Int. J. Hydrogen Energy. 42 (2017) 28349–28362. https://doi.org/10.1016/J.IJHYDENE.2017.09.093.

[36] M. Piumetti, F.S.F.S. Freyria, M. Armandi, F. Geobaldo, E. Garrone, B. Bonelli, Fe- and V-doped mesoporous titania prepared by direct synthesis: Characterization and role in the oxidation of AO7 by H2O2 in the dark, Catal. Today. 227 (2014) 71–79. https://doi.org/10.1016/j.cattod.2013.11.013.

[37] L. Zeng, Z. Lu, M. Li, J. Yang, W. Song, D. Zeng, C. Xie, A modular calcination method to prepare modified N-doped TiO_2 nanoparticle with high photocatalytic activity, Appl. Catal. B Environ. 183 (2016) 308–316. https://doi.org/10.1016/J.APCATB.2015.10.048.

[38] M.A. Hossain, M. Elias, D.R. Sarker, Z.R. Diba, J.M. Mithun, M.A.K. Azad, I.A. Siddiquey, M.M. Rahman, J. Uddin, M.N. Uddin, Synthesis of Fe- or Ag-doped TiO_2–MWCNT nanocomposite thin films and their visible-light-induced catalysis of dye degradation and antibacterial activity, Res. Chem. Intermed. 44 (2018) 2667–2683. https://doi.org/10.1007/s11164-018-3253-z.

[39] J.F. Guayaquil-Sosa, B. Serrano-Rosales, P.J. Valadés-Pelayo, H. de Lasa, Photocatalytic hydrogen production using mesoporous TiO_2 doped with Pt, Appl. Catal. B Environ. 211 (2017) 337–348. https://doi.org/10.1016/J.APCATB.2017.04.029.

[40] C. Lavorato, P. Argurio, T.F. Mastropietro, G. Pirri, T. Poerio, R. Molinari, Pd/TiO_2 doped faujasite photocatalysts for acetophenone transfer hydrogenation in a photocatalytic membrane reactor, J. Catal. 353 (2017) 152–161. https://doi.org/10.1016/J.JCAT.2017.07.015.

[41] C. Jin, Y. Dai, W. Wei, X. Ma, M. Li, B. Huang, Effects of single metal atom (Pt, Pd, Rh and Ru) adsorption on the photocatalytic properties of anatase TiO_2, Appl. Surf. Sci. 426 (2017) 639–646. https://doi.org/10.1016/J.APSUSC.2017.07.065.

[42] Z. Zou, Z. Zhou, H. Wang, Z. Yang, Effect of Au clustering on

ferromagnetism in Au doped TiO$_2$ films: theory and experiments investigation, J. Phys. Chem. Solids. 100 (2017) 71–77. https://doi.org/10.1016/J.JPCS.2016.09.011.

[43] Y. Gai, J. Li, S. Li, J. Xia, S.-H. Wei, Design of Narrow-Gap TiO$_2$: A Passivated Codoping Approach for Enhanced Photoelectrochemical Activity, Phys. Rev. Lett. 036402 (2009) 23–26. https://doi.org/10.1103/PhysRevLett.102.036402.

[44] T. Umebayashi, T. Yamaki, H. Itoh, K. Asai, Analysis of electronic structures of 3d transition metal-doped TiO2 based on band calculations, J. Phys. Chem. Solids. 63 (2002) 1909–1920. https://doi.org/10.1016/S0022-3697(02)00177-4.

[45] J. Wang, R. Li, Z. Zhang, W. Sun, X. Wang, R. Xu, Z. Xing, X. Zhang, Degradation of Hazardous Dyes in Wastewater using Nanometer Mixed Crystal TiO2 Powders under Visible Light Irradiation, Water. Air. Soil Pollut. 189 (2008) 225–237. https://doi.org/10.1007/s11270-007-9570-2.

[46] H. Choi, E. Stathatos, D.D. Dionysiou, Photocatalytic TiO2 films and membranes for the development of efficient wastewater treatment and reuse systems, Desalination. 202 (2007) 199–206. https://doi.org/10.1016/J.DESAL.2005.12.055.

[47] J. Mateo-Sagasta, S.M. Zadeh, H. Turral, More people, more food, worse water? a global review of water pollution from agriculture, n.d. http://www.fao.org/3/ca0146en/CA0146EN.pdf (accessed June 29, 2019).

[48] M. Konsolakis, Recent Advances on Nitrous Oxide (N2O) Decomposition over Non-Noble-Metal Oxide Catalysts: Catalytic Performance, Mechanistic Considerations, and Surface Chemistry Aspects, ACS Catal. 5 (2015) 6397–6421. https://doi.org/10.1021/acscatal.5b01605.

[49] H.S. Rosenberg, L.M. Curran, A. V. Slack, J. Ando, J.H. Oxley, Post combustion methods for control of NOxemissions, Prog. Energy Combust. Sci. 6 (1980) 287–302. https://doi.org/10.1016/0360-1285(80)90020-9.

[50] J.L. Sorrels, D.D. Randall, K.S. Schaffner, C.R. Fry, Chapter 2 Selective Catalytic Reduction, EPA Air Pollut. Control Cost Man. (2016). https://www3.epa.gov/ttn/ecas/docs/SCRCostManualchapter7thEdition_20 16.pdf.

[51] M. Inomata, A. Miyamoto, Y. Murakami, Mechanism of the reaction of NO and NH3 on vanadium oxide catalyst in the presence of oxygen under the dilute gas condition, J. Catal. 62 (1980) 140–148. https://doi.org/10.1016/0021-9517(80)90429-7.

[52] J.A. Dumesic, N.-Y. Topsøe, H. Topsøe, Y. Chen, T. Slabiak, Kinetics of Selective Catalytic Reduction of Nitric Oxide by Ammonia over Vanadia/Titania, J. Catal. 163 (1996) 409–417. https://doi.org/10.1006/JCAT.1996.0342.

[53] E.. B.& W. Tomei, G. L., Steam: its generation and use, 42nd ed., 2015. https://www.babcock.com/-/media/documents/resources/steam-42-sample.ashx (accessed June 19, 2018).

[54] J.L. Xie, Z.B. Fu, F. He, D. Fang, Low Temperature Selective Catalytic Reduction of NO$_x$ with NH$_3$ over MnO$_x$ /TiO$_2$ Catalyst, Appl. Mech. Mater. 295–298 (2013) 364–369. https://doi.org/10.4028/www.scientific.net/AMM.295-298.364.

[55] T. Boningari, P.G. Smirniotis, Impact of nitrogen oxides on the environment and human health: Mn-based materials for the NOx abatement, Curr. Opin. Chem. Eng. 13 (2016) 133–141.

https://doi.org/10.1016/j.coche.2016.09.004.

[56] B. Jiang, Y. Liu, Z. Wu, Low-temperature selective catalytic reduction of NO on MnOx/TiO2 prepared by different methods, J. Hazard. Mater. 162 (2009) 1249–1254. https://doi.org/10.1016/J.JHAZMAT.2008.06.013.

[57] W.S. Kijlstra, D.S. Brands, H.I. Smit, E.K. Poels, A. Bliek, Mechanism of the Selective Catalytic Reduction of NO with NH3 over MnOx/Al2O3, J. Catal. 171 (1997) 219–230. https://doi.org/10.1006/JCAT.1997.1789.

[58] S.R. Taylor, S.M. McLennan, The geochemical evolution of the continental crust, Rev. Geophys. 33 (1995) 241. https://doi.org/10.1029/95RG00262.

[59] R.S. Lima, B.R. Marple, Thermal Spray Coatings Engineered from Nanostructured Ceramic Agglomerated Powders for Structural, Thermal Barrier and Biomedical Applications: A Review, J. Therm. Spray Technol. 16 (2007) 40–63. https://doi.org/10.1007/s11666-006-9010-7.

[60] Anatase mindat.org, (n.d.). https://www.mindat.org/min-213.html.

[61] Brookite mindat.org, (n.d.). https://www.mindat.org/min-787.html.

[62] R. Marchand, L. Brohan, M. Tournoux, TiO2(B) a new form of titanium dioxide and the potassium octatitanate K2Ti8O17, Mater. Res. Bull. 15 (1980) 1129–1133. https://doi.org/10.1016/0025-5408(80)90076-8.

[63] M. Latroche, L. Brohan, R. Marchand, M. Tournoux, New hollandite oxides: TiO2(H) and K0.06TiO2, J. Solid State Chem. 81 (1989) 78–82. https://doi.org/10.1016/0022-4596(89)90204-1.

[64] J. Akimoto, Y. Gotoh, Y. Oosawa, N. Nonose, T. Kumagai, K. Aoki, H. Takei, Topotactic Oxidation of Ramsdellite-Type Li0.5TiO2, a New Polymorph of Titanium Dioxide: TiO2(R), J. Solid State Chem. 113 (1994) 27–36. https://doi.org/10.1006/JSSC.1994.1337.

[65] N.A. Bendeliani, S.V. Popova, L.F. Vereshchagin, New modification of titanium dioxide obtained at high pressure, 3 (1966) 387–390.

[66] L.S. Dubrovinsky, N.A. Dubrovinskaia, V. Swamy, J. Muscat, N.M. Harrison, R. Ahuja, B. Holm, Cotunnite-structured titanium dioxide: the hardest known oxide, (2009). http://arxiv.org/abs/0907.1464 (accessed July 7, 2019).

[67] Y. Al-Khatatbeh, K.K.M. Lee, B. Kiefer, High-pressure behavior of TiO2 as determined by experiment and theory, Phys. Rev. B. 79 (2009) 134114. https://doi.org/10.1103/PhysRevB.79.134114.

[68] O. Tschauner, C. Ma, A. Lanzirotti, M. Newville, Riesite, a new high pressure polymorph of TiO2 that forms upon shock-release - comparison to (Zr,Ti)O2 in pseudotachylites, in: Goldschmidt2017 Abstr., 2017. https://www.its.caltech.edu/~chima/publications/2017_Goldschmidt_riesite.pdf (accessed July 12, 2019).

[69] IMA Commission on New Minerals, Nomenclature and Classification (CNMNC), (n.d.). https://doi.org/10.1180/minmag.2017.081.004.

[70] V. Swamy, A. Kuznetsov, L.S. Dubrovinsky, P.F. McMillan, V.B. Prakapenka, G. Shen, B.C. Muddle, Size-Dependent Pressure-Induced Amorphization in Nanoscale TiO2, Phys. Rev. Lett. 96 (2006) 135702. https://doi.org/10.1103/PhysRevLett.96.135702.

[71] V. Swamy, E. Holbig, L.S. Dubrovinsky, V. Prakapenka, B.C. Muddle, Mechanical properties of bulk and nanoscale TiO2 phases, J. Phys. Chem. Solids. 69 (2008) 2332–2335. https://doi.org/10.1016/J.JPCS.2008.04.018.

[72] D. Machon, M. Daniel, V. Pischedda, S. Daniele, P. Bouvier, S. LeFloch, Pressure-induced polyamorphism in TiO2 nanoparticles, Phys. Rev. B. 82 (2010) 140102. https://doi.org/10.1103/PhysRevB.82.140102.

[73] H. Zhang, J.F. Banfield, Structural Characteristics and Mechanical and Thermodynamic Properties of Nanocrystalline TiO2, Chem. Rev. 114 (2014) 9613–9644. https://doi.org/10.1021/cr500072j.

[74] H. Zhang, B. Chen, J.F. Banfield, The size dependence of the surface free energy of titania nanocrystals, Phys. Chem. Chem. Phys. 11 (2009) 2553. https://doi.org/10.1039/b819623k.

[75] J.R. Eltzholtz, C. Tyrsted, K.M.Ø. Jensen, M. Bremholm, M. Christensen, J. Becker-Christensen, B.B. Iversen, Pulsed supercritical synthesis of anatase TiO2 nanoparticles in a water–isopropanol mixture studied by in situ powder X-ray diffraction, Nanoscale. 5 (2013) 2372. https://doi.org/10.1039/c3nr33127j.

[76] Z. Matěj, L. Matějová, R. Kužel, XRD analysis of nanocrystalline anatase powders prepared by various chemical routes: correlations between micro-structure and crystal structure parameters, Powder Diffr. 28 (2013) S161–S183. https://doi.org/10.1017/S0885715613001061.

[77] G.V. Jensen, M. Bremholm, N. Lock, G.R. Deen, T.R. Jensen, B.B. Iversen, M. Niederberger, J.S. Pedersen, H. Birkedal, Anisotropic Crystal Growth Kinetics of Anatase TiO2 Nanoparticles Synthesized in a Nonaqueous Medium, Chem. Mater. 22 (2010) 6044–6055. https://doi.org/10.1021/cm100469y.

[78] J.-L. Mi, C. Clausen, M. Bremholm, N. Lock, K.M.Ø. Jensen, M. Christensen, B.B. Iversen, Rapid Hydrothermal Preparation of Rutile TiO$_2$ Nanoparticles by Simultaneous Transformation of Primary Brookite and Anatase: An in Situ Synchrotron PXRD Study, Cryst. Growth Des. 12 (2012) 6092–6097. https://doi.org/10.1021/cg301230w.

[79] B. Chen, H. Zhang, K.A. Dunphy-Guzman, D. Spagnoli, M.B. Kruger, D.V.S. Muthu, M. Kunz, S. Fakra, J.Z. Hu, Q.Z. Guo, J.F. Banfield, Size-dependent elasticity of nanocrystalline titania, Phys. Rev. B. 79 (2009) 125406. https://doi.org/10.1103/PhysRevB.79.125406.

[80] G. Li, J. Boerio-Goates, B.F. Woodfield, L. Li, Evidence of linear lattice expansion and covalency enhancement in rutile TiO2 nanocrystals, Appl. Phys. Lett. 85 (2004) 2059–2061. https://doi.org/10.1063/1.1790596.

[81] V. Swamy, D. Menzies, B.C. Muddle, A. Kuznetsov, L.S. Dubrovinsky, Q. Dai, V. Dmitriev, Nonlinear size dependence of anatase TiO2 lattice parameters, Appl. Phys. Lett. 88 (2006) 243103. https://doi.org/10.1063/1.2213956.

[82] A. Sarkar, G.G. Khan, The formation and detection techniques of oxygen vacancies in titanium oxide-based nanostructures, Nanoscale. 11 (2019) 3414–3444. https://doi.org/10.1039/C8NR09666J.

[83] J. Zhang, P. Zhou, J. Liu, J. Yu, New understanding of the difference of photocatalytic activity among anatase, rutile and brookite TiO$_2$, Phys. Chem. Chem. Phys. 16 (2014) 20382–20386. https://doi.org/10.1039/C4CP02201G.

[84] G. Nuspl, K. Yoshizawa, T. Yamabe, Lithium intercalation in TiO2 modifications, J. Mater. Chem. 7 (1997) 2529–2536. https://doi.org/10.1039/a703935b.

[85] S. Yin, Y. Fujishiro, J. Wu, M. Aki, T. Sato, Synthesis and photocatalytic properties of fibrous titania by solvothermal reactions, J. Mater. Process. Technol. 137 (2003) 45–48. https://doi.org/10.1016/S0924-0136(02)01065-8.

[86] B. Ohtani, O.O. Prieto-Mahaney, D. Li, R. Abe, What is Degussa (Evonik)

P25? Crystalline composition analysis, reconstruction from isolated pure particles and photocatalytic activity test, J. Photochem. Photobiol. A Chem. 216 (2010) 179–182. https://doi.org/10.1016/J.JPHOTOCHEM.2010.07.024.

[87] G. Li, K.A. Gray, The solid–solid interface: Explaining the high and unique photocatalytic reactivity of TiO2-based nanocomposite materials, Chem. Phys. 339 (2007) 173–187. https://doi.org/10.1016/J.CHEMPHYS.2007.05.023.

[88] D.O. Scanlon, C.W. Dunnill, J. Buckeridge, S.A. Shevlin, A.J. Logsdail, S.M. Woodley, C.R.A. Catlow, M.J. Powell, R.G. Palgrave, I.P. Parkin, G.W. Watson, T.W. Keal, P. Sherwood, A. Walsh, A.A. Sokol, Band alignment of rutile and anatase TiO2, Nat. Mater. 12 (2013) 798–801. https://doi.org/10.1038/nmat3697.

[89] L. Kavan, M. Grätzel, S.E. Gilbert, C. Klemenz, H.J. Scheel, Electrochemical and Photoelectrochemical Investigation of Single-Crystal Anatase, (1996). https://doi.org/10.1021/JA954172L.

[90] D. Reyes-Coronado, G. Rodríguez-Gattorno, M.E. Espinosa-Pesqueira, C. Cab, R. de Coss, G. Oskam, Phase-pure TiO 2 nanoparticles: anatase, brookite and rutile, Nanotechnology. 19 (2008) 145605. https://doi.org/10.1088/0957-4484/19/14/145605.

[91] J.G. Li, T. Ishigaki, X. Sun, Anatase, brookite, and rutile nanocrystals via redox reactions under mild hydrothermal conditions: Phase-selective synthesis and physicochemical properties, J. Phys. Chem. C. 111 (2007) 4969–4976. https://doi.org/10.1021/jp0673258.

[92] B. Kraeutler, A.J. Bard, Heterogeneous photocatalytic decomposition of saturated carboxylic acids on titanium dioxide powder. Decarboxylative route to alkanes, J. Am. Chem. Soc. 100 (1978) 5985–5992. https://doi.org/10.1021/ja00487a001.

[93] D.A.H. Hanaor, C.C. Sorrell, Review of the anatase to rutile phase transformation, J. Mater. Sci. 46 (2011) 855–874. https://doi.org/10.1007/s10853-010-5113-0.

[94] A. Amtout, R. Leonelli, Optical properties of rutile near its fundamental band gap, Phys. Rev. B. 51 (1995) 6842–6851. https://doi.org/10.1103/PhysRevB.51.6842.

[95] A. Di Paola, M. Bellardita, L. Palmisano, Brookite, the Least Known TiO2 Photocatalyst, Catalysts. 3 (2013) 36–73. https://doi.org/10.3390/catal3010036.

[96] T. Ohsaka, F. Izumi, Y. Fujiki, Raman spectrum of anatase, TiO2, J. Raman Spectrosc. 7 (1978) 321–324. https://doi.org/10.1002/jrs.1250070606.

[97] Y.-H. Zhang, C.K. Chan, J.F. Porter, W. Guo, Micro-Raman Spectroscopic Characterization of Nanosized TiO2 Powders Prepared by Vapor Hydrolysis, J. Mater. Res. 13 (1998) 2602–2609. https://doi.org/10.1557/JMR.1998.0363.

[98] M.N. Iliev, V.G. Hadjiev, A.P. Litvinchuk, Raman and infrared spectra of brookite (TiO2): Experiment and theory, Vib. Spectrosc. 64 (2013) 148–152. https://doi.org/10.1016/j.vibspec.2012.08.003.

[99] G.A. Tompsett, G.A. Bowmaker, R.P. Cooney, J.B. Metson, K.A. Rodgers, J.M. Seakins, The Raman spectrum of brookite, TiO2 (Pbca, Z = 8), J. Raman Spectrosc. 26 (1995) 57–62. https://doi.org/10.1002/jrs.1250260110.

[100] H. Kominami, M. Kohno, Y. Kera, Synthesis of brookite-type titanium oxide nano-crystals in organic media, J. Mater. Chem. 10 (2000) 1151–1156.

https://doi.org/10.1039/a908528i.

[101] J.G. Li, C. Tang, D. Li, H. Haneda, T. Ishigaki, Monodispersed spherical particles of brookite-type TiO_2: Synthesis, characterization, and photocatalytic property, J. Am. Ceram. Soc. 87 (2004) 1358–1361. https://doi.org/10.1111/j.1151-2916.2004.tb07735.x.

[102] T. Xing, J. Sunarso, W. Yang, Y. Yin, A.M. Glushenkov, L.H. Li, P.C. Howlett, Y. Chen, Ball milling: a green mechanochemical approach for synthesis of nitrogen doped carbon nanoparticles, Nanoscale. 5 (2013) 7970. https://doi.org/10.1039/c3nr02328a.

[103] B.N. And, T. Pradeep, Coalescence of Nanoclusters and Formation of Submicron Crystallites Assisted by Lactobacillus Strains, (2002). https://doi.org/10.1021/CG0255164.

[104] K. Prasad, A.K. Jha, A.R. Kulkarni, Lactobacillus assisted synthesis of titanium nanoparticles, Nanoscale Res. Lett. 2 (2007) 248–250. https://doi.org/10.1007/s11671-007-9060-x.

[105] V. Bansal, D. Rautaray, A. Bharde, K. Ahire, A. Sanyal, A. Ahmad, M. Sastry, Fungus-mediated biosynthesis of silica and titania particles, J. Mater. Chem. 15 (2005) 2583. https://doi.org/10.1039/b503008k.

[106] A. Bharde, D. Rautaray, V. Bansal, A. Ahmad, I. Sarkar, S.M. Yusuf, M. Sanyal, M. Sastry, Extracellular Biosynthesis of Magnetite using Fungi, Small. 2 (2006) 135–141. https://doi.org/10.1002/smll.200500180.

[107] V. Bansal, D. Rautaray, A. Ahmad, M. Sastry, Biosynthesis of zirconia nanoparticles using the fungus Fusarium oxysporum, J. Mater. Chem. 14 (2004) 3303. https://doi.org/10.1039/b407904c.

[108] J. Park, J. Joo, S.G. Kwon, Y. Jang, T. Hyeon, Synthesis of Monodisperse Spherical Nanocrystals, Angew. Chemie Int. Ed. 46 (2007) 4630–4660. https://doi.org/10.1002/anie.200603148.

[109] M. Bainbridge, J.S. Clarkson, B.L. Parnham, J. Tabatabaei, D. V. Tyers, K.C. Waugh, Evidence for support effects in metal oxide supported cobalt catalysts, Catal. Struct. React. 3 (2017) 128–137. https://doi.org/10.1080/2055074X.2017.1281718.

[110] M. Campanati, G. Fornasari, A. Vaccari, Fundamentals in the preparation of heterogeneous catalysts, Catal. Today. 77 (2003) 299–314. https://doi.org/10.1016/S0920-5861(02)00375-9.

[111] R. Sui, P. Charpentier, Synthesis of Metal Oxide Nanostructures by Direct Sol–Gel Chemistry in Supercritical Fluids, Chem. Rev. 112 (2012) 3057–3082. https://doi.org/10.1021/cr2000465.

[112] C.J. Brinker, G.W. Scherer, Sol-gel science : the physics and chemistry of sol-gel processing, Academic Press, 1990.

[113] D. Levy, M. Zayat, The Sol-Gel Handbook, 2015. https://doi.org/10.1002/9783527670819.

[114] J. Liu, Y. Ikushima, Z. Shervani, Environmentally benign preparation of metal nano-particles by using water-in-CO2 microemulsions technology, Curr. Opin. Solid State Mater. Sci. 7 (2003) 255–261. https://doi.org/10.1016/j.cossms.2003.09.005.

[115] M.C. McLeod, R.S. McHenry, E.J. Beckman, Christopher B. Roberts, Synthesis and Stabilization of Silver Metallic Nanoparticles and Premetallic Intermediates in Perfluoropolyether/CO2 Reverse Micelle Systems, (2003). https://doi.org/10.1021/JP0218645.

[116] C. Kulkarni, Kulkarni, C. V., Lipid Self-Assemblies and Nanostructured Emulsions for Cosmetic Formulations, Cosmetics. 3 (2016) 37.

https://doi.org/10.3390/cosmetics3040037.

[117] V.A. Torrealba, H. Hoteit, R.T. Johns, Description of Micellar Radii for Phase Behavior and Viscosity Modeling of Aqueous Surfactant Solutions and Microemulsions, Langmuir. 34 (2018) 15327–15334. https://doi.org/10.1021/acs.langmuir.8b02828.

[118] G.P. Kumar, P. Rajeshwarrao, Nonionic surfactant vesicular systems for effective drug delivery—an overview, Acta Pharm. Sin. B. 1 (2011) 208–219. https://doi.org/10.1016/J.APSB.2011.09.002.

[119] S. Chen, Interaction, critical, percolation and kinetic glass transitions in pluronic L-64 micellar solutions, Colloids Surfaces A Physicochem. Eng. Asp. 183–185 (2001) 95–111. https://doi.org/10.1016/S0927-7757(01)00542-8.

[120] G.E. Newby, I.W. Hamley, S.M. King, C.M. Martin, N.J. Terrill, Structure, rheology and shear alignment of Pluronic block copolymer mixtures, J. Colloid Interface Sci. 329 (2009) 54–61. https://doi.org/10.1016/j.jcis.2008.09.054.

[121] J. Jiao, Polyoxyethylated nonionic surfactants and their applications in topical ocular drug delivery, Adv. Drug Deliv. Rev. 60 (2008) 1663–1673. https://doi.org/10.1016/J.ADDR.2008.09.002.

[122] C.J. van Oss, Nonionic Surfactants: Physical Chemistry, J. Dispers. Sci. Technol. 11 (1990) 437–438. https://doi.org/10.1080/01932699008943267.

[123] M. Boutonnet, J. Kizling, P. Stenius, G. Maire, The preparation of monodisperse colloidal metal particles from microemulsions, Colloids and Surfaces. 5 (1982) 209–225. https://doi.org/10.1016/0166-6622(82)80079-6.

[124] C. Dhand, N. Dwivedi, X.J. Loh, A.N. Jie Ying, N.K. Verma, R.W. Beuerman, R. Lakshminarayanan, S. Ramakrishna, Methods and strategies for the synthesis of diverse nanoparticles and their applications: a comprehensive overview, RSC Adv. 5 (2015) 105003–105037. https://doi.org/10.1039/C5RA19388E.

[125] M. Aziz, S. Saber Abbas, W.R. Wan Baharom, Size-controlled synthesis of SnO2 nanoparticles by sol–gel method, Mater. Lett. 91 (2013) 31–34. https://doi.org/10.1016/J.MATLET.2012.09.079.

[126] S. Ghosh, Comparative studies on brij reverse micelles prepared in benzene/surfactant/ethylammonium nitrate systems: Effect of head group size and polarity of the hydrocarbon chain, J. Colloid Interface Sci. 360 (2011) 672–680. https://doi.org/10.1016/j.jcis.2011.05.006.

[127] R.D. Falcone, N.M. Correa, J.J. Silber, On the Formation of New Reverse Micelles: A Comparative Study of Benzene/Surfactants/Ionic Liquids Systems Using UV−Visible Absorption Spectroscopy and Dynamic Light Scattering, Langmuir. 25 (2009) 10426–10429. https://doi.org/10.1021/la901498e.

[128] D.M. Zhu, K.I. Feng, Z.A. Schelly, Reverse micelles of Triton X-100 in cyclohexane: effects of temperature, water content, and salinity on the aggregation behavior, J. Phys. Chem. 96 (1992) 2382–2385. https://doi.org/10.1021/j100184a068.

[129] E. Acosta, E. Szekeres, D.A. Sabatini, Jeffrey H. Harwell, Net-Average Curvature Model for Solubilization and Supersolubilization in Surfactant Microemulsions, (2002). https://doi.org/10.1021/LA026168A.

[130] *,† Jean-Louis Salager, †,‡,§ Nelson Marquez, § and Alain Graciaa, J. Lachaise§, Partitioning of Ethoxylated Octylphenol Surfactants in Microemulsion−Oil−Water Systems: Influence of Temperature and

Relation between Partitioning Coefficient and Physicochemical Formulation, (2000). https://doi.org/10.1021/LA9905517.

[131] Molybdenum - Element information, properties and uses | Periodic Table, (n.d.). http://www.rsc.org/periodic-table/element/42/molybdenum.

[132] J.D. Hem, Study and Interpretation of the Chemical Characteristics of Natural Water Third Edition, n.d. https://pubs.usgs.gov/wsp/wsp2254/pdf/wsp2254a.pdf.

[133] B. Hansen, Molybdenum Market Factors – A new paradigm emerging, n.d.

[134] E.R. (Eric R. Braithwaite, J. Haber, Molybdenum : an outline of its chemistry and uses, Elsevier, 1994.

[135] R.D. Shannon, IUCr, Revised effective ionic radii and systematic studies of interatomic distances in halides and chalcogenides, Acta Crystallogr. Sect. A. 32 (1976) 751–767. https://doi.org/10.1107/S0567739476001551.

[136] I.A. Nechaev, V.P. Zhukov, E. V. Chulkov, Ab initio calculation of the lifetime of quasiparticle excitations in transition metals within the framework of the GW approximation, Phys. Solid State. 49 (2007) 1811–1819. https://doi.org/10.1134/S1063783407100010.

[137] E. Zarate, P. Apell, P.M. Echenique, Calculation of low-energy-electron lifetimes, Phys. Rev. B. 60 (1999) 2326–2332. https://doi.org/10.1103/PhysRevB.60.2326.

[138] E.R. Braithwaite, J. Haber, Molybdenum: An Outline of its Chemistry and Uses, 2013. https://doi.org/10.1016/B978-0-444-88198-4.50012-7.

[139] D.L. Trimm, S. Akashah, A. Bishara, Catalysts in Petroleum Refining 1989 : Conference Proceedings., Elsevier, 1989.

[140] J.A. Cusumano, R.A. Dalla Betta, R. Levy, Catalysis in coal conversion, Academic Press, 1978.

[141] J.N. Fiedor, A. Proctor, M. Houalla, D.M. Hercules, Determination of the distribution of molybdenum oxidation states in reduced Mo/TiO2 catalysts by factor analysis and curve fitting, Surf. Interface Anal. 20 (1993) 1–9. https://doi.org/10.1002/sia.740200102.

[142] J. Haber, E. Lalik, Catalytic properties of MoO3 revisited, Catal. Today. 33 (1997) 119–137. https://doi.org/10.1016/S0920-5861(96)00107-1.

[143] J. Yasumaru, M. Yamada, M. Houalla, D.M. Hercules, Distribution of Mo Oxidation States in Reduced Mo/Al2O3 Catalysts. Correlation With Catalytic Activity, Stud. Surf. Sci. Catal. 75 (1993) 1867–1870. https://doi.org/10.1016/S0167-2991(08)64554-1.

[144] M. Malekshahi Byranvand, A. Nemati Kharat, L. Fatholahi, Z. Malekshahi Beiranvand, A Review on Synthesis of Nano-TiO2 via Different Methods, J. Nanostructures. 3 (2013) 1–9. https://doi.org/10.7508/JNS.2013.01.001.

[145] P. Nyamukamba, O. Okoh, H. Mungondori, R. Taziwa, S. Zinya, Synthetic Methods for Titanium Dioxide Nanoparticles: A Review, in: Titan. Dioxide - Mater. a Sustain. Environ., InTech, 2018. https://doi.org/10.5772/intechopen.75425.

[146] P. Chandra, D.S. Doke, S.B. Umbarkar, A. V. Biradar, One-pot synthesis of ultrasmall MoO3 nanoparticles supported on SiO2 , TiO2 , and ZrO2 nanospheres: an efficient epoxidation catalyst, J. Mater. Chem. A. 2 (2014) 19060–19066. https://doi.org/10.1039/C4TA03754E.

[147] T. Overview, AEROXIDE ® – Fumed Metal Oxides AEROXIDE ® – Fumed Metal Oxides, (n.d.).

[148] B. Bonelli, S. Esposito, F.S. Freyria, Mesoporous Titania: synthesis, properties and comparison with non-porous titania, in: Magdalena Janus

(Ed.), Titan. Dioxide, Intech, 2017.

[149]   R. Nasi, S. Esposito, F.S. Freyria, M. Armandi, T.A. Gadhi, S. Hernandez, P. Rivolo, N. Ditaranto, B. Bonelli, Application of Reverse Micelle Sol – Gel Synthesis for Bulk Doping and Heteroatoms Surface Enrichment in, (n.d.). https://doi.org/10.3390/ma12060937.

[150]   B.K. Mutuma, G.N. Shao, W. Duck, H. Taik, Sol – gel synthesis of mesoporous anatase – brookite and anatase – brookite – rutile TiO2 nanoparticles and their photocatalytic properties Journal of Colloid and Interface Science Sol – gel synthesis of mesoporous anatase – brookite and anatase – brookit, (2014). https://doi.org/10.1016/j.jcis.2014.11.060.

[151]   Y. Hu, H.L. Tsai, C.L. Huang, Effect of brookite phase on the anatase-rutile transition in titania nanoparticles, J. Eur. Ceram. Soc. 23 (2003) 691–696. https://doi.org/10.1016/S0955-2219(02)00194-2.

[152]   K.J.A. Raj, B. Viswanathan, Effect of surface area, pore volume and particle size of P25 titania on the phase transformation of anatase to rutile, (2009). https://www.semanticscholar.org/paper/Effect-of-surface-area%2C-pore-volume-and-particle-of-Raj-Viswanathan/70884d0fde05c3ddf7e1f65ec15492212335e141   (accessed August 24, 2019).

[153]   S. Kang, H. Qin, L. Zhang, Y. Huang, X. Bai, X. Li, D. Sun, Y. Wang, L. Cui, Efficient Photocatalytic Bilirubin Removal over the Biocompatible Core/Shell P25/g-C3N4 Heterojunctions with Metal-free Exposed Surfaces under Moderate Green Light Irradiation., Sci. Rep. 7 (2017) 44338. https://doi.org/10.1038/srep44338.

[154]   B. Xue, J. Zhang, X. Tang, C. Yang, Q. Chen, X. Man, W. Dang, Micro-pore Structure and Gas Accumulation Characteristics of Shale in the Longmaxi Formation, Northwest Guizhou, Pet. Res. 1 (2016) 191–204. https://doi.org/10.1016/S2096-2495(17)30042-X.

[155]   M. Thommes, K. Kaneko, A. V. Neimark, J.P. Olivier, F. Rodriguez-Reinoso, J. Rouquerol, K.S.W. Sing, Physisorption of gases, with special reference to the evaluation of surface area and pore size distribution (IUPAC Technical Report), Pure Appl. Chem. 87 (2015) 1051–1069. https://doi.org/10.1515/pac-2014-1117.

[156]   R. López, R. Gómez, Band-gap energy estimation from diffuse reflectance measurements on sol-gel and commercial TiO 2: A comparative study, J. Sol-Gel Sci. Technol. 61 (2012) 1–7. https://doi.org/10.1007/s10971-011-2582-9.

[157]   K. Suttiponparnit, J. Jiang, M. Sahu, S. Suvachittanont, T. Charinpanitkul, P. Biswas, Role of Surface Area, Primary Particle Size, and Crystal Phase on Titanium Dioxide Nanoparticle Dispersion Properties, Nanoscale Res. Lett. 6 (2010) 27. https://doi.org/10.1007/s11671-010-9772-1.

[158]   J. Kaeding, W. Stumm und J. J. Morgan: Aquatic Chemistry An Introduction Emphasizing Chemical Equilibria in Natural Waters. New York, London, Sydney, Toronto, Wiley-Interscience, 1970, 583 S., zahlr. Abb. und Tab, Acta Hydrochim. Hydrobiol. 1 (1973) 117–117. https://doi.org/10.1002/aheh.19730010116.

[159]   J.A. Davis, R.O. James, J.O. Leckie, Surface ionization and complexation at the oxide/water interface: I. Computation of electrical double layer properties in simple electrolytes, J. Colloid Interface Sci. 63 (1978) 480–499. https://doi.org/10.1016/S0021-9797(78)80009-5.

[160]   B. Gilbert, J.F. Banfield, Molecular-Scale Processes Involving

Nanoparticulate Minerals in Biogeochemical Systems, Rev. Mineral. Geochemistry. 59 (2005) 109–155. https://doi.org/10.2138/rmg.2005.59.6.

[161] B.R. Bickmore, K.M. Rosso, K.L. Nagy, R.T. Cygan, C.J. Tadanier, <I>Ab initio</I> determination of edge surface structures for dioctahedral 2:1 phyllosilicates: implications for acid-base for reactivity, Clays Clay Miner. 51 (2003) 359–371. https://doi.org/10.1346/CCMN.2003.0510401.

[162] J.W.B. and, M.J. Cima*, Orientation Dependence of the Isoelectric Point of TiO2 (Rutile) Surfaces, (2006). https://doi.org/10.1021/LA061900H.

[163] J.P. Holmberg, E. Ahlberg, J. Bergenholtz, M. Hassellöv, Z. Abbas, Surface charge and interfacial potential of titanium dioxide nanoparticles: Experimental and theoretical investigations, J. Colloid Interface Sci. 407 (2013) 168–176. https://doi.org/10.1016/j.jcis.2013.06.015.

[164] L. Pirinejad, A. Maleki, B. Shahmoradi, H. Daraei, J.-K. Yang, S.-M. Lee, Synthesis and application of Fe-N-Cr-TiO2 nanocatalyst for photocatalytic degradation of Acid Black 1 under LED light irradiation, J. Mol. Liq. 279 (2019) 232–240. https://doi.org/10.1016/J.MOLLIQ.2019.01.135.

[165] M.M. Allard, S.N. Merlos, B.N. Springer, J. Cooper, G. Zhang, D.S. Boskovic, S.R. Kwon, K.E. Nick, C.C. Perry, Role of TiO 2 Anatase Surface Morphology on Organophosphorus Interfacial Chemistry, J. Phys. Chem. C. 122 (2018) 29237–29248. https://doi.org/10.1021/acs.jpcc.8b08641.

[166] E. Al-Hetlani, M.O. Amin, M. Madkour, Detachable photocatalysts of anatase TiO2 nanoparticles: Annulling surface charge for immediate photocatalyst separation, Appl. Surf. Sci. 411 (2017) 355–362. https://doi.org/10.1016/J.APSUSC.2017.03.151.

[167] H. He, Y. Cheng, C. Yang, G. Zeng, C. Zhu, Z. Yan, Influences of anion concentration and valence on dispersion and aggregation of titanium dioxide nanoparticles in aqueous solutions, J. Environ. Sci. 54 (2017) 135–141. https://doi.org/10.1016/J.JES.2016.06.009.

[168] F. Azeez, E. Al-Hetlani, M. Arafa, Y. Abdelmonem, A.A. Nazeer, M.O. Amin, M. Madkour, The effect of surface charge on photocatalytic degradation of methylene blue dye using chargeable titania nanoparticles, Sci. Rep. 8 (2018) 7104. https://doi.org/10.1038/s41598-018-25673-5.

[169] D.L. Liao, G.S. Wu, B.Q. Liao, Zeta potential of shape-controlled TiO2 nanoparticles with surfactants, Colloids Surfaces A Physicochem. Eng. Asp. 348 (2009) 270–275. https://doi.org/10.1016/j.colsurfa.2009.07.036.

[170] J. Eastoe, M.J. Hollamby, L. Hudson, Recent advances in nanoparticle synthesis with reversed micelles, Adv. Colloid Interface Sci. 128–130 (2006) 5–15. https://doi.org/10.1016/j.cis.2006.11.009.

[171] C. Su, B.-Y. Hong, C.-M. Tseng, Sol–gel preparation and photocatalysis of titanium dioxide, Catal. Today. 96 (2004) 119–126. https://doi.org/10.1016/j.cattod.2004.06.132.

[172] W.D. Kingery, H.K. Bowen, D.R. (Donald R. Uhlmann, Introduction to ceramics, Wiley, 1976. https://www.wiley.com/en-us/Introduction+to+Ceramics%2C+2nd+Edition-p-9780471478607 (accessed June 15, 2018).

[173] P. Praveen, G. Viruthagiri, S. Mugundan, N. Shanmugam, Sol-gel synthesis and characterization of pure and manganese doped TiO2nanoparticles - A new NLO active material, Spectrochim. Acta - Part A Mol. Biomol. Spectrosc. 120 (2014) 548–557. https://doi.org/10.1016/j.saa.2013.12.006.

[174] E.R. Stobbe, B.A. de Boer, J.W. Geus, The reduction and oxidation

behaviour of manganese oxides, Catal. Today. 47 (1999) 161–167. https://doi.org/10.1016/S0920-5861(98)00296-X.

[175] M.C. Biesinger, B.P. Payne, A.P. Grosvenor, L.W.M. Lau, A.R. Gerson, R.S.C. Smart, Resolving surface chemical states in XPS analysis of first row transition metals, oxides and hydroxides: Cr, Mn, Fe, Co and Ni, Appl. Surf. Sci. 257 (2011) 2717–2730. https://doi.org/10.1016/J.APSUSC.2010.10.051.

[176] F. Kapteijn, A.D. Vanlangeveld, J.A. Moulijn, A. Andreini, M.A. Vuurman, A.M. Turek, J.M. Jehng, I.E. Wachs, Alumina-Supported Manganese Oxide Catalysts: I. Characterization: Effect of Precursor and Loading, J. Catal. 150 (1994) 94–104. https://doi.org/10.1006/JCAT.1994.1325.

[177] P.R. Ettireddy, N. Ettireddy, S. Mamedov, P. Boolchand, P.G. Smirniotis, Surface characterization studies of TiO2 supported manganese oxide catalysts for low temperature SCR of NO with NH3, Appl. Catal. B Environ. 76 (2007) 123–134. https://doi.org/10.1016/j.apcatb.2007.05.010.

[178] I.S. Petrik, G. V Krylova, L. V Lutsenko, N.P. Smirnova, L.P. Oleksenko, XPS AND TPR STUDY OF SOL-GEL DERIVED M / TiO 2 POWDERS (M = Co , Cu , Mn , Ni), (2015) 179–189.

[179] R. Sanjinés, H. Tang, H. Berger, F. Gozzo, G. Margaritondo, F. Lévy, Electronic structure of anatase TiO 2 oxide, J. Appl. Phys. 75 (1994) 2945–2951. https://doi.org/10.1063/1.356190.

[180] B. Bharti, S. Kumar, H.-N. Lee, R. Kumar, Formation of oxygen vacancies and Ti3+ state in TiO2 thin film and enhanced optical properties by air plasma treatment, Sci. Rep. 6 (2016) 32355. https://doi.org/10.1038/srep32355.

[181] M. Stucchi, D. Boffito, E. Pargoletti, G. Cerrato, C. Bianchi, G. Cappelletti, Nano-MnO2 Decoration of TiO2 Microparticles to Promote Gaseous Ethanol Visible Photoremoval, Nanomaterials. 8 (2018) 686. https://doi.org/10.3390/nano8090686.

[182] B. Murugan, A. V. Ramaswamy, Chemical States and Redox Properties of Mn/CeO 2 −TiO 2 Nanocomposites Prepared by Solution Combustion Route, J. Phys. Chem. C. 112 (2008) 20429–20442. https://doi.org/10.1021/jp806316x.

[183] D.A. Peña, B.S. Uphade, P.G. Smirniotis, TiO2-supported metal oxide catalysts for low-temperature selective catalytic reduction of NO with NH3: I. Evaluation and characterization of first row transition metals, J. Catal. 221 (2004) 421–431. https://doi.org/10.1016/j.jcat.2003.09.003.

[184] K. Zhuang, J. Qiu, F. Tang, B. Xu, Y. Fan, The structure and catalytic activity of anatase and rutile titania supported manganese oxide catalysts for selective catalytic reduction of NO by NH3, Phys. Chem. Chem. Phys. 13 (2011) 4463. https://doi.org/10.1039/c0cp02288h.

[185] Y. Song, R.J. Hemley, Z. Liu, M. Somayazulu, H.K. Mao, D.R. Herschbach, High-pressure stability, transformations, and vibrational dynamics of nitrosonium nitrate from synchrotron infrared and Raman spectroscopy, J. Chem. Phys. 119 (2003) 2232–2240. https://doi.org/10.1063/1.1586695.

[186] A. Sultana, M. Sasaki, H. Hamada, Influence of support on the activity of Mn supported catalysts for SCR of NO with ammonia, Catal. Today. 185 (2012) 284–289. https://doi.org/10.1016/J.CATTOD.2011.09.018.

[187] Shuhui Liang, Fei Teng, G. Bulgan, and Ruilong Zong, Y. Zhu*, Effect of Phase Structure of MnO2 Nanorod Catalyst on the Activity for CO Oxidation, (2008). https://doi.org/10.1021/JP0774995.

[188] X. Tang, J. Li, L. Sun, J. Hao, Origination of N2O from NO reduction by NH3 over β-MnO2 and α-Mn2O3, Appl. Catal. B Environ. 99 (2010) 156–162. https://doi.org/10.1016/J.APCATB.2010.06.012.

[189] S.S.R. Putluru, L. Schill, A.D. Jensen, B. Siret, F. Tabaries, R. Fehrmann, Mn/TiO2 and Mn-Fe/TiO2 catalysts synthesized by deposition precipitation-promising for selective catalytic reduction of NO with NH3 at low temperatures, Appl. Catal. B Environ. 165 (2015) 628–635. https://doi.org/10.1016/j.apcatb.2014.10.060.

[190] G.P. Deshmukh, G.D. Yadav, Insight into regioselective hydrogenation of methyl phenyl glyoxalate to methyl mandelate over Pt/α-MnO2 nanorods, Mol. Catal. 433 (2017) 250–264. https://doi.org/10.1016/J.MCAT.2017.02.002.

[191] S.T. Oyama, G.T. Went, K.B. Lewis, A.T. Bell, G.A. Somorjai, Oxygen chemisorption and laser Raman spectroscopy of unsupported and silica-supported vanadium oxide catalysts, J. Phys. Chem. 93 (1989) 6786–6790. https://doi.org/10.1021/j100355a041.

[192] A. Jha, T. Chandole, R. Pandya, H.-S. Roh, C. V. Rode, Solvothermal synthesis of mesoporous manganese oxide with enhanced catalytic activity for veratryl alcohol oxidation, RSC Adv. 4 (2014) 19450–19455. https://doi.org/10.1039/C4RA00184B.

[193] S. Bhatia, J. Beltramini, D.D. Do, Temperature programmed analysis and its applications in catalytic systems, Catal. Today. 7 (1990) 309–438. https://doi.org/10.1016/0920-5861(90)87001-J.

[194] F. Kapteijn, L. Singoredjo, A. Andreini, J.A. Moulijn, Activity and selectivity of pure manganese oxides in the selective catalytic reduction of nitric oxide with ammonia, Appl. Catal. B Environ. 3 (1994) 173–189. https://doi.org/10.1016/0926-3373(93)E0034-9.

[195] V.G. Deshmane, S.L. Owen, R.Y. Abrokwah, D. Kuila, Mesoporous nanocrystalline TiO2 supported metal (Cu, Co, Ni, Pd, Zn, and Sn) catalysts: Effect of metal-support interactions on steam reforming of methanol, J. Mol. Catal. A Chem. 408 (2015) 202–213. https://doi.org/10.1016/J.MOLCATA.2015.07.023.

[196] Y. Khan, S.K. Durrani, M. Mehmood, M.R. Khan, Mild hydrothermal synthesis of γ-MnO2 nanostructures and their phase transformation to α-MnO2 nanowires, J. Mater. Res. 26 (2011) 2268–2275. https://doi.org/10.1557/jmr.2011.138.

[197] B. Nammalwar, C. Fortenberry, R.A. Bunce, S.K. Lageshetty, K.D. Ausman, Efficient oxidation of arylmethylene compounds using nano-MnO2, Tetrahedron Lett. 54 (2013) 2010–2013. https://doi.org/10.1016/J.TETLET.2013.02.009.

[198] J.R. Dahn, E.W. Fuller, M. Obrovac, U. von Sacken, Thermal stability of LixCoO2, LixNiO2 and λ-MnO2 and consequences for the safety of Li-ion cells, Solid State Ionics. 69 (1994) 265–270. https://doi.org/10.1016/0167-2738(94)90415-4.

[199] Y. Zhao, C. Li, X. Liu, F. Gu, H.L. Du, L. Shi, Zn-doped TiO2 nanoparticles with high photocatalytic activity synthesized by hydrogen–oxygen diffusion flame, Appl. Catal. B Environ. 79 (2008) 208–215. https://doi.org/10.1016/J.APCATB.2007.09.044.

[200] C. Ciardelli, I. Nova, E. Tronconi, D. Chatterjee, B. Bandl-Konrad, M. Weibel, B. Krutzsch, Reactivity of NO/NO2–NH3 SCR system for diesel exhaust aftertreatment: Identification of the reaction network as a function

of temperature and NO2 feed content, Appl. Catal. B Environ. 70 (2007) 80–90. https://doi.org/10.1016/J.APCATB.2005.10.041.

[201] S. Suárez, J.A. Martín, M. Yates, P. Avila, J. Blanco, N2O formation in the selective catalytic reduction of NOx with NH3 at low temperature on CuO-supported monolithic catalysts, J. Catal. 229 (2005) 227–236. https://doi.org/10.1016/J.JCAT.2004.10.019.

[202] Giuseppe Madia, * Manfred Koebel, and Martin Elsener, A. Wokaun, Side Reactions in the Selective Catalytic Reduction of NOx with Various NO2 Fractions, (2002). https://doi.org/10.1021/IE020054C.

[203] N.I. Il'chenko, G.I. Golodets, Catalytic oxidation of ammonia: II. Relationship between catalytic properties of substances and surface oxygen bond energy. General regularities in catalytic oxidation of ammonia and organic substances, J. Catal. 39 (1975) 73–86. https://doi.org/10.1016/0021-9517(75)90283-3.

[204] A. Malik, S. Hameed, M.J. Siddiqui, M.M. Haque, K. Umar, A. Khan, M. Muneer, Electrical and Optical Properties of Nickel- and Molybdenum-Doped Titanium Dioxide Nanoparticle: Improved Performance in Dye-Sensitized Solar Cells, J. Mater. Eng. Perform. 23 (2014) 3184–3192. https://doi.org/10.1007/s11665-014-0954-3.

[205] P. Ciambelli, D. Sannino, V. Palma, V. Vaiano, R.I. Bickley, Reaction mechanism of cyclohexane selective photo-oxidation to benzene on molybdena/titania catalysts, Appl. Catal. A Gen. 349 (2008) 140–147. https://doi.org/10.1016/j.apcata.2008.07.019.

[206] M. Del Arco, S.R.G. Carrazhn, V. Rives, J. V. Garcla-Ramos, A Laser Raman Spectroscopy Study of Surface Species Existing in MoO_3/Al_2O_3 Catalysts, Spectrosc. Lett. 25 (1992) 73–82. https://doi.org/10.1080/00387019208020758.

[207] S.R. Stampfl, Y. Chen, J.A. Dumesic, C. Niu, C.G. Hill, Interactions of molybdenum oxide with various oxide supports: Calcination of mechanical mixtures, J. Catal. 105 (1987) 445–454. https://doi.org/10.1016/0021-9517(87)90072-8.

[208] J.P. Holmberg, E. Ahlberg, J. Bergenholtz, M. Hassellöv, Z. Abbas, Surface charge and interfacial potential of titanium dioxide nanoparticles: Experimental and theoretical investigations, J. Colloid Interface Sci. 407 (2013) 168–176. https://doi.org/10.1016/J.JCIS.2013.06.015.

[209] J.C. Lavalley, Infrared spectrometric studies of the surface basicity of metal oxides and zeolites using adsorbed probe molecules, Catal. Today. 27 (1996) 377–401. https://doi.org/10.1016/0920-5861(95)00161-1.

[210] K.I. Hadjiivanov, G.N. Vayssilov, Characterization of oxide surfaces and zeolites by carbon monoxide as an IR probe molecule, Adv. Catal. 47 (2002) 307–511. https://doi.org/10.1016/S0360-0564(02)47008-3.

[211] V. Bolis, B. Fubini, E. Garrone, C. Morterra, Thermodynamic and vibrational characterization of CO adsorption on variously pretreated anatase, J. Chem. Soc. Faraday Trans. 1 Phys. Chem. Condens. Phases. 85 (1989) 1383. https://doi.org/10.1039/f19898501383.

[212] C. Deiana, E. Fois, G. Martra, S. Narbey, F. Pellegrino, G. Tabacchi, On the Simple Complexity of Carbon Monoxide on Oxide Surfaces: Facet-Specific Donation and Backdonation Effects Revealed on TiO_2 Anatase Nanoparticles, ChemPhysChem. 17 (2016) 1956–1960. https://doi.org/10.1002/cphc.201600284.

[213] H. Park, Y. Park, W. Kim, W. Choi, Surface modification of TiO2

photocatalyst for environmental applications, J. Photochem. Photobiol. C Photochem. Rev. 15 (2013) 1–20. https://doi.org/10.1016/j.jphotochemrev.2012.10.001.

[214] J. Diaz-Angulo, I. Gomez-Bonilla, C. Jimenez-Tohapanta, M. Mueses, M. Pinzon, F. Machuca-Martinez, Visible-light activation of TiO 2 by dye-sensitization for degradation of pharmaceutical compounds, Photochem. Photobiol. Sci. 18 (2019) 897–904. https://doi.org/10.1039/c8pp00270c.

[215] C. Lops, A. Ancona, K. Di, B. Dumontel, N. Garino, Applied Catalysis B : Environmental Sonophotocatalytic degradation mechanisms of Rhodamine B dye via radicals generation by micro- and nano-particles of ZnO, Appl. Catal. B Environ. 243 (2019) 629–640. https://doi.org/10.1016/j.apcatb.2018.10.078.

[216] M. Rochkind, S. Pasternak, Y. Paz, M. Rochkind, S. Pasternak, Y. Paz, Using Dyes for Evaluating Photocatalytic Properties: A Critical Review, Molecules. 20 (2014) 88–110. https://doi.org/10.3390/molecules20010088.

[217] T.A. Gadhi, A. Hernández-Gordillo, M. Bizarro, P. Jagdale, A. Tagliaferro, S.E. Rodil, Efficient α/β-Bi2O3composite for the sequential photodegradation of two-dyes mixture, Ceram. Int. 42 (2016) 13065–13073. https://doi.org/10.1016/j.ceramint.2016.05.087.

[218] T.A. Gadhi, S. Hernández, M. Castellino, A. Chiodoni, T. Husak, G. Barrera, P. Allia, N. Russo, A. Tagliaferro, Single BiFeO3 and mixed BiFeO3/Fe2O3/Bi2Fe4O9 ferromagnetic photocatalysts for solar light driven water oxidation and dye pollutants degradation, J. Ind. Eng. Chem. 63 (2018) 437–448. https://doi.org/10.1016/J.JIEC.2018.03.004.

[219] R. Boppella, P. Basak, S. V. Manorama, Viable method for the synthesis of biphasic TiO 2 nanocrystals with tunable phase composition and enabled visible-light photocatalytic performance, ACS Appl. Mater. Interfaces. 4 (2012) 1239–1246. https://doi.org/10.1021/am201354r.